

AD-A135 880

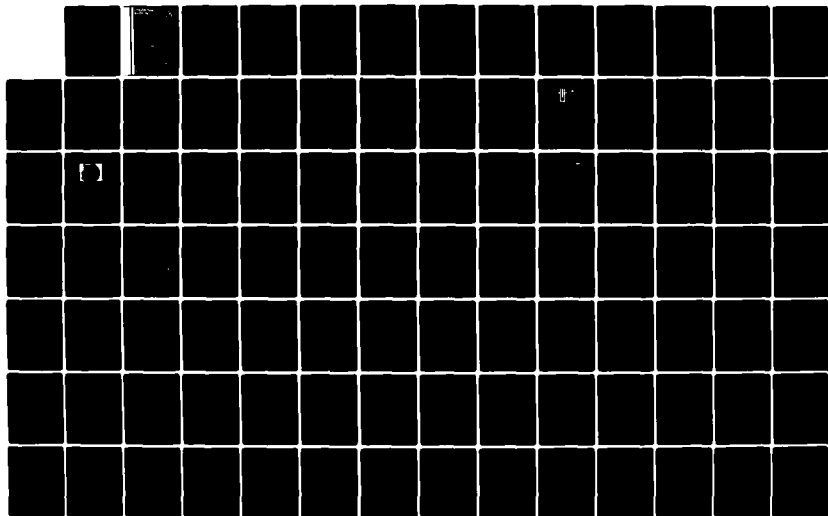
AN INVESTIGATION OF RF CURRENTS IN A MAGNETIZED PLASMA
USING A SLOW WAVE..(U) POLYTECHNIC INST OF NEW YORK
FARMINGDALE DEPT OF ELECTRICAL E.. B R POOLE ET AL.
OCT 83 POLY-EE-83-004 AFOSR-TR-83-1057

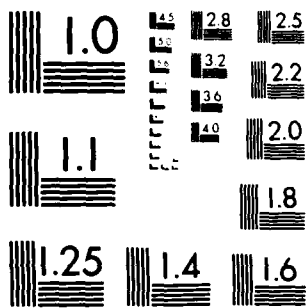
1/2

UNCLASSIFIED

F/G 20/3

NL





MICROCOPY RESOLUTION TEST CHART
NATIONAL BUREAU OF STANDARDS 1963-A

Polytechnic Institute of New York

AFOSR-TR. 83-1057



ELECTRICAL ENGINEERING DEPARTMENT

POLY-EE-83-004
October 1983

AD-A135880

AN INVESTIGATION OF RF CURRENTS IN A MAGNETIZED PLASMA USING A SLOW WAVE STRUCTURE

by

B.R. Poole and B.R. Cheo

Interim ~~SCIENTIFIC REPORT~~

Prepared For

AIR FORCE OFFICE OF SCIENTIFIC RESEARCH

Grant No. AFOSR-79-0009

~~AFOSR-79-0009~~

DTIC
ELECTE
DEC 15 1983
S D

Approved for public release;
distribution unlimited.

DTIC FILE COPY

83 12 13 273

Unclassified

SECURITY CLASSIFICATION OF THIS PAGE (When Data Entered)

REPORT DOCUMENTATION PAGE		READ INSTRUCTIONS BEFORE COMPLETING FORM
1. REPORT NUMBER AFOSR-TR- 83-1057	2. GOVT ACCESSION NO. AD-A135880	3. RECIPIENT'S CATALOG NUMBER
4. TITLE (and Subtitle) An Investigation of RF Driven Currents in a Magnetized Plasma Using a Slow Wave Structure		5. TYPE OF REPORT & PERIOD COVERED FINAL Scientific Report Oct. 1, 1978-December 31, 1982
7. AUTHOR(s) Brian R. Poole Bernard R. Cheo		6. PERFORMING ORG. REPORT NUMBER
9. PERFORMING ORGANIZATION NAME AND ADDRESS Polytechnic Institute of New York Electrical Engineering Department Rt. 110, Farmingdale, N.Y. 11735		8. CONTRACT OR GRANT NUMBER(s) AFOSR-79-0009
11. CONTROLLING OFFICE NAME AND ADDRESS Air Force Office of Scientific Research /NP Washington, D.C.		10. PROGRAM ELEMENT, PROJECT, TASK AREA & WORK UNIT NUMBERS 61102F 2301/A8
14. MONITORING AGENCY NAME & ADDRESS (if different from Controlling Office)		12. REPORT DATE October 1983
		13. NUMBER OF PAGES 123
		15. SECURITY CLASS. (of this report) Unclassified
		15a. DECLASSIFICATION/DOWNGRADING SCHEDULE
16. DISTRIBUTION STATEMENT (of this Report) Approved for public release, distribution unlimited.		
17. DISTRIBUTION STATEMENT (of the abstract entered in Block 20, if different from Report)		
18. SUPPLEMENTARY NOTES		
19. KEY WORDS (Continue on reverse side if necessary and identify by block number) RF Driven Currents, Slow Wave Structure, Electrostatic Waves, Ponderomotive Force		
20. ABSTRACT (Continue on reverse side if necessary and identify by block number) An investigation of the interaction of electrostatic waves launched by a slow wave structure with a magnetized plasma is made. The characteristics of the electrostatic waves and the electron dynamics are studied experimentally. Of primary experimental interest is the measurement of the electron energy distribution and the rf-induced electron flux along the background magnetic field. This interest is motivated by a need for a more complete understanding of interaction of plasma with a slow wave electrostatic field which is of importance for rf-heating and rf current drive in fusion plasmas. (continued)		

DD FORM 1 JAN 73 1473

Unclassified

SECURITY CLASSIFICATION OF THIS PAGE (When Data Entered)

Unclassified

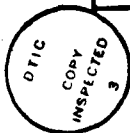
SECURITY CLASSIFICATION OF THIS PAGE(When Data Entered)

20. Abstract (Continued)

Electrostatic waves are launched from a slow wave structure near the low density periphery of a magnetized plasma column that possesses density gradients in both the radial and axial directions. The axial inhomogeneity is found to significantly complicate the picture of wave propagation. It is found the waves launched along the background magnetic field into a region of increasing electron density can experience a reflection as the wave propagates into the plasma interior. Significant increases in the effective electron temperature and rf-induced axial electron flux near the plasma surface are observed using an electrostatic energy analyzer and current probes. The lower-hybrid resonance layer as determined by the observations of large radial phase changes using rf probes in this region correspond approximately with the radial location of increased electron temperature and rf-induced electron flux.

The increase in effective electron temperature can be attributed to the coherent oscillations of the resonant electrons in the wave field as derived from the quasilinear theory. The rf-induced electron flux can be interpreted as the nonlinear ponderomotive force on electrons due to the parallel gradient of the electric field energy. The experimental results are in qualitative agreement with theory.

Accession For	
NTIS GRA&I	<input checked="checked" type="checkbox"/>
DTIC TAB	<input type="checkbox"/>
Unannounced	<input type="checkbox"/>
Justification	<input type="checkbox"/>
By _____	
Distribution/	
Availability Codes	
Dist.	Avail and/or Special
A/1	



Unclassified

SECURITY CLASSIFICATION OF THIS PAGE(When Data Entered)

AN ABSTRACT

MATTHEW J. KERPER
Chief, Technical Information Division

An investigation of the interaction of electrostatic waves launched by a slow wave structure with a magnetized plasma is made. The characteristics of the electrostatic waves and the electron dynamics are studied experimentally.

Of primary experimental interest is the measurement of the electron energy distribution and the rf-induced electron flux along the background magnetic field. This interest is motivated by a need for a more complete understanding of interaction of plasma with a slow wave electrostatic field which is of importance for rf-heating and rf dc current drive in plasmas.

Electrostatic waves are launched from a slow wave structure near the low density periphery of a magnetized plasma column that possesses density gradients in both the radial and axial directions. The axial inhomogeneity is found to significantly complicate the picture of wave propagation.

It is found the waves launched along the background magnetic field into a region of increasing electron density can experience a reflection as the wave propagates into the plasma interior. Significant increases in the effective electron temperature and rf-induced axial electron flux near the plasma surface are observed using an electrostatic energy analyzer and current probes. The lower-hybrid resonance layer as determined by the observations of large radial phase changes using rf probes in this region correspond approximately with the radial location of increased electron temperature and rf-induced electron flux.

The increase in effective electron temperature can be attributed to the coherent oscillations of the resonant electrons in the wave field as derived from the quasilinear theory. The rf-induced electron flux can be interpreted as the nonlinear ponderomotive force on electrons due to the parallel gradient of the electric field energy. The experimental results are in qualitative agreement with theory.

TABLE OF CONTENTS

<u>Chapter</u>	<u>Page</u>
1 INTRODUCTION.....	1
2 EXPERIMENTAL SETUP.....	3
1. General Description.....	3
2. Vacuum System.....	3
3. Magnet System.....	5
4. Microwave Power System.....	6
5. Microwave Energy Coupler.....	11
6. RF System and Slow Wave Structure.....	14
3 PLASMA DIAGNOSTIC SYSTEMS.....	21
1. General Description.....	21
2. Electrostatic Probes.....	21
3. DC Current Probes.....	26
4. RF Probes.....	29
5. Retarding Field Electrostatic Energy Analyzer.....	32
4 EXPERIMENTAL RESULTS.....	43
1. Introduction.....	43
2. Background Plasma.....	43
3. Typical Plasma Parameters.....	57
4. Free Space Characteristics of the Slow Wave Structure.....	61
5. Experimental Results on the Interaction of the Plasma with Unidirectional RF Waves Excited by the Slow Wave Structure.....	65
5 THEORETICAL FORMULATION AND INTERPRETATION OF EXPERIMENTAL RESULTS.....	99
1. Introduction.....	99
2. Electrostatic Waves in a Magnetized Plasma.....	99
3. Interaction of Electrostatic Waves with Plasma.....	107
4. Conclusions and Proposal for Future Work.....	114
REFERENCES.....	116

LIST OF FIGURES

<u>Figure</u>		<u>Page</u>
2-1	Basic Experimental Setup.....	4
2-2	Vacuum Chamber, Field Coil Location, Diagnostic Port Locations and RF Slow Wave Structure Coupling Ports.....	7
2-3	Axial Magnetic Field per Unit Current Profiles for Coupler Coils and Drift Coils.....	8
2-4	Total Magnetic Axial Field Profile for $I_c = 96A$, $I_d = 150A$	8
2-5	ECRH Microwave System.....	9
2-6	Magnetron Output Characteristic	10
2-7	Lisitano Coil.....	12
2-8	Physical Dimensions of Lisitano Coil.....	12
2-9	Overall Assembly of Microwave Energy Coupler.....	13
2-10	Electric Field Configuration of Microwave Energy Coupler.....	15
2-11	Schematic of Low Frequency RF System and Slow Wave Structure.....	16
2-12	Pictorial Representation of Slow Wave Structure.....	17
2-13	RF Spectrum of Transmitter Output.....	19
2-14	Dimensions of Coupling Plates of Slow Wave Structure.....	20
3-1	Basic Diagnostic Setup.....	22
3-2	Locus of Radial and Azimuthal Probe Paths.....	23
3-3	Circuitry for Probe Positioning Assembly.....	24
3-4	Construction of Langmuir Probe.....	24
3-5	Electronic Circuit for Langmuir Probe Measurements.....	25
3-6	Typical Langmuir Probe Characteristic.....	25
3-7	Construction of DC Current Probe.....	27
3-8	Electronic Circuit for DC Current Profile Measurements.....	27
3-9	Construction of RF Probe.....	31
3-10	Electronic Circuit for Amplitude and Phase Measurements of RF Potential.....	31
3-11	Grid Configuration of Retarding Field Electrostatic Energy Analyzer.....	34
3-12	Construction of Electrostatic Energy Analyzer.....	34

<u>Figure</u>		<u>Page</u>
3-13	Electronic System for Measuring Electron Distribution Function.....	38
3-14	Typical Experimental Electron Energy Distribution.....	40
4-1	Reflected and Transmitted Microwave Power vs. Incident Power for Lisitano Coil.....	45
4-2	Axial Reference Position for Experimental Measurements.....	46
4-3	Radial Profile of Electron Density at $z = -3.81$ cm.....	47
4-4	Electron Density vs. r^2 at $z = -3.81$ cm.....	48
4-5	Electron Temperature vs. r^2 at $z = -3.81$ cm.....	49
4-6	Radial Profile of Relative Magnitude of Ion Saturation Current.....	50
4-7	Magnitude of Ion Saturation Current vs. α with z as a Parameter.....	51
4-8	Axial Profile of Electron Density at $r = 0$	53
4-9	Axial Profile of Electron Temperature at $r = 0$	54
4-10	Magnitude of Ion Saturation Current vs. α with ECRH Power as a Parameter.....	55
4-11	Background Axial Electron Current Density vs. α	56
4-12	Background Electron Energy Distribution at $(r, \theta) = (3.81 \text{ cm}, \pi/2)$	59
4-13	Background Electron Energy Distribution from Fig. 4-12.....	59
4-14	Axial Phase Shift of Slow Wave Structure in Free Space.....	62
4-15	Relative Magnitude of RF Potential vs. α with z as a Parameter in Free Space.....	63
4-16	α -Profile of Phase in Free Space.....	64
4-17	Electron Density vs. r^2 with k_{z0} and P_{rf} as a Parameter at $z = -3.81$ cm.....	66
4-18	Magnitude of Ion Saturation Current vs. α for $P_{rf} = 6.25$ Watts.....	67
4-19	Magnitude of Ion Saturation Current vs. α for $P_{rf} = 25$ Watts.....	68
4-20	α -Profiles of Axial Electron Current Density for $k_{z0} = .21 \text{ cm}^{-1}$	70

<u>Figure</u>		<u>Page</u>
4-21	α -Profiles of Axial Electron Current Density for $k_{zo} = -.21 \text{ cm}^{-1}$	71
4-22	Azimuthal Profile of Electron Current Density at $r = 3.81 \text{ cm}$	72
4-23	Max. Value of Electron Current Density for Peak A vs. RF Power	73
4-24	Max. Value of Electron Current Density for Peak B vs. RF Power	74
4-25	Radial Location of Peak A of Electron Flux as a Function of RF Power	75
4-26	Axial Electron Current Density vs. α for $k_{zo} = .21 \text{ cm}^{-1}$ with ECRH Power as a Parameter	76
4-27	Axial Electron Current Density vs. α for $k_{zo} = -.21 \text{ cm}^{-1}$ with ECRH Power as a Parameter	77
4-28	Electron Energy Distribution for $k_{zo} = .21 \text{ cm}^{-1}$ with P_{rf} as a Parameter	79
4-29	Electron Energy Distribution for $k_{zo} = -.21 \text{ cm}^{-1}$ with P_{rf} as a Parameter	80
4-30	Peak of Electron Energy Distribution vs. P_{rf}	81
4-31	Velocity Corresponding to Peak of Energy Distribution vs. P_{rf}	82
4-32	Effective Electron Temperature vs. Peak RF Voltage	83
4-33	Relative Value of Axial Electron Flux vs. RF Power	84
4-34	Average Electron Velocity vs. P_{rf}	85
4-35	Average Electron Kinetic Energy vs. RF Power	86
4-36	Electron Energy Distribution for $P_{rf} = 225 \text{ Watts}$	88
4-37	α -Profile of Relative RF Amplitude	89
4-38	Max. RF Probe Signal vs. Peak RF Voltage	90
4-39	α -Profiles of Phase for $k_{zo} = .21 \text{ cm}^{-1}$ and $P_{rf} = 6.25 \text{ Watts}$ with z as a Parameter	91

Figure

4-40	α -Profiles of Phase for $k_{zo} = -.21\text{cm}^{-1}$ and $P_{rf} = 6.25$ Watts with z as a Parameter.....	92
4-41	α -Profiles of Phase for $k_{zo} = .21\text{cm}^{-1}$ and $P_{rf} = 25$ Watts with z as a Parameter.....	93
4-42	α -Profiles of Phase for $k_{zo} = -.21\text{cm}^{-1}$ and $P_{rf} = 25$ Watts with z as a Parameter.....	94
4-43	α -Profiles of Phase for $k_{zo} = .21\text{cm}^{-1}$ and $P_{rf} = 196$ Watts with z as a Parameter.....	95
4-44	α -Profiles of Phase for $k_{zo} = -.21\text{cm}^{-1}$ and $P_{rf} = 196$ Watts with z as a Parameter.....	96
4-45	α -Profiles of Phase for $k_{zo} = .21\text{cm}^{-1}$ and $P_{rf} = 6.25$ Watts with ECRH Power as a Parameter.....	97
4-46	α -Profiles of Phase for $k_{zo} = -.21\text{cm}^{-1}$ and $P_{rf} = 6.25$ Watts with ECRH Power as a Parameter.....	98
5-1	Geometry of the Model.....	101

Chapter 1

INTRODUCTION

The interaction of rf waves with plasmas has been extensively studied especially in recent times because of their applicability to rf current drive and plasma heating. Techniques involving the coupling of energy to lower hybrid waves have received considerable attention in realizing these goals. In thermonuclear devices the lower hybrid frequency is in the low gigahertz range where the high power required for heating and current drive is readily available using conventional high power microwave sources.

Wong¹ has observed current generation by unidirectional electron plasma waves and McWilliams, et.al.^{2,3} have studied rf driven current by collisionless and collisional damping of lower hybrid waves. In addition, current drive using lower hybrid waves has been observed by Bernabei, et.al.⁴ in the PLT tokamak. General studies of rf current drive have been made by Bhadra, et.al.⁵ and Fisch and Karney⁶. Extensive studies have been made in the literature of the excitation and properties of lower hybrid waves in plasmas⁷⁻¹³.

In this report we consider an experimental study of the interaction of plasma with electrostatic waves launched by an external slow wave structure. Electrostatic waves are launched along the background magnetic field with either an $e^{ik_z z}$ or $e^{-ik_z z}$ dependence at the low density periphery of the plasma column. The plasma possesses density gradients in both the radial and axial direction which complicates the description of wave propagation in the plasma. Experimental investigations of both particle and wave dynamics under the influence of these externally launched slow electrostatic waves are examined.

A detailed description of the experimental setup is given in chapter 2. The plasma production scheme and the system used to excite slow electrostatic waves is discussed as well as the supporting equipment required for the experiment. Chapter 3 describes a variety of diagnostics used in the experiments for measurements of the properties of the plasma as well as for the rf waves. Where applicable, the basic theories of the diagnostic systems are discussed so that a reliable interpretation of

experimental data can be made. Detailed experimental results are presented in chapter 4. First, a description of the background plasma is made and secondly the results are presented from the measurements when the plasma was excited by the slow electrostatic wave. Measurements include; radial and axial profiles of electron density and temperature, radial and azimuthal profiles of axial electron current, density, axial electron energy distribution function as determined from an electrostatic energy analyzer, and amplitude and phase measurements of the rf potential in the plasma. In chapter 5 a brief discussion of the wave structure in a plasma with both axial and transverse inhomogeneities is made using the cold, magnetized plasma dielectric tensor. Also a discussion is made of the interaction of the electrostatic waves with the plasma electrons. An interpretation of experimental results is also discussed in this chapter with suggestions for future work.

Chapter 2

EXPERIMENTAL SETUP

To understand the dynamics of a plasma, it is important to be familiar with the method used to produce the plasma as well as the diagnostic techniques used to obtain experimental data. In this chapter, the method and associated systems used for plasma production will be discussed. Also, the system used to excite low phase velocity ($\omega/k_z \ll c$) electrostatic waves for the rf experiments will be discussed. Chapter 3 will be devoted to the various plasma diagnostic and electronic systems used in the experiments.

2.1 General Description

The plasma is produced and maintained by electron cyclotron resonance heating (ECRH) at 2.45 GHz in a magnetic mirror field at one end of a linear device. The plasma drifts out of this coupler region into a drift region with a uniform axial magnetic field. Measurements are made in the relatively quiescent drift region. A general pictorial representation of the device is shown in Fig. 2-1. Fig. 2-1 does not show the slow wave rf coupling structure. The slow wave structure and the associated rf system will be discussed in section 2.6.

The discharge is typically operated at a pressure of 2×10^{-4} Torr with Argon as the filling gas. The plasma is weakly ionized (typically 0.5%) with electron densities on the order of 10^{10} cm^{-3} at the center of the plasma column. The electron temperature is generally about 4 eV.

2.2 Vacuum System

The vacuum system is composed of a 6-inch high speed diffusion pump backed by a rotary mechanical pump. A Varian model 336, 6-inch water cooled baffle is mounted between the diffusion pump and the sliding valve to prevent backstreaming of pump contaminants into the vacuum chamber. The diffusion pump is a National Research Corporation model VHS6 with an operating range of 10^{-3} Torr to 10^{-9} Torr and a pumping speed greater than 2000 liters/sec. The mechanical backing pump is a Duo Seal model 1397 rotary pump.

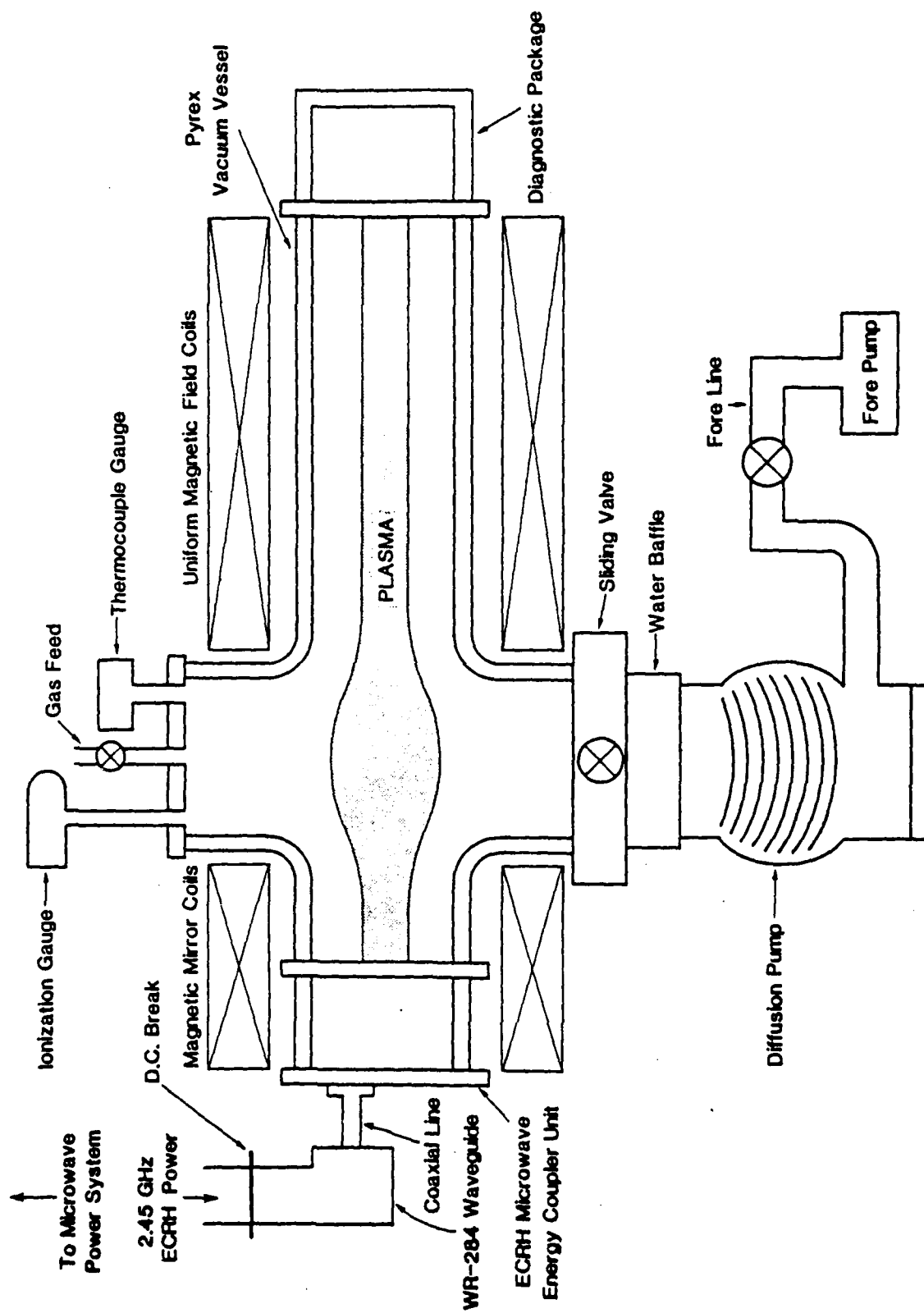


Fig. 2-1 Basic Experimental Setup

The mechanical forepump maintains a system pressure of approximately 10^{-3} Torr. To prepare the machine for plasma production, the diffusion pump is activated and evacuates the system to 10^{-6} Torr base pressure. Argon gas is then leaked into the chamber using a flow gauge to obtain an equilibrium flow at 2×10^{-4} Torr operating pressure.

Pressures below 10^{-3} Torr are measured by a Varian model 563 Bayard-Alpert ionization gauge, controlled by a Varian model 843 ratio-matic ionization gauge control. The Varian 843 unit also contains two thermocouple gauge monitors. Pressures above 10^{-3} Torr are measured by a Varian model 531 thermocouple gauge tube.

The vacuum chamber which basically consists of three main sections, is 15.24 cm in diameter and has a total length of approximately 1.2 meters. The first section houses the microwave energy coupler and is constructed of aluminum to provide adequate shielding of the microwave coupler as well as acting as the reference electrode for the plasma experiments. Its large structure which is externally water cooled also dissipates the large quantities of heat generated in the microwave energy coupler. It is approximately 11.9 cm in length. The second section of the vacuum chamber is a pyrex 4-port tee section (see Fig. 2-1). This section is 45.7 cm long. The third section is a 61 cm long straight pyrex section. This last section has fourteen 1.27 cm diameter ports at various locations for plasma diagnostics and the power feeds for the slow wave structure. Fig. 2.2 shows the locations of these ports.

2.3 Magnet System

The axial magnetic field is provided by two sets of Princeton L-2 water cooled coils. One set of ten coils establishes the magnetic mirror field used in the ECRH coupler region. These ten coils are series connected to a Sorensen model DCR40-125 dc power supply capable of delivering up to 150A at a maximum power of 7.5 kW. The power supply is operated at 96A establishing the ECRH condition for plasma production. The second set of coils establishes the uniform axial magnetic field in the drift region. These ten coils are series connected to a HuMac dc power supply capable of delivering up to 600A at a maximum power of 180

kW. The maximum allowable current through the L-2 coil is 300A. A uniform magnetic field of approximately 1.8 kG results if the drift coils are operated at the 300A limit.

Fig. 2-2 shows the location of the L-2 coils in reference to the vacuum chamber. Fig. 2-3 shows the axial magnetic mirror field profile per unit mirror field current as function of axial position. Also shown in Fig. 2-3 is the axial drift magnetic field profile per unit drift field current as a function of axial position. Fig. 2-4 shows the total axial magnetic field profile for a mirror field current of 96A and a drift field current of 150A. Most of the experiments were performed using these magnetic field parameters.

The plasma column acquired maximum radius at the region of minimum magnetic field, i.e., near the region of the high vacuum port. The magnetic field is uniform over the circular cross section of the plasma column.

2.4 Microwave Power System

The microwave system used for ECRH is shown in Fig. 2-5. The microwave power is produced by an Amperex model YJ1160 magnetron capable of delivering up to 2.5 kW cw at $2.45 \text{ GHz} \pm 25 \text{ MHz}$. The anode of the magnetron is water cooled and the cathode radiator is air cooled. The output power of the magnetron is proportional to the beam current as shown in Fig. 2-6. The magnetron operates at a cathode voltage of approximately -4.6 kV. To maintain a stable microwave power output, a high voltage beam current regulator is used in conjunction with the high voltage dc power supply to deliver a well regulated beam current to the magnetron.

The output coupling of the magnetron is a 1 5/8" rigid coaxial line with an impedance of 50Ω . The magnetron output is connected to a tapered coaxial line which reduces the 1 5/8" coaxial line to a 7/8" coaxial line while maintaining a line impedance of 50Ω . The 7/8" coaxial line is coupled to a WR-284 S-band waveguide through a coax-waveguide adapter. The microwave energy is then fed through an isolator used to protect the magnetron against excessive reflected power. The isolator can dissipate reflected microwave power up to 750 W average power. The output of the isolator is connected to a dual directional

Slow Wave Structure Coupling Ports
(see section 2.6)

6 Ports Directly Opposite On
Other Side Of Vacuum Chamber

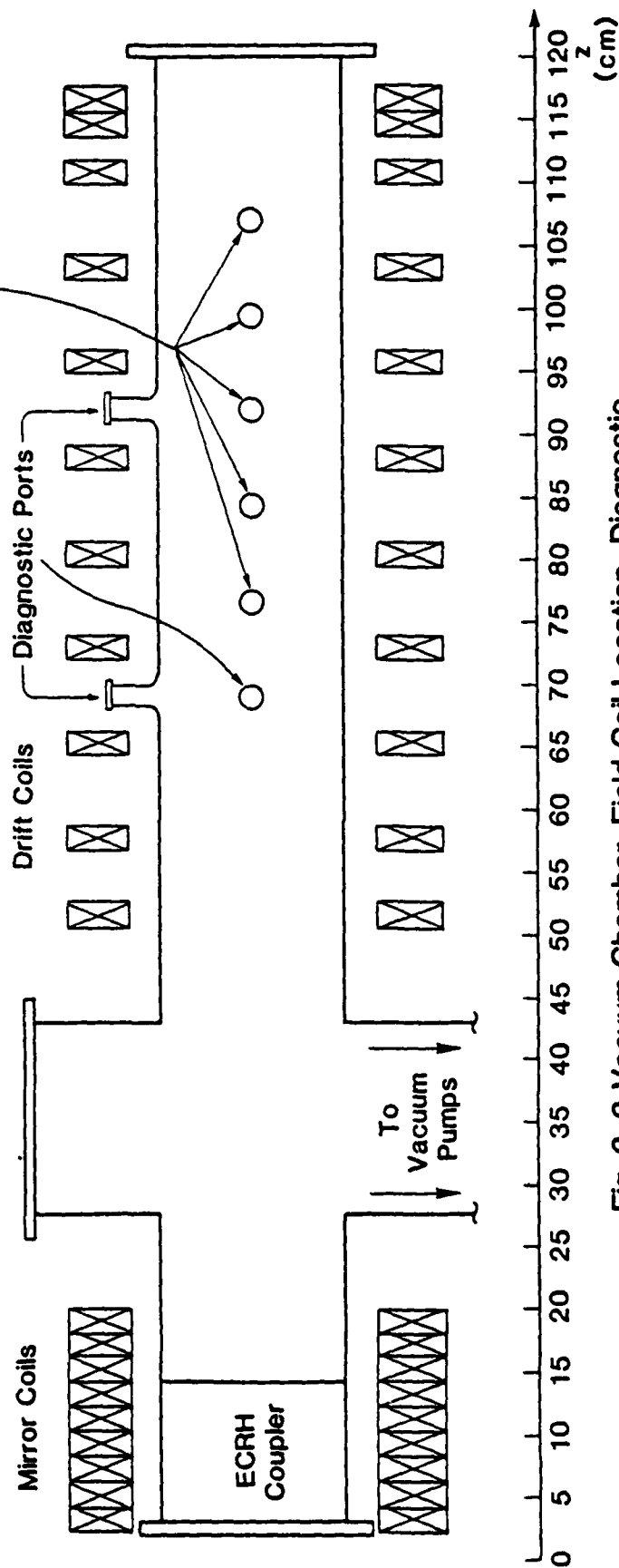


Fig. 2-2 Vacuum Chamber, Field Coil Location, Diagnostic Port Locations and RF Slow Wave Structure Coupling Ports.

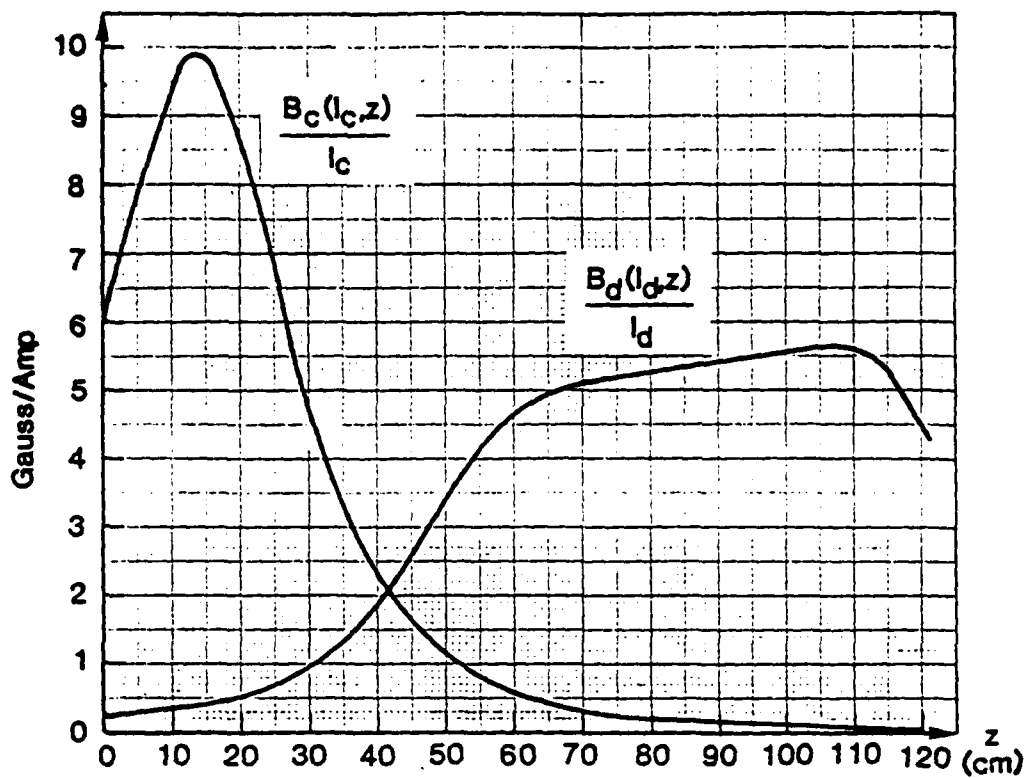


Fig. 2-3 Axial Magnetic Field per Unit Current Profiles for Coupler Coils and Drift Coils.

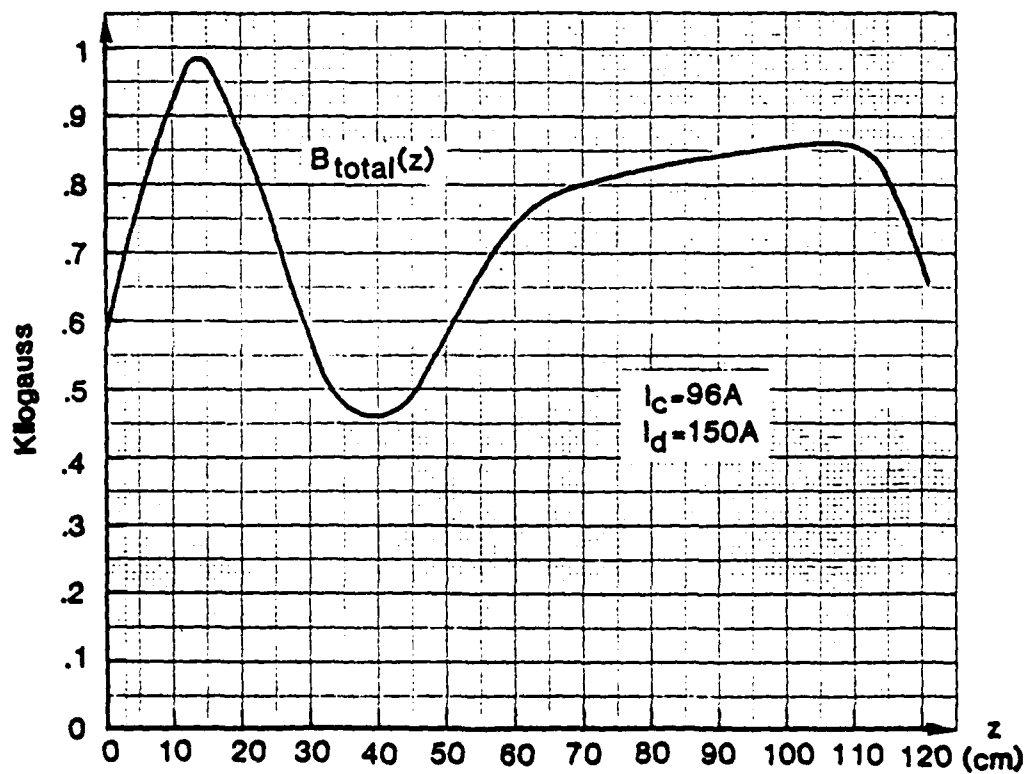


Fig. 2-4 Total Magnetic Axial Field Profile for $I_c = 96A$ $I_d = 150A$.

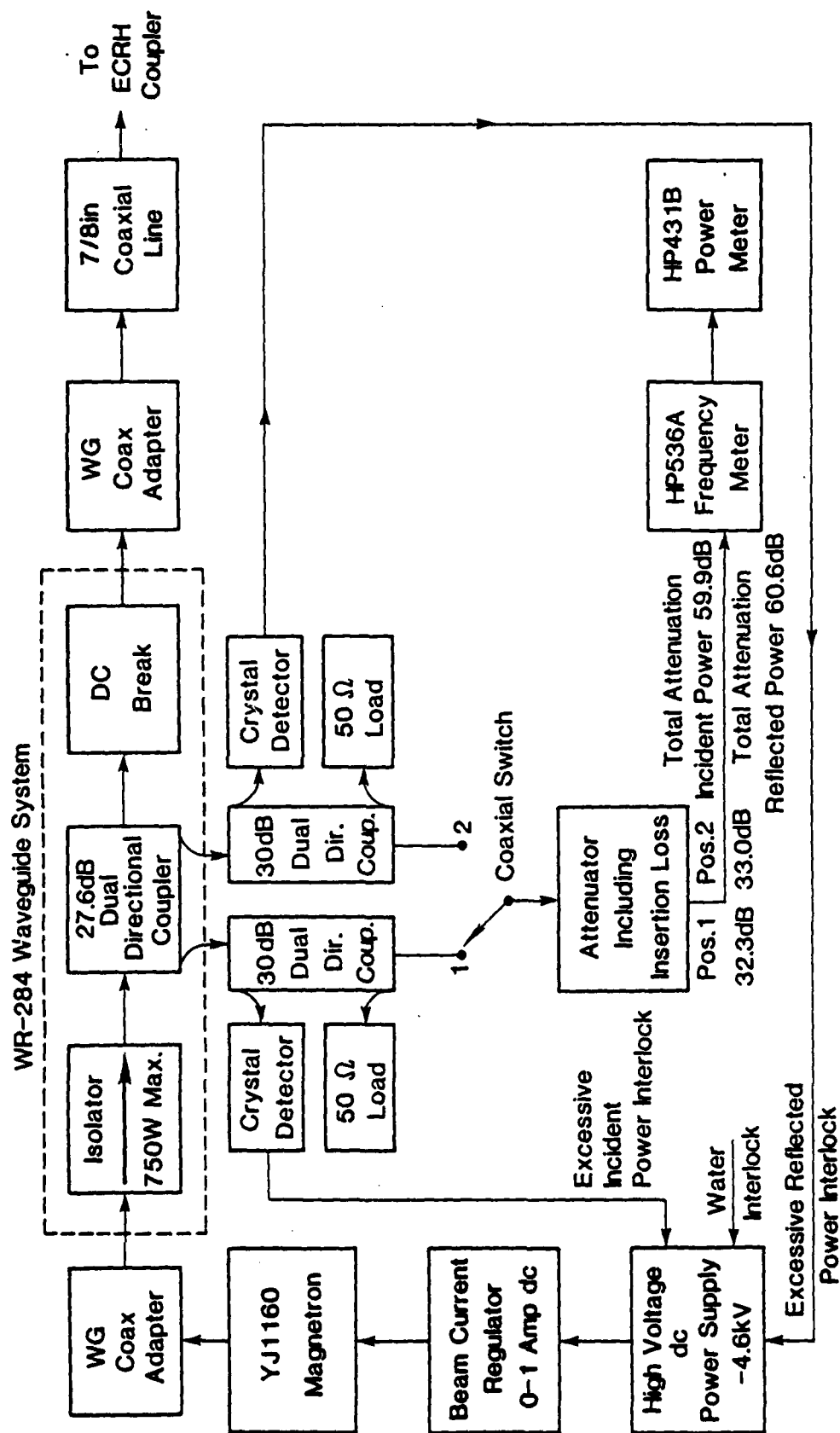


Fig. 2-5 ECRH Microwave System

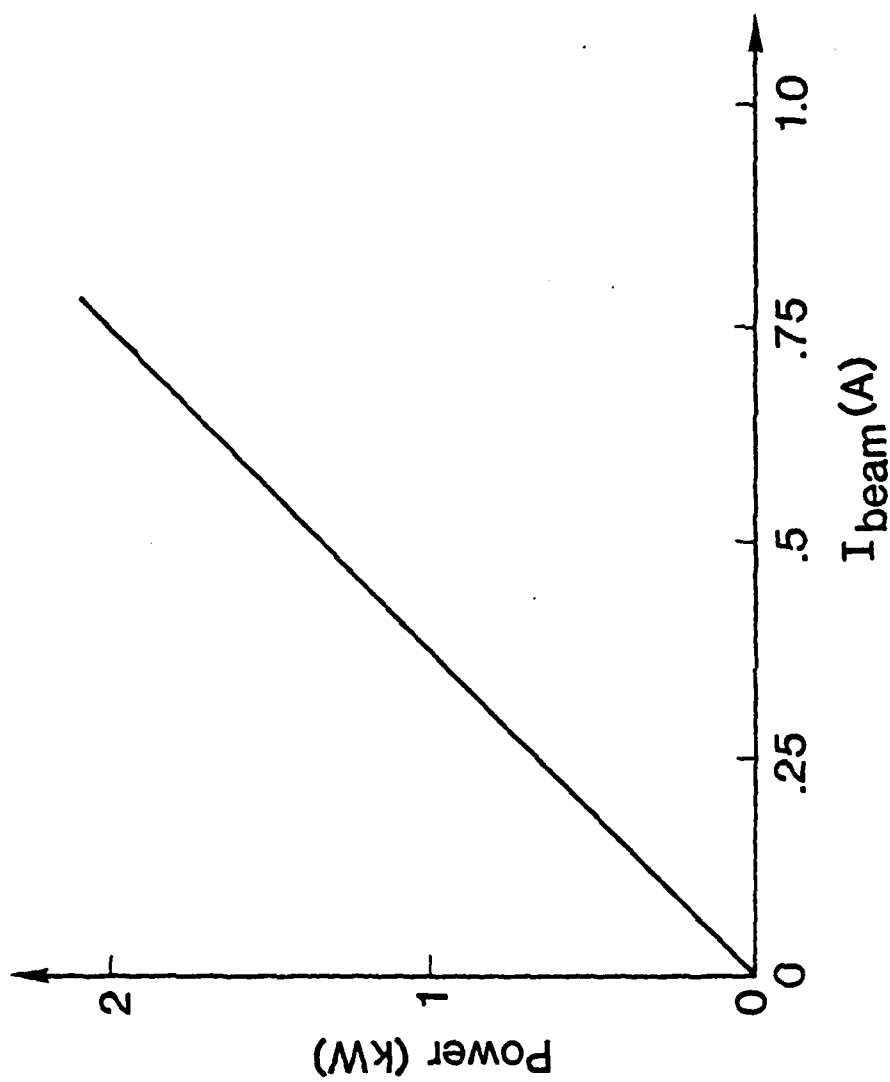


Fig. 2-6 Magnetron Output Characteristic.

coupler. The low power branches on the directional coupler are used to monitor incident and reflected microwave power as well as to detect excessive incident or reflected microwave power. The detection circuits shut down the high voltage power supply if the incident or reflected power exceeds 750 W. Incident and reflected microwave powers are monitored by an HP model 431B power meter measured through 59.9 dB and 60.6 dB of attenuation respectively. An HP model 536A frequency meter is used to determine the microwave frequency. A coaxial switch is used to select which directional coupler branch is connected to the power meter. The main branch of the directional coupler is connected to a 7/8" coaxial line through a waveguide-coax adapter. The 7/8" coaxial line is brought into the vacuum chamber through a 7/8" coaxial pressure seal and tapered to the microwave energy coupler used to generate the plasma. The microwave energy coupler will be discussed in the next section. A thin teflon waveguide section 1.59 mm thick is inserted between the last two waveguide sections to isolate the reference electrode from ground (see Fig. 2-1).

2.5 Microwave Energy Coupler

ECRH is achieved by coupling electromagnetic energy into the plasma at the electron cyclotron frequency using a Lisitano^{14,15} coil. The Lisitano coil has been used previously in this laboratory by Chrisner¹⁶ in a study of electron cyclotron resonance plasmas and by Kudyan¹⁷ in a study of transverse instabilities in a hollow plasma column. The microwave energy coupler is shown in Fig. 2-7 and the physical dimensions of the coupler are shown in Fig. 2-8. The overall assembly of the microwave energy coupler is shown in Fig. 2-9. As shown in Figs. 2-7 and 2-8 the energy coupler consists of an open ended thin copper cylinder with 16 axially oriented slots uniformly distributed over the cylinder. These axial slots are alternately connected together by short azimuthal slots at each end of the cylinder forming one continuous slot around the cylinder. The first slot is connected by a fin-line adapter to the coaxial line through a boron-nitride vacuum seal. Boron nitride was chosen for the vacuum seal because of its ability to withstand the

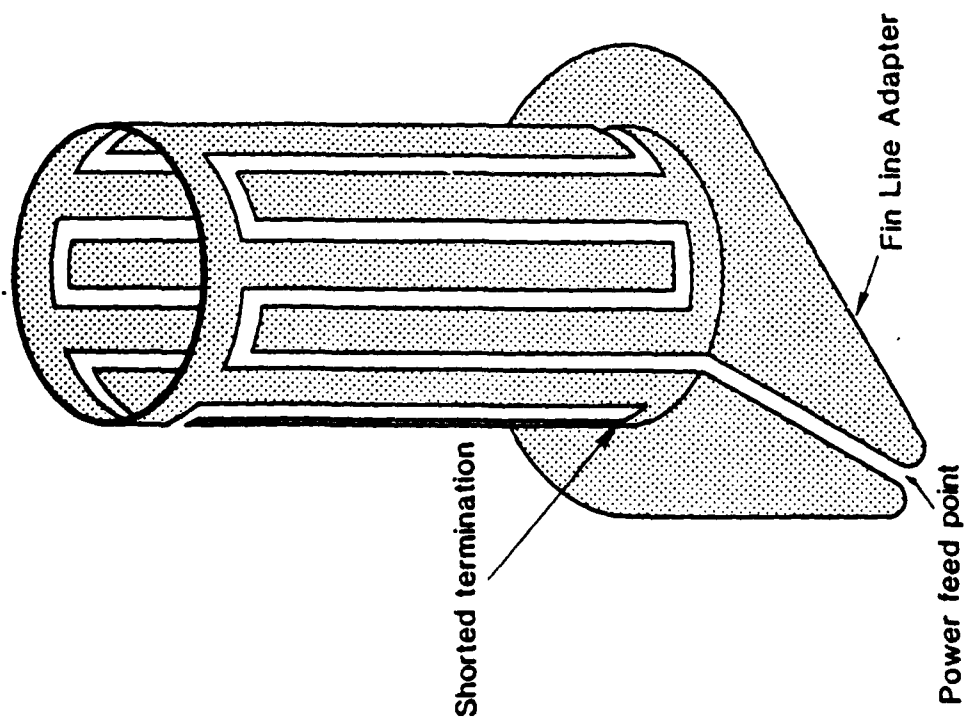
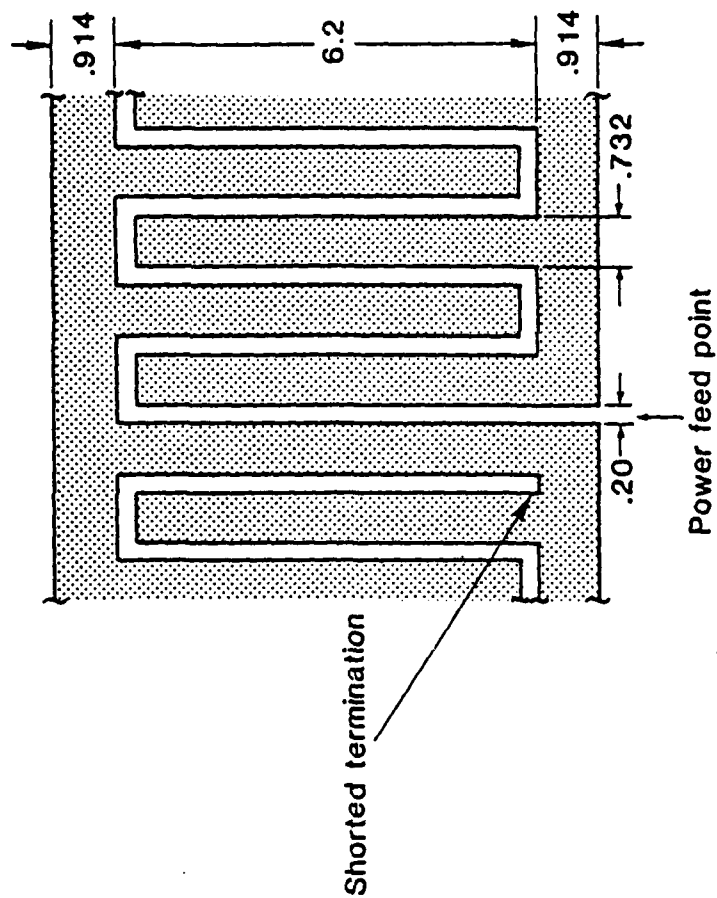
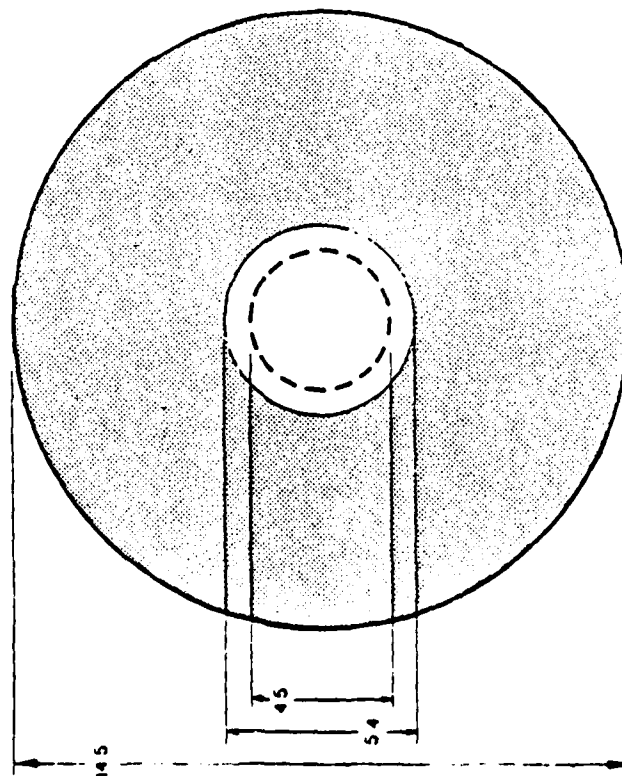


Fig. 2-7 Lisitano Coil

Fig. 2-8 Physical Dimensions of Lisitano Coil
(Dimensions in centimeters)

(Front View)



(Side View)

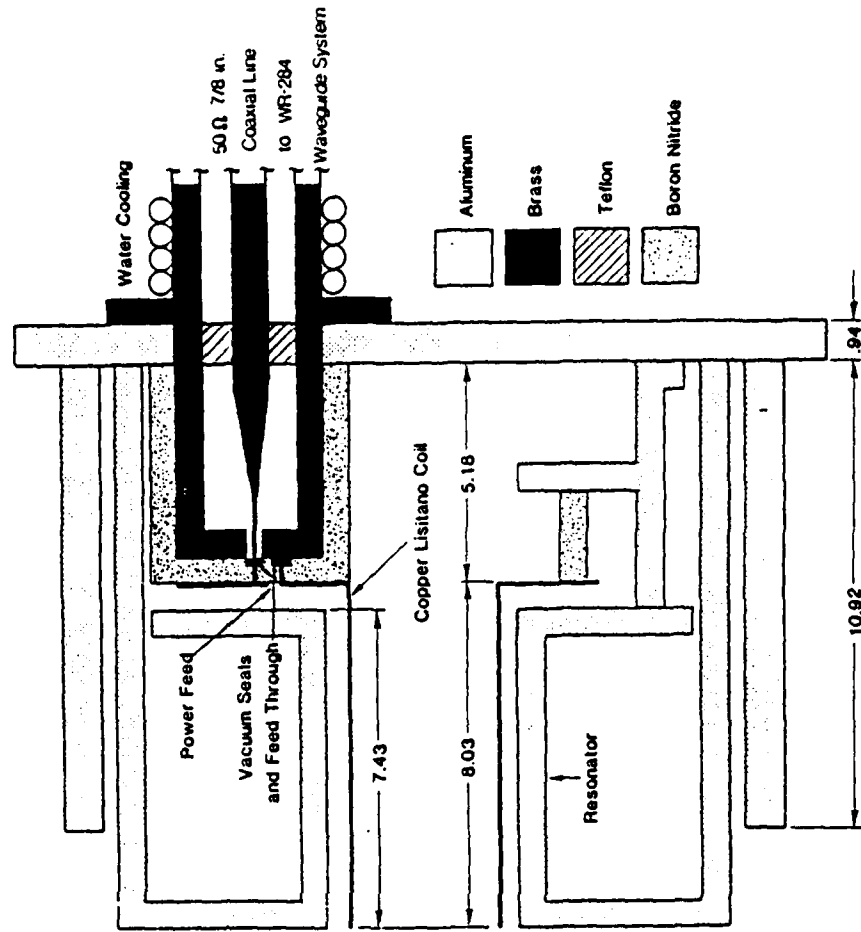


Fig. 2-9 Overall Assembly of Microwave Energy Coupler
(Dimensions in Centimeters) (Not to Scale)

large quantities of heat generated by the discharge. The last slot is terminated in a short circuit. The length of each axial slot is a half wavelength long at the applied microwave frequency (2.45 GHz). Without a plasma, the microwave energy is guided along the slots to the shorted termination where it is reflected establishing an azimuthal electric field within the cylinder with a maximum standing wave voltage in the central cross section of the cylinder. The electric field configuration is shown in Fig. 2-10.

After a plasma is established, microwave energy is absorbed by ECRH as the wave propagates along the slots and the reflected power is determined by the state of the plasma. In turn, the state of the plasma is determined by the coupler region magnetic field, the drift magnetic field, and the neutral gas pressure.

2.6 RF System and Slow Wave Structure

Fig. 2-11 is a schematic diagram of the 3.25 MHz rf system used to excite low phase velocity electrostatic waves in the plasma. RF power at 3.25 MHz is produced by an rf transmitter capable of delivering up to 5 kW cw. The output power amplifier consists of two parallel connected, grid driven Eimac 750 TL power triodes operated class C. The power amplifier output is connected to a pi-L network which tunes the transmitter frequency and adjusts the power transfer from the transmitter to the load impedance. The transmitter output is connected to a 5 kW, wideband (2MHz - 30 MHz), 1:1, ferrite core balanced transformer which is in turn connected to two 50 Ω (RG-8/u) delay lines which phases adjacent elements of the slow wave structure 90° apart as shown in Figs. 2-11 and 2-12. Two power meters on the output of the transmitter monitor the output power of the transmitter and the reflected power from the rf coupling system. The other ends of the two slow wave structure delay lines are terminated by 50 Ω loads each capable of dissipating 2.5 kW. These 50 Ω terminations eliminate reflections on the slow wave structure. The rf load currents are monitored on an oscilloscope or an rf spectrum analyzer by two model 411

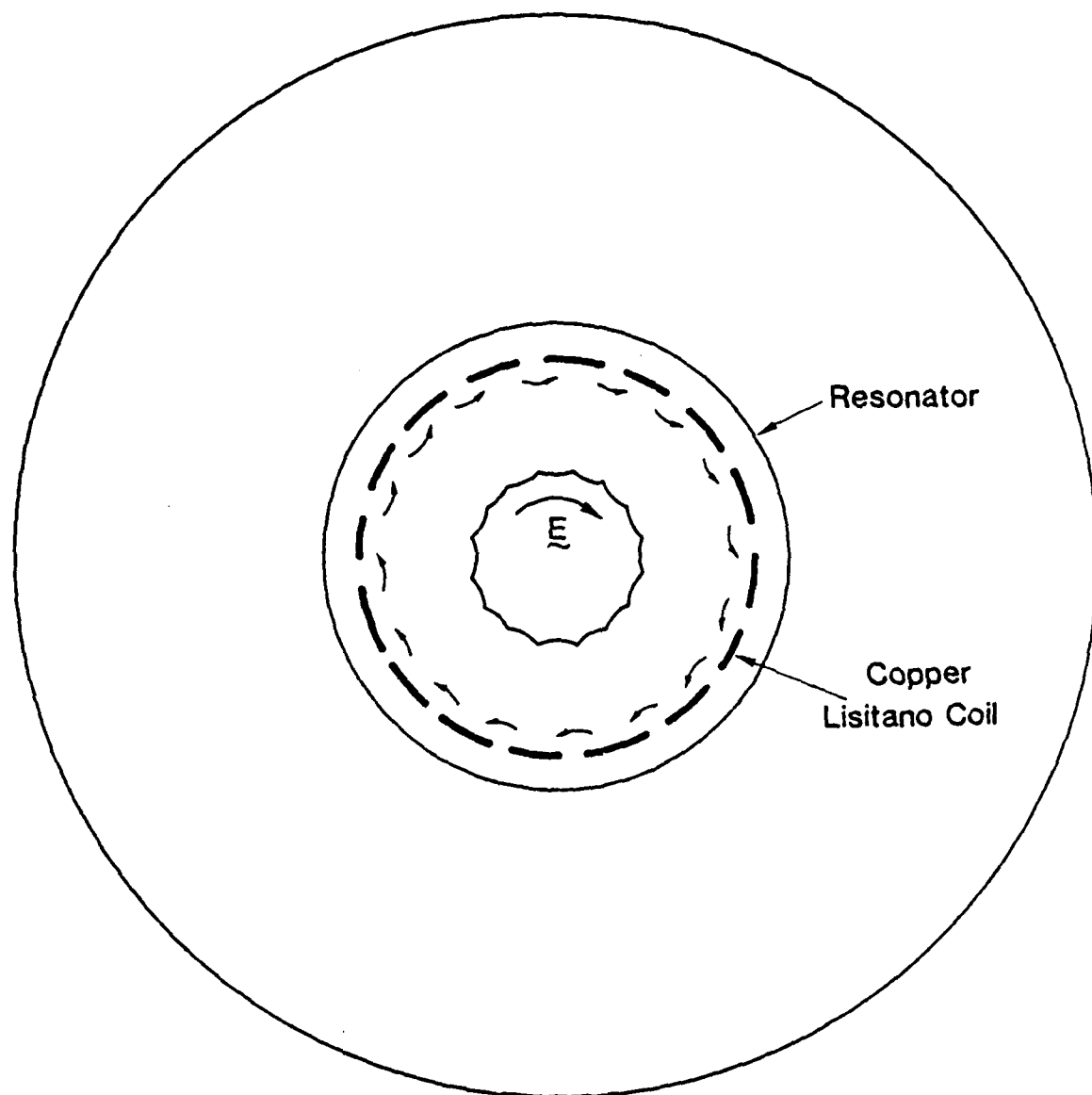


Fig. 2-10 Electric Field Configuration of Microwave Energy Coupler.

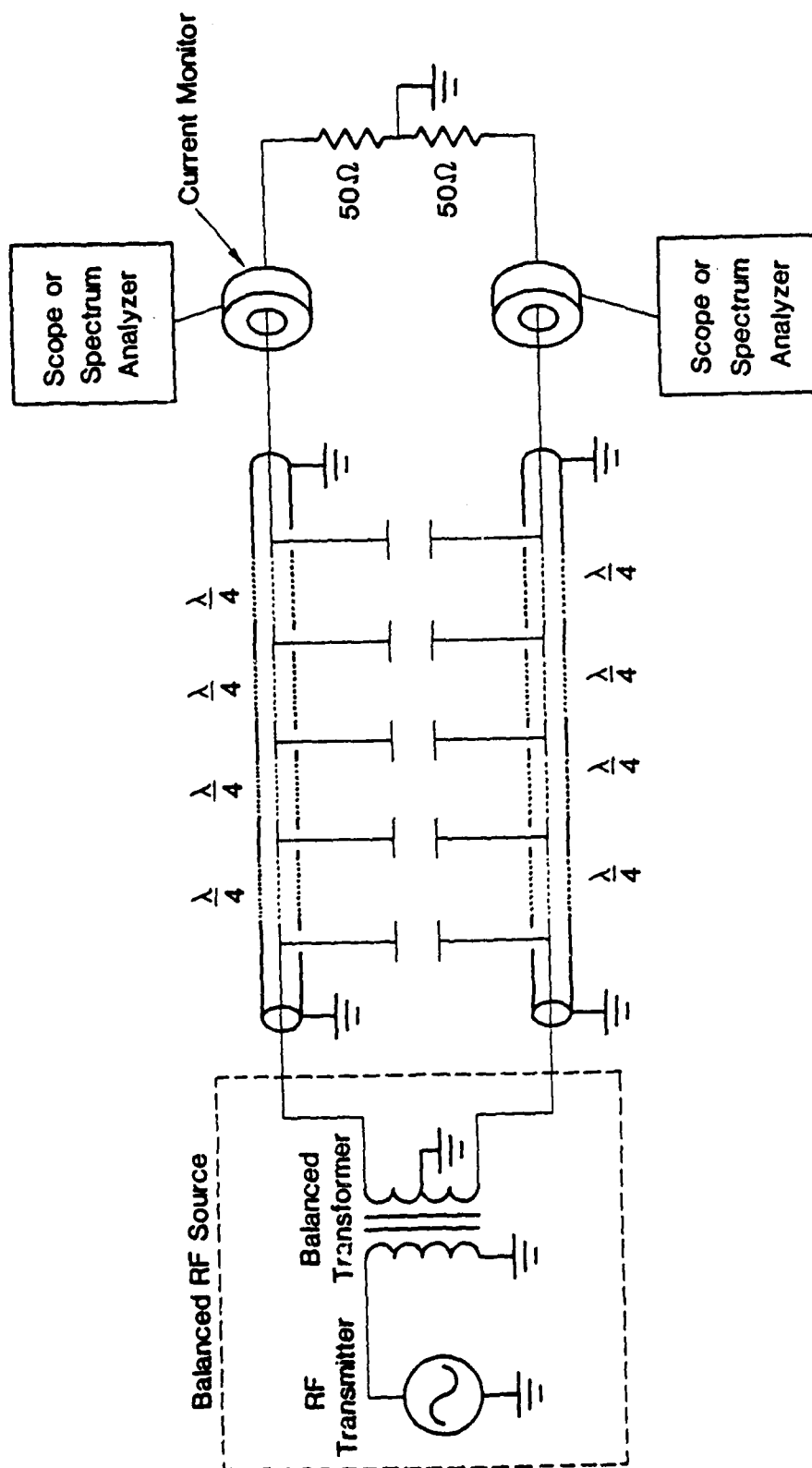


Fig. 2-11 Schematic of Low Frequency RF System and Slow Wave Structure

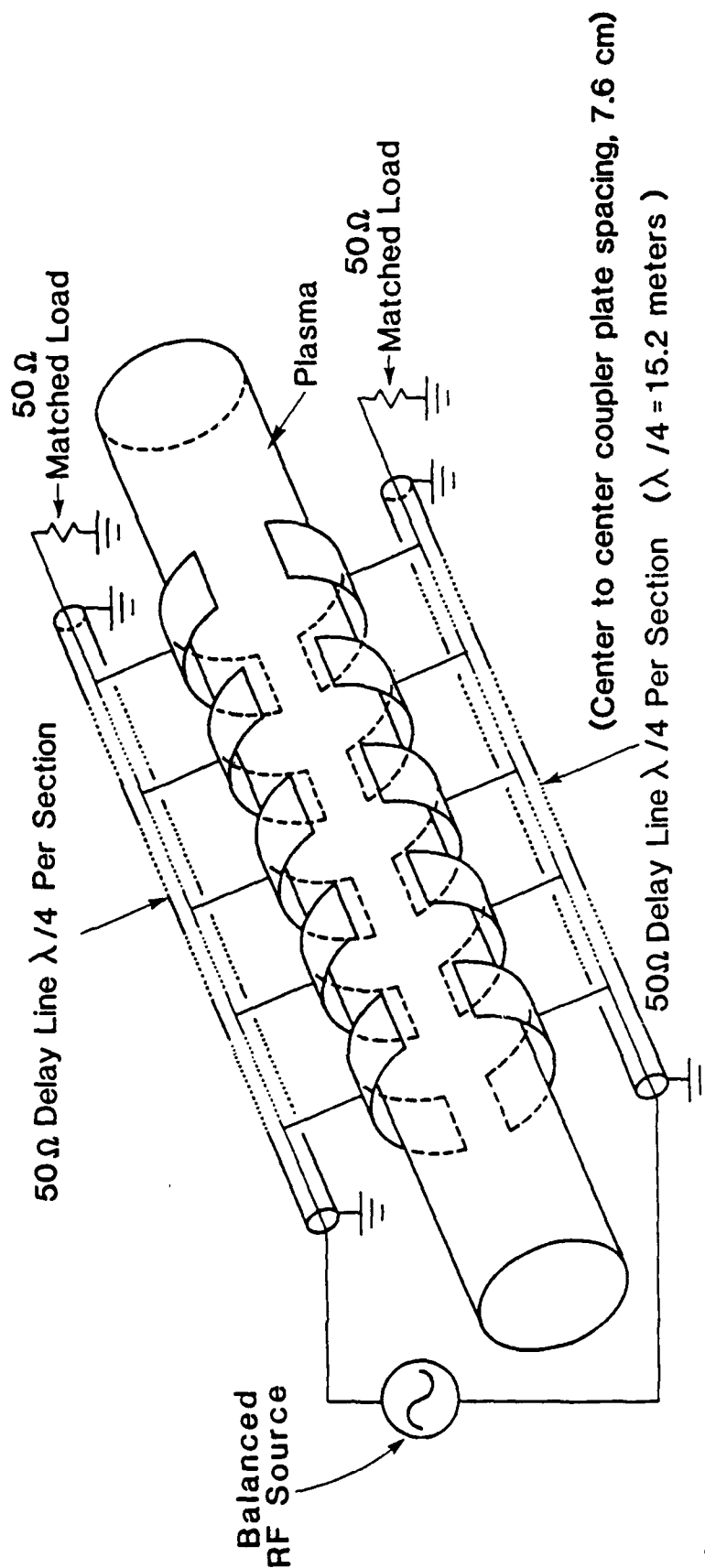


Fig. 2-12 Pictorial Representation of Slow Wave Structure

Pearson wideband (1 Hz - 33 MHz) current monitors with a 50Ω output impedance. The current monitors produce an output voltage of 100 mV into an open circuit with an input current of 1A. The rf spectrum analyzer consists of an HP 141S oscilloscope with two spectrum analyzer plug-in units; an HP 8553L RF unit and an HP 8552A IF unit. The spectrum analyzer is capable of displaying rf spectra from 1 kHz to 110 MHz. Fig. 2-13 shows the rf spectrum of the transmitter output. The rf output and terminating loads on the delay lines can be interchanged so either an $e^{ik_z z}$ or an $e^{-ik_z z}$ excitation can be established on the slow wave structure.

The copper coupling plates have a radius of 5.1 cm, a length of 3.8 cm and subtend an angle of 90° as shown in Fig. 2-14. The longitudinal separation of adjacent plate edges is 3.8 cm with a center-to-center spacing of 7.6 cm. The azimuthal angle subtended by corresponding coupling plates on delay line 1 and delay line 2 is 90° . The edge of the last plate is located approximately 12.7 cm from the end-plate of the experiment.

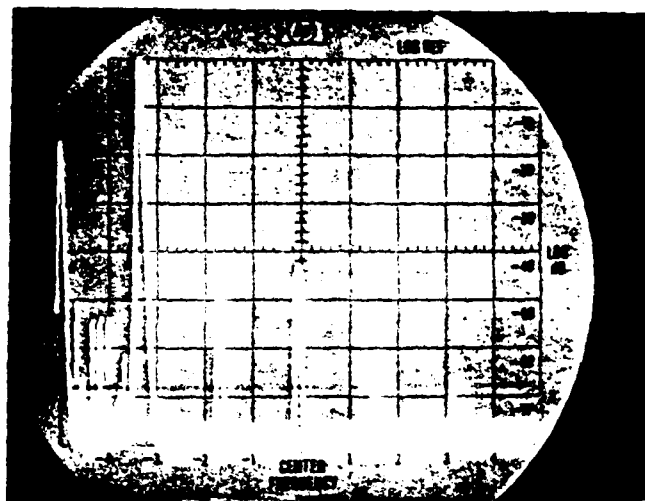


Fig. 2-13 RF Spectrum of Transmitter Output

First peak on left edge is the zero reference

Log vertical scale

2 MHz/division horizontal scale

Signal frequency 3.25 MHz

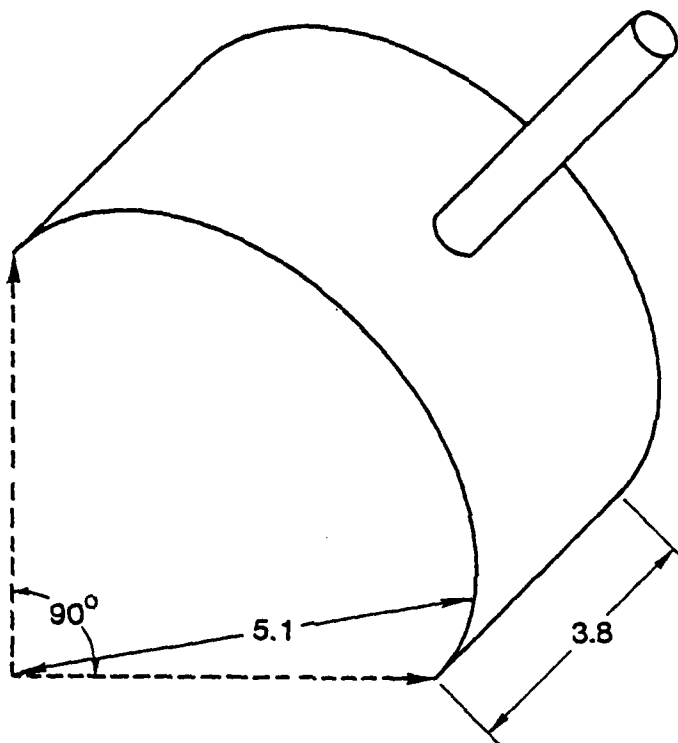


Fig. 2-14 Dimensions of Coupling Plates of Slow Wave Structure.

(All dimensions in centimeters)

Chapter 3

PLASMA DIAGNOSTIC SYSTEMS

3.1 General Description

A variety of diagnostic systems are employed to investigate plasma parameters as well as the interaction of the plasma with electrostatic waves excited by the slow wave structure. The diagnostic systems, which will be discussed in this chapter, consist of: (1) electrostatic (Langmuir) probes, (2) dc current probes, (3) rf probes, and (4) electrostatic energy analyzer.

Fig. 3-1 shows the basic diagnostic systems used, and Fig. 3-2 shows the locus of the radial and azimuthal probe paths. The positions of the radially and azimuthally movable probes are accurately determined by mechanically coupling the probe assembly to a 10-turn, 1 k Ω helipot. The wiper of the helipot gives a voltage proportional to the angle of the probe and this voltage is used to drive the x-axis of an x-y recorder as shown in Fig. 3-3.

3.2 Electrostatic Probes

Electrostatic probes are frequently used for the localized measurement of electron temperature, electron number density, and plasma potential in low pressure discharges. The theories of electrostatic probes are well documented^{18, 19, 20, 21} and only the relevant equations will be given here.

The construction of a cylindrical electrostatic probe is shown in Fig. 3-4 and the electronic system used for measurements of the probe characteristic and the radial profile of ion saturation current is shown in Fig. 3-5. Fig. 3-6 shows a typical probe characteristic. The electron current can be extracted from the total probe current when $\Delta\phi < 0$, where

$$\Delta\phi = \phi - \phi_p \quad (3.1)$$

Here, ϕ and ϕ_p represent the probe potential and the plasma potential, respectively. When $\Delta\phi < 0$, that is, in the potential range where electrons are being repelled, the electron current is given by

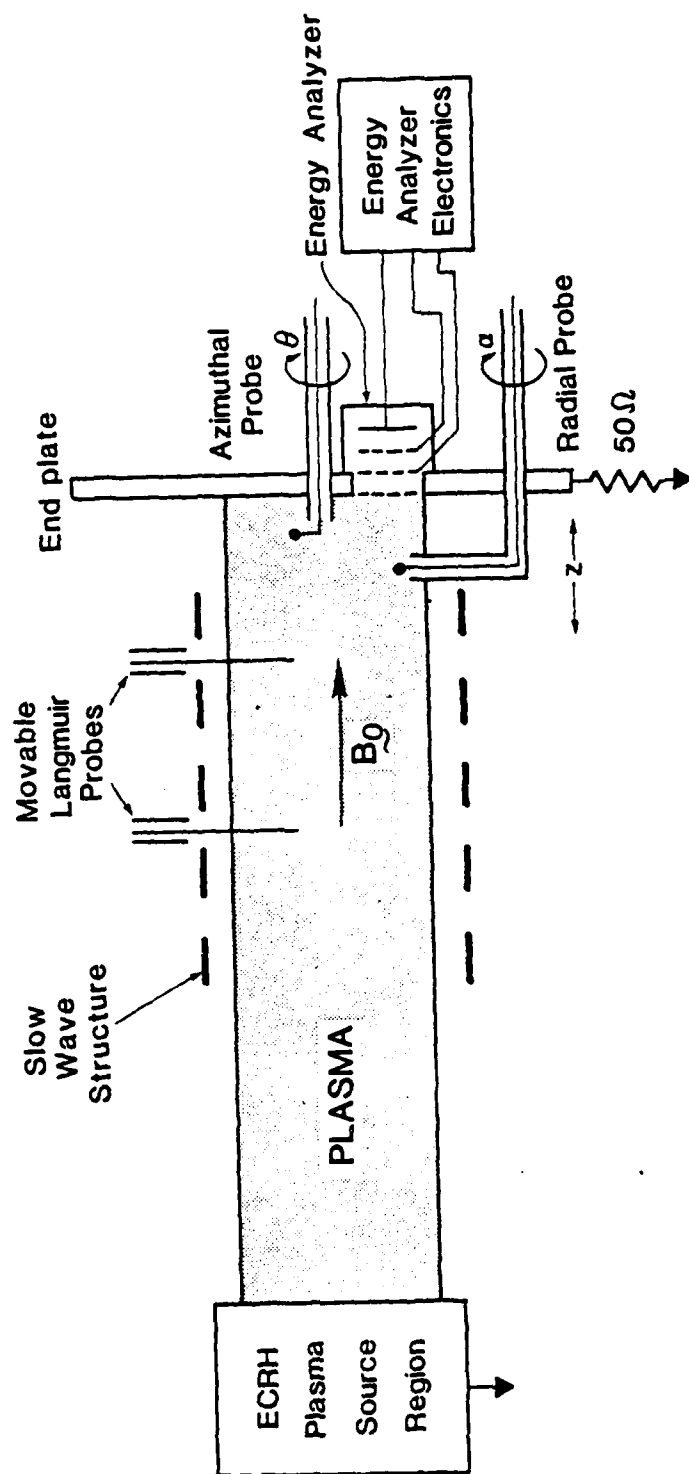


Fig. 3-1 Basic Diagnostic Setup

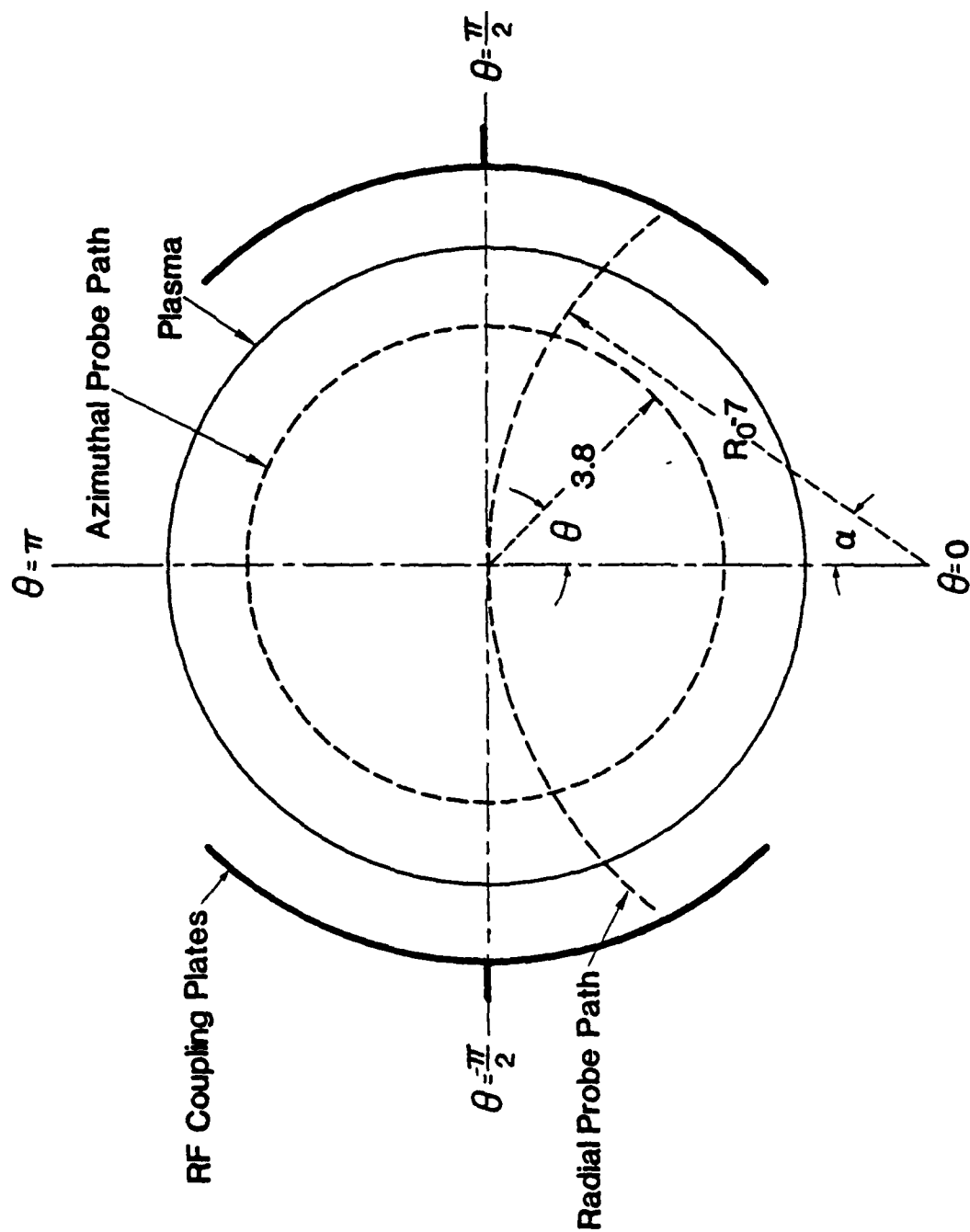


Fig. 3-2 Locus of Radial and Azimuthal Probe Paths
(All Dimensions in Centimeters)

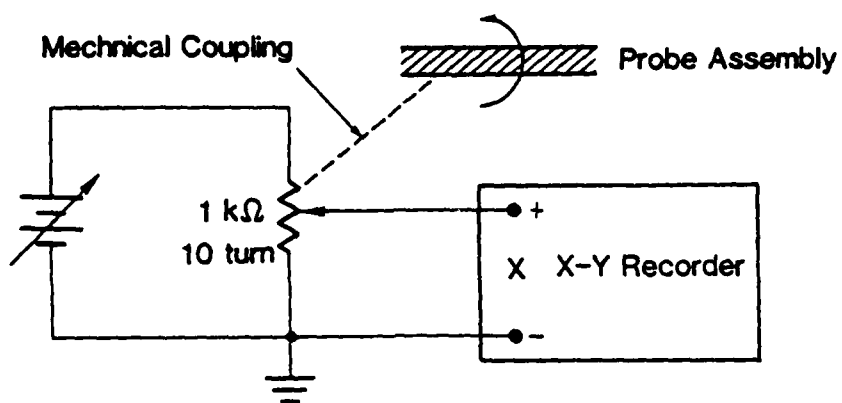


Fig. 3-3 Circuitry for Probe Positioning Assembly

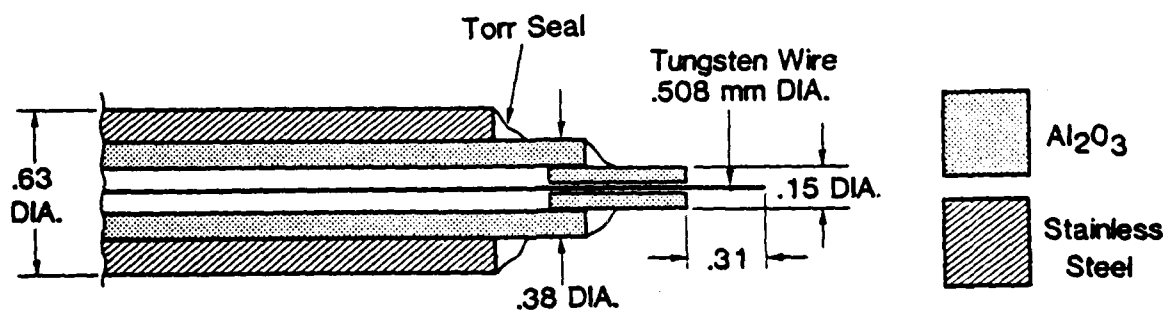


Fig. 3-4 Construction of Langmuir Probe
(Dimensions in Centimeters)

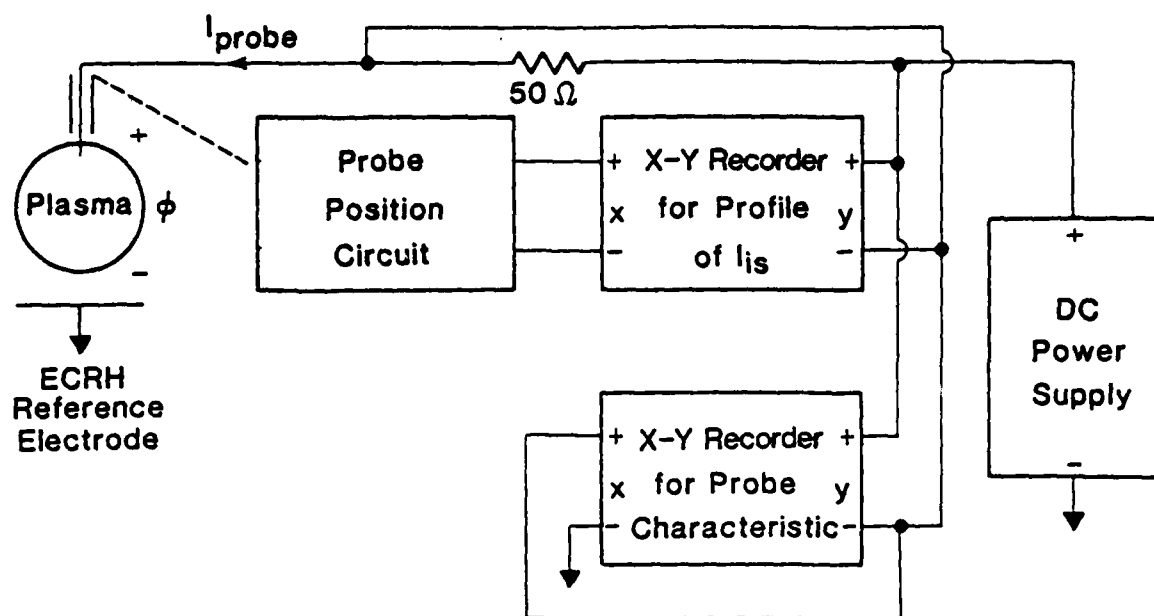


Fig. 3-5 Electronic Circuit for Langmuir Probe Measurements

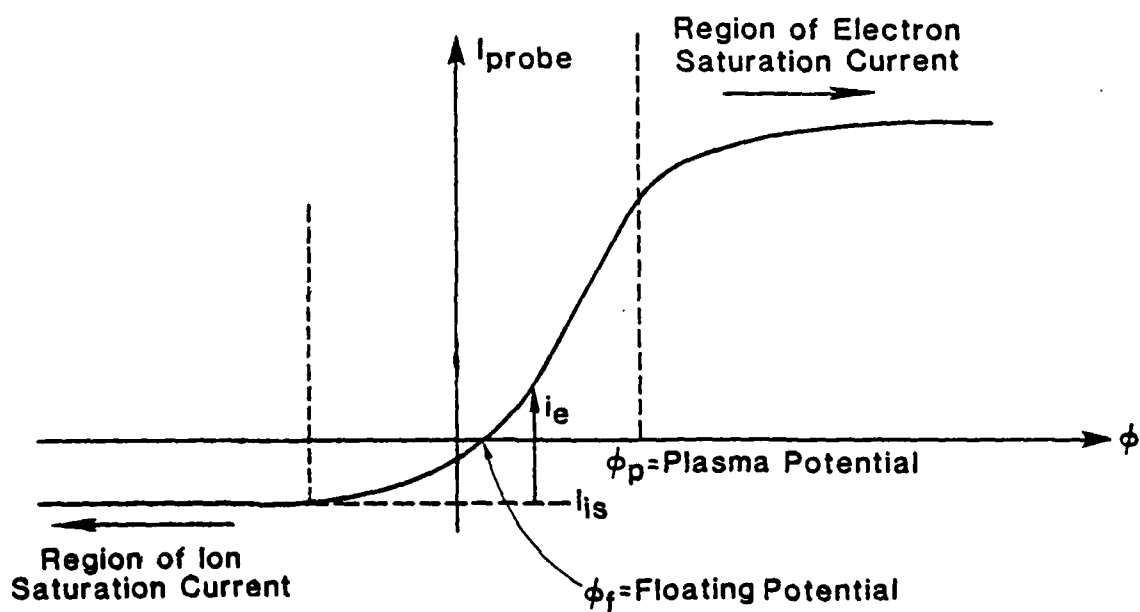


Fig. 3-6 Typical Langmuir Probe Characteristic

$$i_e = en_e A'_p \left(\frac{k_B T_e}{2\pi m_e} \right)^{1/2} e^{\Delta\phi/k_B T_e} \quad (3.2)$$

where n_e is the electron number density and $k_B T_e/e$ is the electron temperature in eV. A'_p represents the electron current collection area. Since the electron current is constrained to flow along the background magnetic field B_0 , the electron collection area is approximated by the projection of the probe area on a plane perpendicular to B_0 rather than by the real probe area. If d is the probe diameter and l is the probe length, the electron collection area A'_p is given by

$$A'_p = 2dl \quad (3.3)$$

From Eq. (3.2) it is found that

$$\frac{d}{d\phi} (\ln i_e) = \left(\frac{k_B T_e}{e} \right)^{-1} \quad (3.4)$$

A plot of $\ln(i_e)$ versus ϕ yields a straight line whose slope determines the electron temperature. The electron number density can then be determined by Eq. (3.5).

$$i_e(\phi_p) = en_e A'_p \left(\frac{k_B T_e}{2\pi m_e} \right)^{1/2} \quad (3.5)$$

The magnitude of the ion saturation current, $|I_{is}|$ is proportional to $n_e (k_B T_e)^{1/2}$ and the radial profile of this quantity in conjunction with probe characteristics at various radii, yield valuable information about the radial inhomogeneity of the plasma. These characteristics are also measured at various axial locations in the plasma to obtain information about the axial inhomogeneity of the plasma.

3.3 DC Current Probes

To obtain some information about the relative axial electron flux over the cross section of the plasma, both radial and azimuthal current probes are used near the endplate of the experiment. The construction of these current probes are shown in Fig. 3-7 and the measurement circuit is shown in Fig. 3-8. The normal to the surface of the current probes are oriented parallel to B_0 so the axial component of electron flux is measured. The diameter of the circular

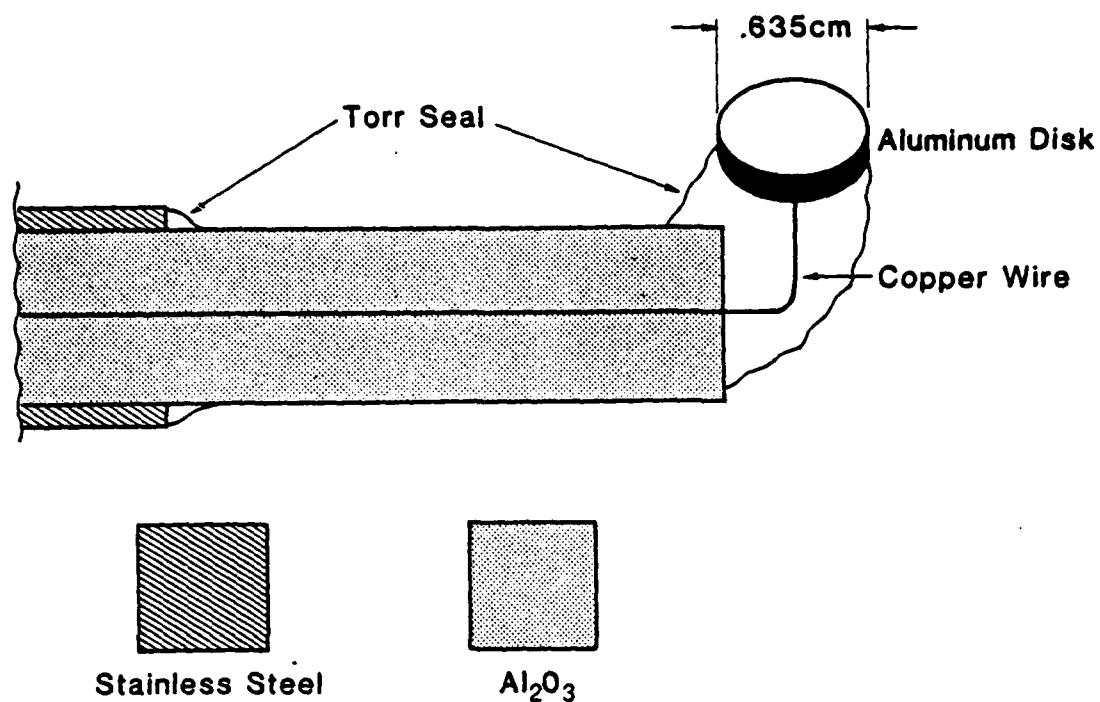


Fig. 3-7 Construction of DC Current Probe

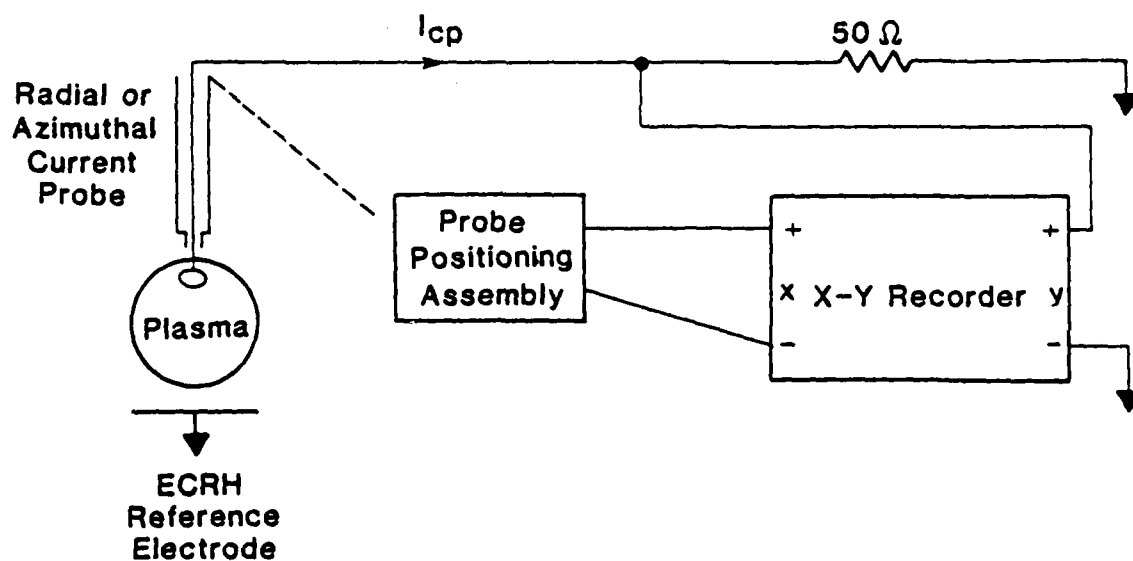


Fig. 3-8 Electronic Circuit for DC Current Profile Measurements

current probes are made small so as to increase the spatial resolution of the probes. The probe diameter is 0.635 cm. The local electron current density can be approximated by $J_{ez} = I_{cp} / A_{cp}$ where I_{cp} is the measured current through the external 50Ω current sensing resistor and A_{cp} is the cross sectional area of the probe. In general, J_{ez} is a function of r and θ , however the azimuthal position of the radially movable current probe is not independent of the probe angle α . Because of this it is not possible to extract the radial dependence of J_{ez} at a fixed azimuthal position. It is found however, that the θ dependence of J_{ez} is nearly constant in the azimuthal range of θ near the coupler plates ($\frac{\pi}{4} \leq \theta \leq \frac{3\pi}{4}$, $-\frac{3\pi}{4} \leq \theta \leq -\frac{\pi}{4}$) and hence the α dependence of J_{ez} can be separated from the θ dependence. The total current picked up by the endplate of the device is determined by the integration of the local current density over the cross section of the plasma

$$I_{e,total} = \int_0^{2\pi} \int_0^{r_p} r J_{ez}(r, \theta) dr d\theta \quad (3.6)$$

where r_p is the plasma radius.

From the geometry indicated in Fig. 3-2 the radial position of the probe is related to the probe angle α by,

$$r = 2R_o \sin \frac{\alpha}{2} \quad (3.7)$$

where R_o is the radius of the arc swept out by the probe. Eq. (3.7) is also used to relate r and α in the Langmuir probe and rf probe measurements. A change of variables from (r, θ) to (α, θ) can be applied to Eq. (3.6) yielding

$$I_{e,total} = \int_0^{2\pi} \int_0^{\alpha_{max}} 2R_o \left(\sin \frac{\alpha}{2}\right) J_{ez}(\alpha, \theta) \frac{\partial(r, \theta)}{\partial(\alpha, \theta)} d\alpha d\theta \quad (3.8)$$

where $\frac{\partial(r, \theta)}{\partial(\alpha, \theta)}$ is the Jacobian of the transformation $(r, \theta) \rightarrow (\alpha, \theta)$. The Jacobian is defined by

$$\frac{\partial(r, \theta)}{\partial(\alpha, \theta)} = \begin{vmatrix} \frac{\partial r}{\partial \alpha} & \frac{\partial \theta}{\partial \alpha} \\ \frac{\partial r}{\partial \theta} & \frac{\partial \theta}{\partial \theta} \end{vmatrix} = R_o \cos \frac{\alpha}{2} \quad (3.9)$$

Hence,

$$I_{e, \text{total}} = \int_0^{2\pi} \int_0^{\alpha_{\text{max}}} R_o^2 J_{ez}(\alpha, \theta) \sin \alpha d\alpha d\theta \quad (3.10)$$

where α_{max} is defined by Eq. (3.11).

$$\alpha_{\text{max}} = 2 \sin^{-1} \left(\frac{r_p}{2R_o} \right) \quad (3.11)$$

The externally measured current received by the current probe is influenced by the characteristics of the plasma, which is in turn influenced by the structure of the electromagnetic fields exciting the plasma. These measurements, in conjunction with the electrostatic energy analyzer measurements give a variety of information regarding the axial electron flux and the axial electron energy distribution as a function of the rf power exciting the slow wave structure. Experimental results and their interpretation will be discussed in chapters 4 and 5 respectively.

3.4 RF Probes

RF probes have been extensively used in plasma physics experiments to investigate amplitude and phase characteristics of waves in plasma. For example, rf probes have been used by Briggs and Parker²² in the study of the coupling of rf energy to lower hybrid waves, Fisher and Gould²³ in the investigation of the formation of resonance cones in plasmas, Bellan and Porkolab¹² in the study of the excitation of lower hybrid waves using a slow wave structure, and Hooke and Bernabei⁷ in the observation of propagating lower-hybrid waves.

The rf probe is constructed as shown in Fig. 3-9. As can be seen in the figure the probe is doubly shielded (triaxial) with the outer stainless steel tube providing the vacuum seal. The stainless steel tube is inserted through a probe port in the endplate of the device which allows probe motion along z and can rotate the probe in α . The coaxial

probe tip is sealed in an alumina (Al_2O_3) insulating shield which prevents the probe from drawing current from the plasma. The amplitude and phase of the rf potential can be measured using the electronic system illustrated in Fig. 3-10. The probe output is connected to an HP model 8405A vector voltmeter and a 50Ω termination located at the vector voltmeter signal input. A reference signal is applied through a Tektronix P6012, 10X probe from one of the slow wave structure coupler plates (see Fig. 3-10) to the reference channel on the vector voltmeter. The vector voltmeter measures the amplitude of the probe signal and the phase difference between the probe and reference at the frequency of the reference signal. Two dc output voltages are available from the vector voltmeter; one is proportional to the amplitude of the probe signal and the other is proportional to the phase difference between the probe and the reference. Each of these voltages is applied to the y-axis of two x-y recorders and the x-axes are driven by the probe position assembly described in section 3.1. Using this method one can accurately map the amplitude and phase of the rf potential as a function of α in the plasma. These measurements are then made at various axial locations to determine amplitude and phase characteristics along the plasma column. The axial position is measured simply by using an accurate caliper.

Care must be taken in the interpretation of the phase characteristics since the vector voltmeter only measures phase differences between -180° and $+180^\circ$. If the phase varies by more than 360° the phase output of the vector voltmeter may change discontinuously and this must be distinguished from a rapid physical change in phase. Fortunately, the phase changes are generally less than 360° across the plasma column and this problem is not experienced. The vector voltmeter also possesses a phase offset control so it is possible to bias the phase output at a convenient point so as to avoid the 'ends' of the phase range on the vector voltmeter where the phase output may change discontinuously. When making phase measurements it is important to record the value of the phase offset to make comparisons between measurements.

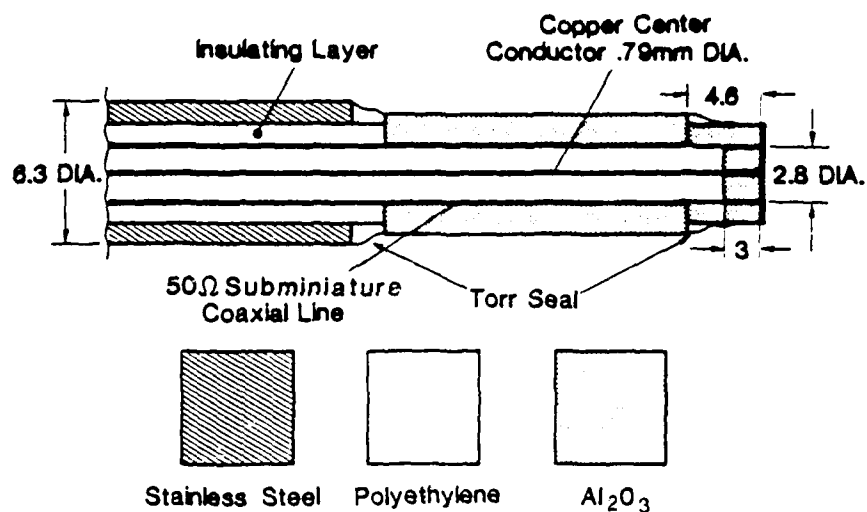


Fig. 3-9 Construction of RF Probe
(Dimensions in Millimeters)

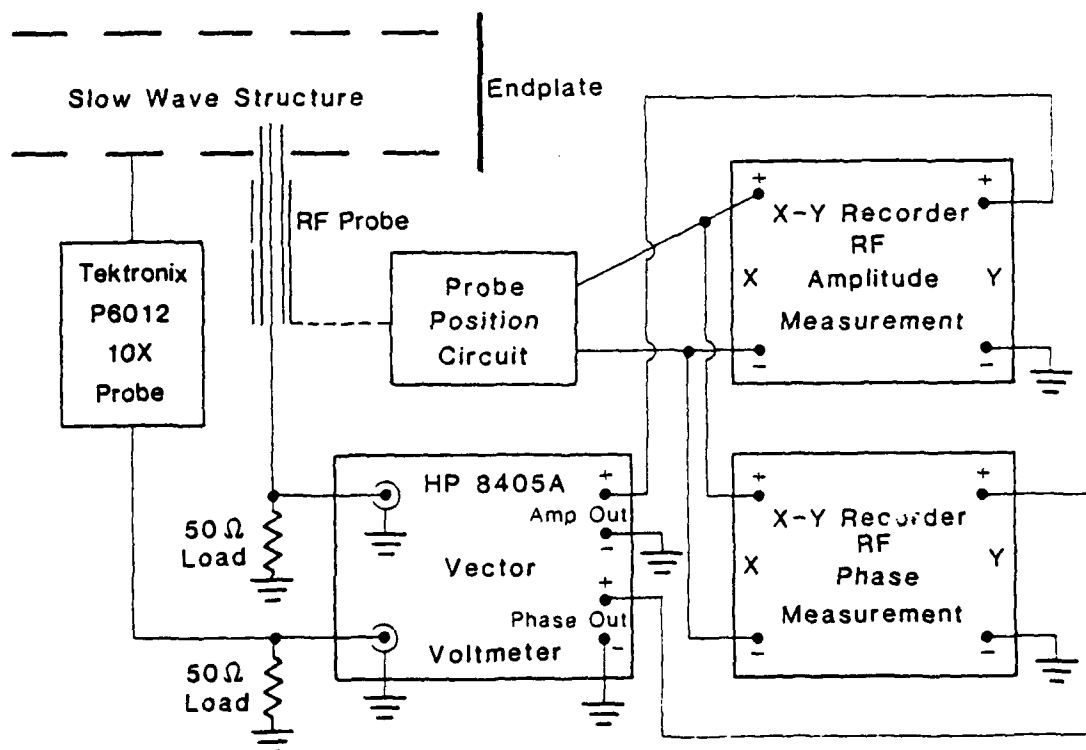


Fig. 3-10 Electronic Circuit for Amplitude and Phase Measurements of RF Potential

From the measured phase variation as a function of α , $\psi(\alpha)$, it is possible to determine the local radial wave number $k_r(r)$. The radial wave number can be readily deduced assuming a small phase variation in the azimuthal direction near the coupler plates as discussed in conjunction with the current probes in section 3.3. The radial wave number is determined from the phase information by Eq. (3.12)

$$k_r(r) = \frac{d}{dr} \psi(r) \quad (3.12)$$

where $r = r(\alpha)$ is defined in Eq. (3.7), $k_r(r)$ can be written as,

$$k_r(r) = \frac{d\psi}{d\alpha} \frac{d\alpha}{dr} \quad (3.13)$$

From Eq. (3.7) we find

$$\frac{dr}{d\alpha} = R_o \cos \frac{\alpha}{2}.$$

Hence,

$$k_r(r) = \frac{1}{R_o \cos \frac{\alpha}{2}} \left(\frac{d\psi}{d\alpha} \right), \quad \alpha \neq \pm \pi \quad (3.14)$$

3.5 Retarding Field Electrostatic Energy Analyzer

The retarding field electrostatic energy analyzer has been used in plasma physics experiments for the measurement of charged particle distribution functions and distribution function modification due to the presence of waves in the plasma. For example, Mau²⁴ has studied the theory of energy analyzer operation and the modification of the electron distribution due to damped whistler waves, Andersen, et.al.^{25,26} has studied the ion distribution and wave-particle interaction in a Q-machine, and Guillemot, et.al.²⁷ reported the deformation of the electron distribution due to damped electrostatic waves. Design considerations for energy analyzers were reported by Simpson²⁸.

The energy analyzer used in our experiments has four electrodes as shown in Fig. 3-11. The entrance grid, shields the plasma from the electric fields within the analyzer and can be biased at the plasma potential ϕ_p assuming this does not disturb the operation of the plasma. Since this grid is electrically connected to the endplate of the experiment and ϕ_p is a function of radius it is impossible to bias this grid at the local

plasma potential without affecting the remaining regions of the plasma. In our case it is connected through a 50Ω resistor to the ECRH coupler assembly which serves as the reference electrode. Grid 2 is the discriminator grid and imposes an axial electric field to retard incoming charged particles. It was biased at negative voltages in our experiment since we wanted to analyze the axial energy of electrons. If ϕ_p is the local plasma potential and ϕ_d is the discriminator potential only electrons with energies, $\mathcal{E} > e(\phi_p - \phi_d)$ can surpass the potential barrier between the plasma and discriminator grid assuming ϕ_E , the potential on the entrance grid is small. It is experimentally determined that ϕ_E is sufficiently small ($\sim -10\text{mV}$) so that it can be neglected. Grid 3 is the repeller grid and is biased at a sufficiently large positive potential so as to repel all ions. The last element in the analyzer is the collector electrode which collects the electrons that have surpassed the retarding potential barrier of the discriminator grid.

The construction of the electrostatic energy analyzer is shown in Fig. 3-12. The entrance aperture of the analyzer is located at a radius of 3.81 cm and at an azimuthal position of $\theta = \pi/2$, i.e. in the region of maximum signals as indicated by the radial and azimuthal current probe measurements. The entrance aperture diameter of the analyzer is 1.11 cm. The wire mesh grids were constructed from tungsten screening and the copper collector electrode was covered with a layer of carbon to help eliminate secondary emission from the collector. Pertinent dimensions of the energy analyzer are indicated in Fig. 3-12.

An important figure of merit for the energy analyzer is the energy resolution which has a lower limit determined by the lens effect^{17,29}. The entrance aperture of the energy analyzer can be considered as a diverging electrostatic lens whose focal length is given by

$$f = \left(\frac{E_2 - E_1}{4\mathcal{E}_2} \right)^{-1} \quad (3.15)$$

where E_2 and E_1 are the electric fields in the plasma and in the analyzer respectively. The incoming particles have an energy $e\mathcal{E}_2$. The electrostatic lens is diverging since $E_2 < E_1$. A lower bound on the resolution can be estimated by assuming $E_2 = 0$ and $E_1 \neq 0$. The particle energy is

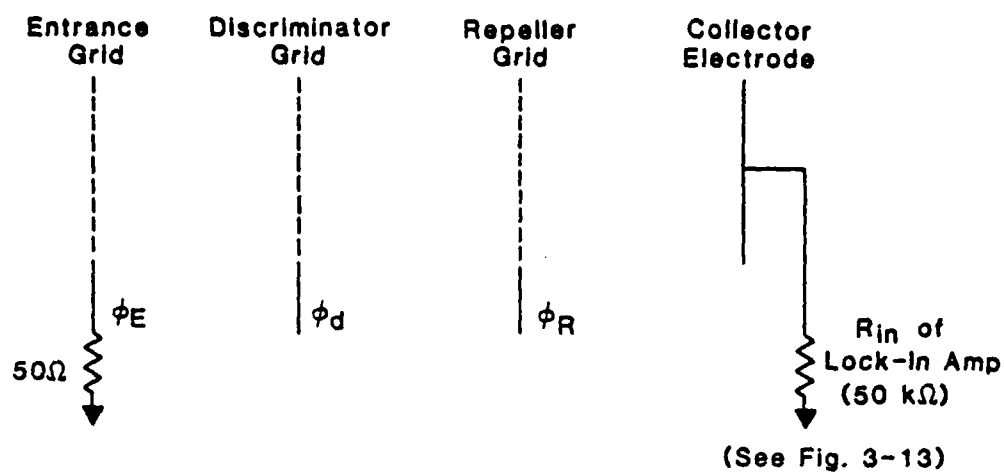


Fig. 3-11 Grid Configuration of Retarding Field Electrostatic Energy Analyzer

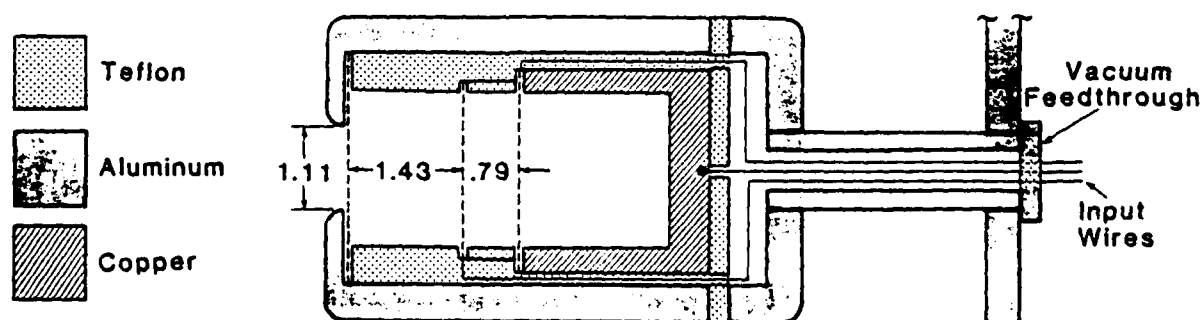


Fig. 3-12 Construction of Electrostatic Energy Analyzer
(Dimensions in Centimeters)

$\mathcal{E}_2 = E_1 h$ where h is the distance between the entrance grid aperture and the discriminator grid. Hence Eq. (3.15) reduces to

$$f = -4h \quad (3.15A)$$

The divergence angle^{17,29} is given by

$$\sin^2 \theta_d = \frac{(D/2)^2}{(D/2)^2 + f^2} \quad (3.16)$$

and using Eq. (3.15A) the maximum divergence angle is given by

$$\sin^2 \theta_{d,\max} = \frac{(D/2)^2}{(D/2)^2 + 16h^2} \quad (3.17)$$

where D is the diameter of the entrance aperture. It is now assumed that an incoming particle possesses both axial and transverse components of velocity, v_z and v_1 respectively. The magnetic field does not complicate the situation since both electron and ion gyro radii are much less than the diameter of the entrance aperture. The transverse energy and the axial energy of the particle is related by

$$\frac{\mathcal{E}_1}{\mathcal{E}_2} = \tan^2 \theta$$

where θ is the angle between the velocity vector and the z -axis. Since only axial momentum is sampled by the analyzer, the energy resolution is given by

$$\frac{\Delta \mathcal{E}}{\mathcal{E}} = \frac{v_1^2}{v^2} = \sin^2 \theta \quad (3.18)$$

Hence an estimate of the resolution of the energy analyzer is given by

$$\frac{\Delta \mathcal{E}}{\mathcal{E}} = \frac{1}{1 + (8h/D)^2} \quad (3.19)$$

For our analyzer, $D = 1.11$ cm and $h = 1.43$ cm which gives a resolution $\Delta \mathcal{E}/\mathcal{E} \approx 0.009$.

The energy analyzer is designed to sample electrons with a positive axial velocity component (directed away from the ECRH plasma source). The electrons possess an axial distribution function $f_e(v_z)$ and it is desired to find a relationship between the collector current I_c , the dis-

criminator potential ϕ_d , and the distribution function $f_e(v_z)$. The collector current is determined by the number of electrons that surpassed the potential barrier established by the discriminator grid. Hence,

$$I_c(\phi_d) = -A T e \int_{v_c}^{\infty} v_z f_e(v_z) dv_z \quad (3.20)$$

where v_z is the axial electron velocity associated with an energy $-e\phi_o = (1/2)m_e v_z^2$, A is the cross sectional area of the entrance aperture, T is the overall geometric transmission coefficient of the grids, and v_c is the cutoff velocity determined by the discriminator and plasma potentials.

$$v_z(\phi_o) = \left(\frac{-2e\phi_o}{m_e} \right)^{1/2} \quad (3.21)$$

$$dv_z = \left(\frac{-e}{2m_e\phi_o} \right)^{1/2} d\phi_o \quad (3.22)$$

Substituting Eqs. (3.21) and (3.22) into Eq. (3.20) yields

$$I_c(\phi_d) = -A T e \int_{\phi_p - \phi_d}^{-\infty} \left(\frac{-2e\phi_o}{m_e} \right)^{1/2} \left(\frac{-e}{2m_e\phi_o} \right)^{1/2} f_e(v_z(\phi_o)) d\phi_o$$

$$I_c(\phi_d) = \frac{-A T e^2}{m_e} \int_{\phi_p - \phi_d}^{-\infty} f_e(v_z(\phi_o)) d\phi_o \quad (3.23)$$

Differentiating yields,

$$\frac{dI_c}{d\phi_d} = \frac{-A T e^2}{m_e} f_e(v_z(\phi_p - \phi_d)) \quad (3.24)$$

Eq. (3.24) demonstrates that the distribution function can be obtained by differentiating the collector current with respect to the discriminator potential.

The differentiation of Eq. (3.24) is performed electronically as shown in Fig. 3-13^{17,27}. It was found experimentally that a repeller grid potential, $\phi_R = 100V$ was sufficient to repel all ions. The output of the collector electrode was connected through a shielded coaxial cable to the input of a Princeton Applied Research model JB-5 lock-in amplifier (input impedance of $50k\Omega$). The discriminator voltage was swept by the sawtooth output (0 - +150 V) from a Tektronix type 33 oscilloscope. A -150V power supply was kept in series with this sawtooth signal to maintain the discriminator at a negative potential since we are sampling the electron energies. Also a small amplitude, high frequency reference potential, ϕ_{ref} was applied to the discriminator grid through an isolation transformer. As can be seen in Fig. 3-13 the reference was derived from the internal reference of the lock-in amplifier.

$$\text{Reference Signal: } \phi_{ref}(t) = v_o \cos \omega_{ref} t$$

$$\text{DC + Sawtooth Signal: } \phi_s(t) = -V_o + V_o \cos \omega_{s,fund} t$$

$\omega_{s,fund}$ is the fundamental frequency component of the sawtooth signal. The total discriminator potential is given by

$$\phi_d = \phi_s(t) + \phi_{ref}(t)$$

Conditions were set on the applied signals such that

$$V_o \gg v_o, \omega_{ref} \gg \omega_{s,fund}$$

The time base on the oscilloscope was typically set at a sweep of 5 sec/cm and the reference frequency from the lock-in amplifier at 1 kHz. On this time scale the voltage sweep from the sawtooth generator is extremely slow compared to the time scale of the reference signal. The collector current is written as,

$$I_c(\phi_d) = I_c(\phi_s + \phi_{ref}(t)) \quad (3.25)$$

Since $V_o \gg v_o$, we expand $I_c(\phi_d)$ about ϕ_s retaining terms only to first order

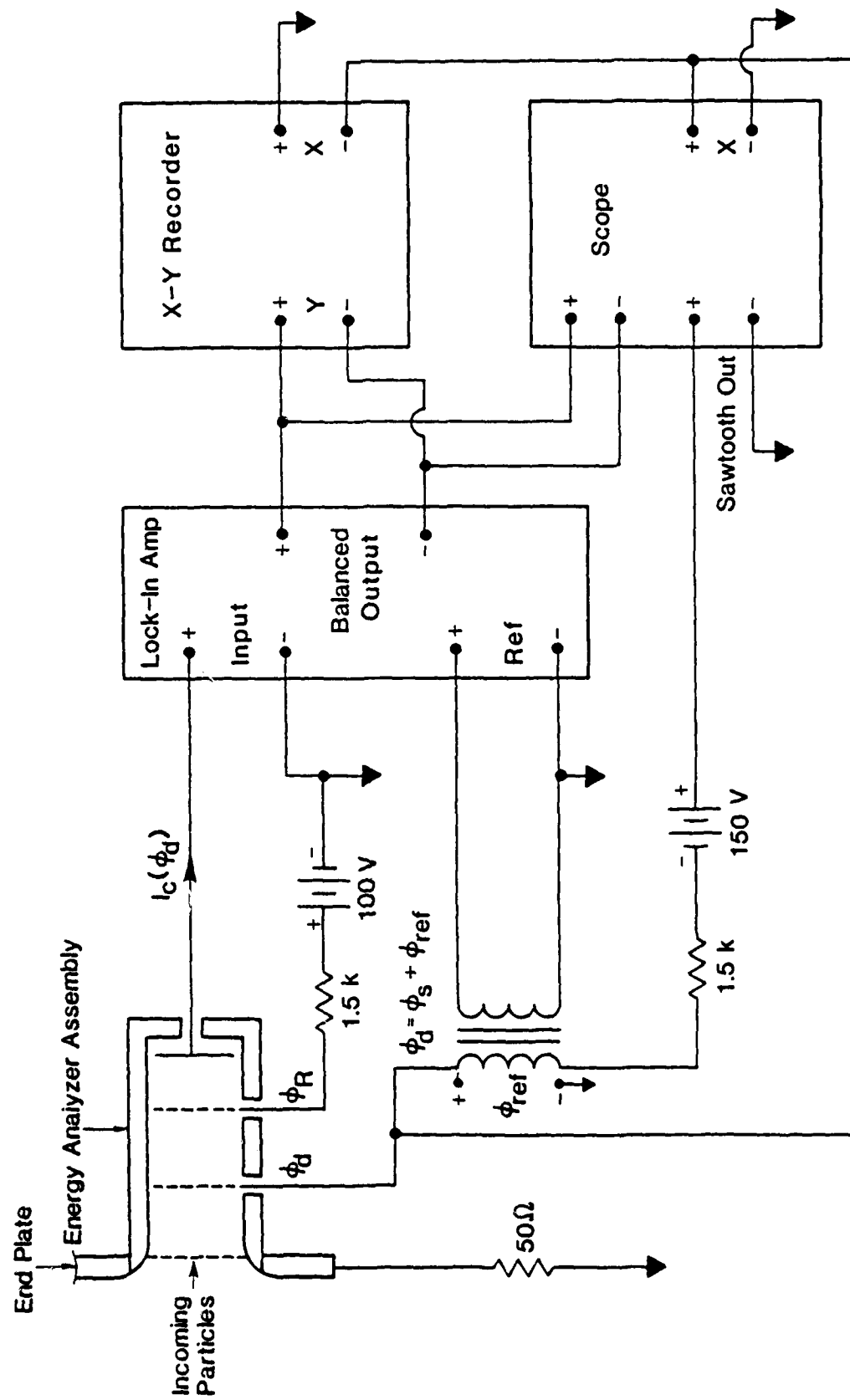


Fig. 3-13 Electronic System for Measuring Electron Distribution Function

$$I_c(\phi_d) = I_c(\phi_s) + \left. \frac{dI_c}{d\phi_d} \right|_{\phi_s} \phi_{ref}(t) + \dots \quad (3.26)$$

The collector signal is mixed with the reference signal in the lock-in amplifier and a dc component is produced due to the term

$$\left. \frac{dI_c}{d\phi_d} \right|_{\phi_s} \phi_{ref}^2(t)$$

This dc output is filtered through a low pass filter with a time constant of 1 sec (fast compared with sweep speed) and is applied to the y-axis of an x-y recorder. The x-axis is driven by the sawtooth sweep signal ϕ_s . Using this technique the energy distribution function of electrons can be displayed directly on the x-y recorder. It should be noted that the reference signal amplitude V_o , must satisfy the condition that $V_o \ll V_o$; it should not be so small as to sample the small scale fluctuations in the distribution function. The entire electronic system is isolated from ground through an isolation transformer which supplies all ac power to the electronic equipment. The ECRH coupler serves as the common reference electrode.

The electron velocity distribution is normalized as

$$\langle n \rangle_{total} = \int_{-\infty}^{\infty} f_e(v_z) dv_z \quad (3.27)$$

Some information regarding the dynamics of the electrons can be determined by analyzing the moments of the electron distribution. Care must be taken in the interpretation of the energy analyzer data since the moments as determined from the experimental distribution are not the same as the moments obtained from the real distribution since the energy analyzer does not sample electrons with negative velocities. A typical experimental electron distribution is shown in Fig. 3-14 where ϕ is the absolute value of the applied dc discriminator potential ϕ_s and ϕ_p is the negative of the plasma potential. The moments of the experimental distribution $g(\phi)$ are given in Eqs. (3.28) to (3.33) ^{17,29}.

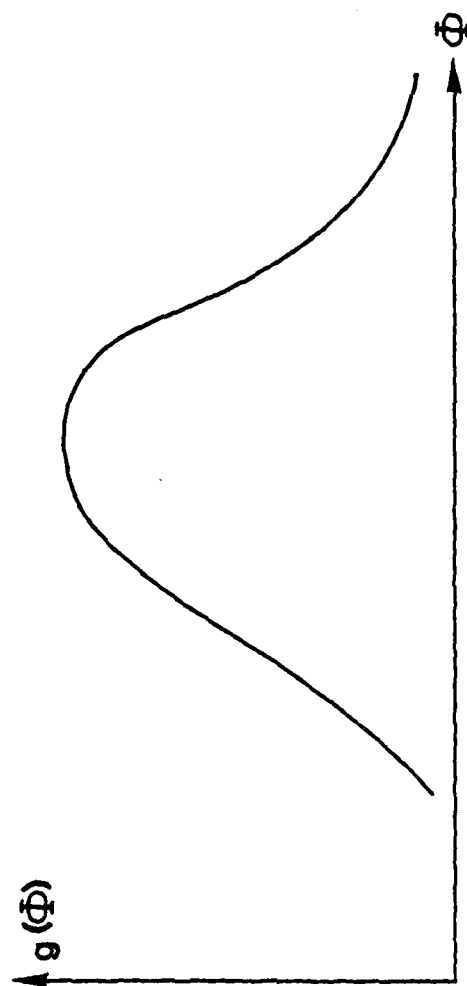


Fig. 3-14 Typical Experimental Electron Energy Distribution

$$\langle n \rangle = \left(\frac{-e}{2m_e} \right)^{1/2} \int_{\phi_p}^{\infty} \phi^{-1/2} g(\phi) d\phi \quad (3.28)$$

$$\langle nv_z \rangle = \frac{-e}{m_e} \int_{\phi_p}^{\infty} g(\phi) d\phi \quad (3.29)$$

$$\langle \frac{1}{2} m_e n v_z^2 \rangle = -e \left(\frac{-e}{2m_e} \right)^{1/2} \int_{\phi_p}^{\infty} \phi^{1/2} g(\phi) d\phi \quad (3.30)$$

If $\langle n \rangle$ is uncorrelated with $\langle nv_z \rangle$ and $\langle \frac{1}{2} m_e n v_z^2 \rangle$ the following moments can also be written

$$\langle v_z \rangle = \frac{\langle nv_z \rangle}{\langle n \rangle} = \left(\frac{-2e}{m_e} \right)^{1/2} \frac{\int_{\phi_p}^{\infty} g(\phi) d\phi}{\int_{\phi_p}^{\infty} \phi^{-1/2} g(\phi) d\phi} \quad (3.31)$$

$$\langle \frac{1}{2} m_e v_z^2 \rangle = \frac{\langle \frac{1}{2} m_e n v_z^2 \rangle}{\langle n \rangle} = -e \frac{\int_{\phi_p}^{\infty} \phi^{1/2} g(\phi) d\phi}{\int_{\phi_p}^{\infty} \phi^{-1/2} g(\phi) d\phi} \quad (3.32)$$

and the mean random energy $\langle \mathcal{E}_z \rangle$ can be written

$$\begin{aligned}
\langle \mathcal{E}_z \rangle &= \left\langle \frac{1}{2} m_e v_z^2 \right\rangle - \frac{1}{2} m_e \langle v_z \rangle^2 \\
&= -e \left\{ \frac{\int_{\phi_p}^{\infty} \phi^{1/2} g(\phi) d\phi}{\int_{\phi_p}^{\infty} \phi^{-1/2} g(\phi) d\phi} - \left[\frac{\int_{\phi_p}^{\infty} g(\phi) d\phi}{\int_{\phi_p}^{\infty} \phi^{-1/2} g(\phi) d\phi} \right]^2 \right\} \quad (3.33)
\end{aligned}$$

Eqs. (3.28) to (3.33) are evaluated numerically for the experimental data.

It should be noted that if there is a drift velocity associated with the electron distribution and the plasma potential is not known a priori it may be difficult to interpret the experimental data since a change in plasma potential also will shift the experimental distribution function as well as a shift in energy of the real distribution function. However, the combination of energy analyzer data, current probe measurements, and electrostatic probe measurements will help in the understanding of the electron dynamics as will be discussed in chapter 4.

Chapter 4

EXPERIMENTAL RESULTS4.1 Introduction

To understand the wave-plasma interaction, it is important to be familiar with the operating characteristics of the plasma device, the unperturbed nature of the plasma, and the free space characteristics of the slow wave structure. By doing this, it is possible to obtain a better understanding of how the rf electrostatic waves interact with the plasma and modify it. In this chapter a discussion of the background plasma and the rf experiments will be presented, and in Chapter 5 an interpretation of these results along with a simple theoretical model will be presented.

All plasma experiments were performed using Argon at an operating pressure of 2×10^{-4} Torr and the axial magnetic field profile illustrated in Fig. 2-4.

4.2 Background Plasma

The incident ECRH microwave power determines the initial state of the plasma before low frequency electrostatic waves are excited by the slow wave structure. Electrons absorb microwave energy through ECRH and the hot electron fluid expands out of the coupler region into the drift region with a relatively uniform axial magnetic field. The cold ions then acquire an axial drift out of the coupler region to maintain quasineutrality. As the microwave power is increased, the ionization, and hence the local electron density increases until the density reaches a level such that the local electron plasma frequency is equal to the incident microwave frequency. At this point additional microwave energy is shielded from the plasma and is reflected from the microwave coupler and is dissipated in the isolator. Hence, the maximum achievable electron density is determined from this criterion. The electron plasma frequency is determined from the electron density by Eq. (4.1)

$$\omega_{pe}^2 = \frac{e^2 n_e}{m_e \epsilon_0} \quad (4.1)$$

For the microwave frequency of 2.45 GHz used in the experiment the upper limit on electron density is $7.43 \times 10^{10} \text{ cm}^{-3}$. Fig. 4-1 shows a graph of the reflected and transmitted microwave power for the Lisitano coil versus incident microwave power. It can be seen in Fig. 4-1 that approximately 25 watts is required to initiate a discharge. It should also be noted that the reflection coefficient is unity if the plasma is not present due to the short circuit termination on the Lisitano coil. For most experiments the system is operated at an incident microwave power of 490 watts and a transmitted power of 121 watts.

Fig. 4-2 defines the axial reference position, $z = 0$, in reference to the slow wave structure. It should be noted that the z -scale used here is not the same as the z -scale used in some of the figures of chapter 2. This axial reference is important to define since the plasma is inhomogeneous in both the axial and the radial directions and both inhomogeneities affect the coupling of the rf energy from the slow wave structure to the plasma. Fig. 4-3 shows the radial profile of the electron density at an axial position of $z = -3.81 \text{ cm}$. Figs. 4-4 and 4-5 are semi-log plots of the electron density and electron temperature versus r^2 at $z = -3.81 \text{ cm}$. A radial profile of the relative magnitude of the ion saturation current is shown in Fig. 4-6. Figs. 4-3 and 4-6 indicate that the radial profile of ion saturation current is approximately the same as the radial profile of electron density indicating that the electron temperature varies more slowly across the plasma than does the electron density. This result is supported by Figs. 4-4 and 4-5 which indicates the radial scale length of electron temperature variation is longer than the radial scale length of the electron density variation. Fig. 4-7 shows the magnitude of the ion saturation current versus the radial probe angle α with the axial position z as a parameter. From Fig. 4-7 and various probe characteristics at different axial positions in the plasma, the axial profile of electron density and electron

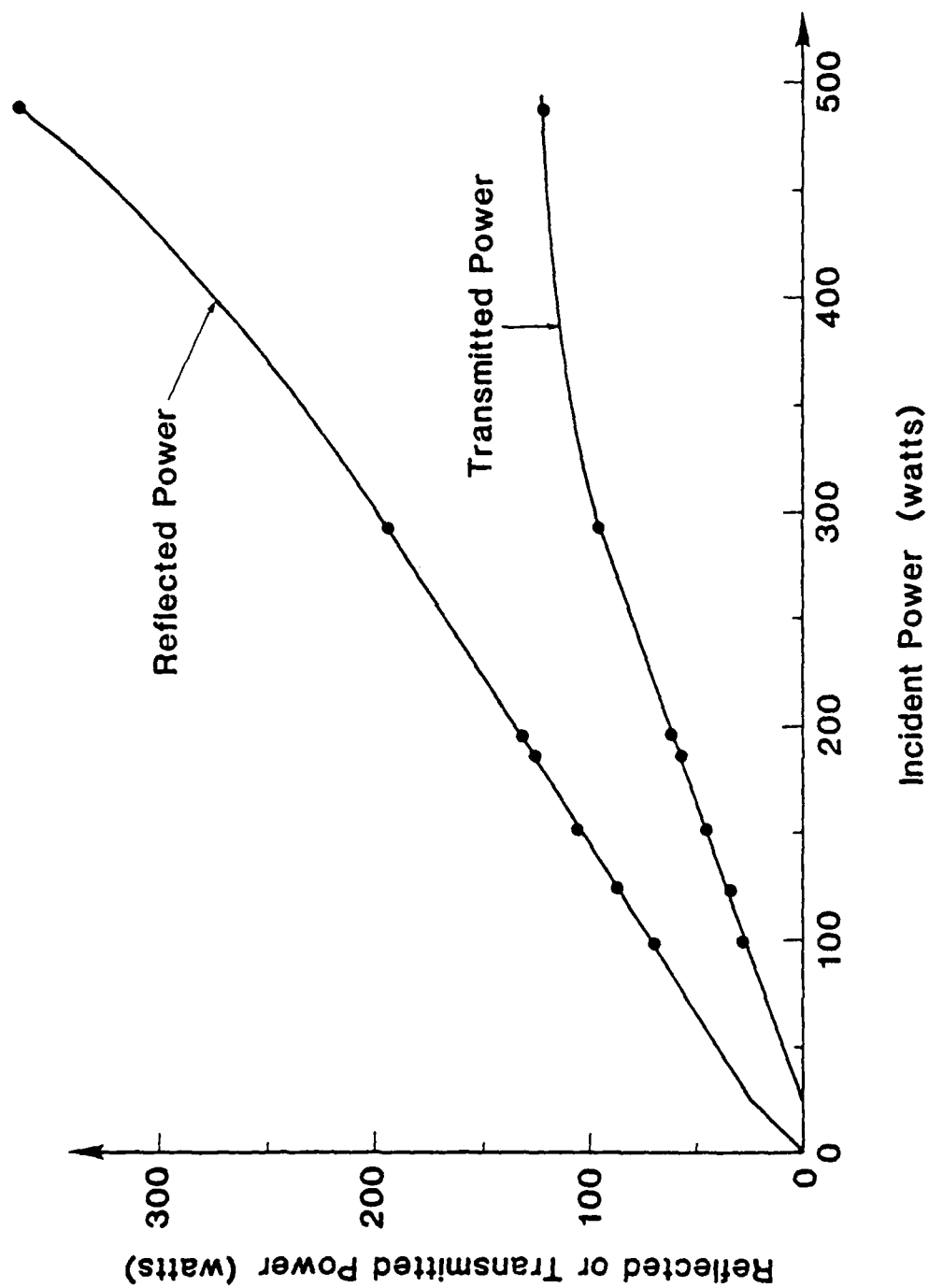


Fig. 4-1 Reflected and Transmitted Microwave Power vs. Incident Power for Lisitano Coil

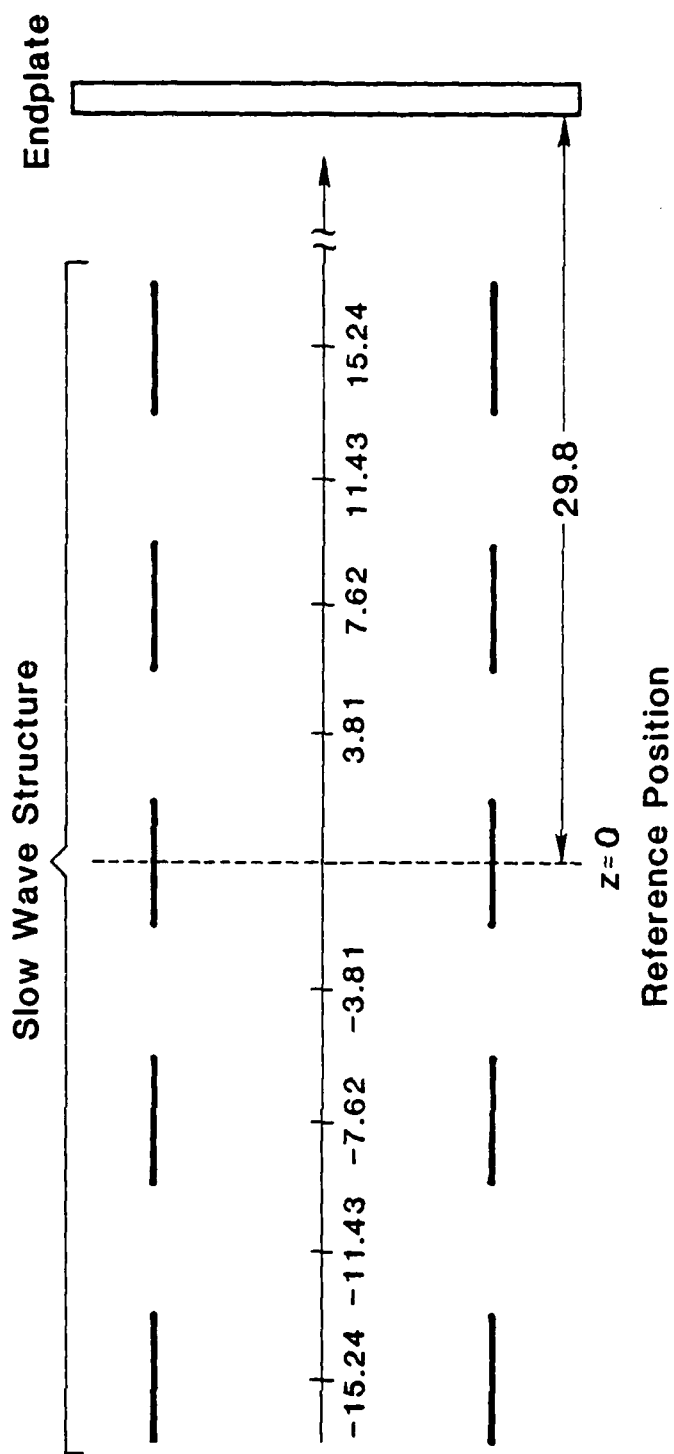


Fig. 4-2 Axial Reference Position for Experimental Measurements
(Dimensions in Centimeters)

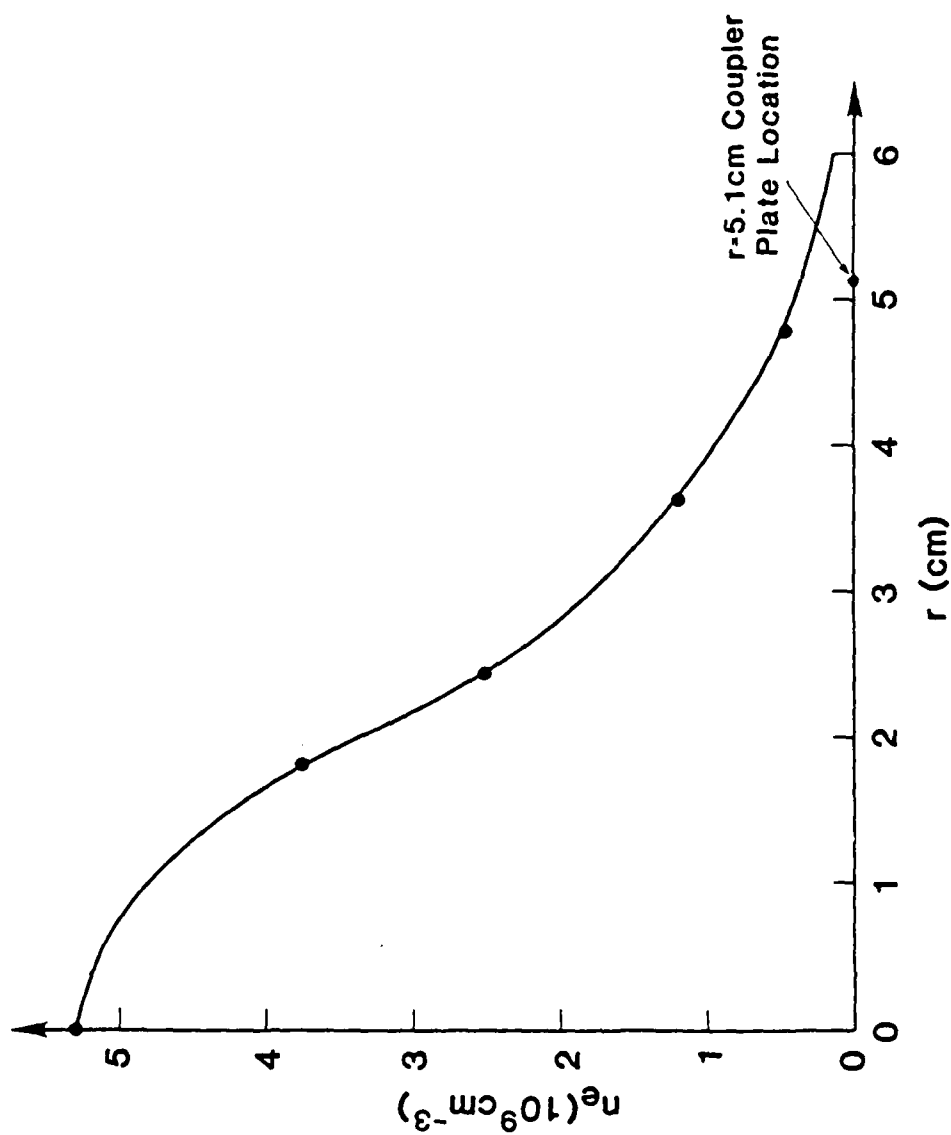


Fig. 4-3 Radial Profile of Electron Density at $z = -3.81$ cm

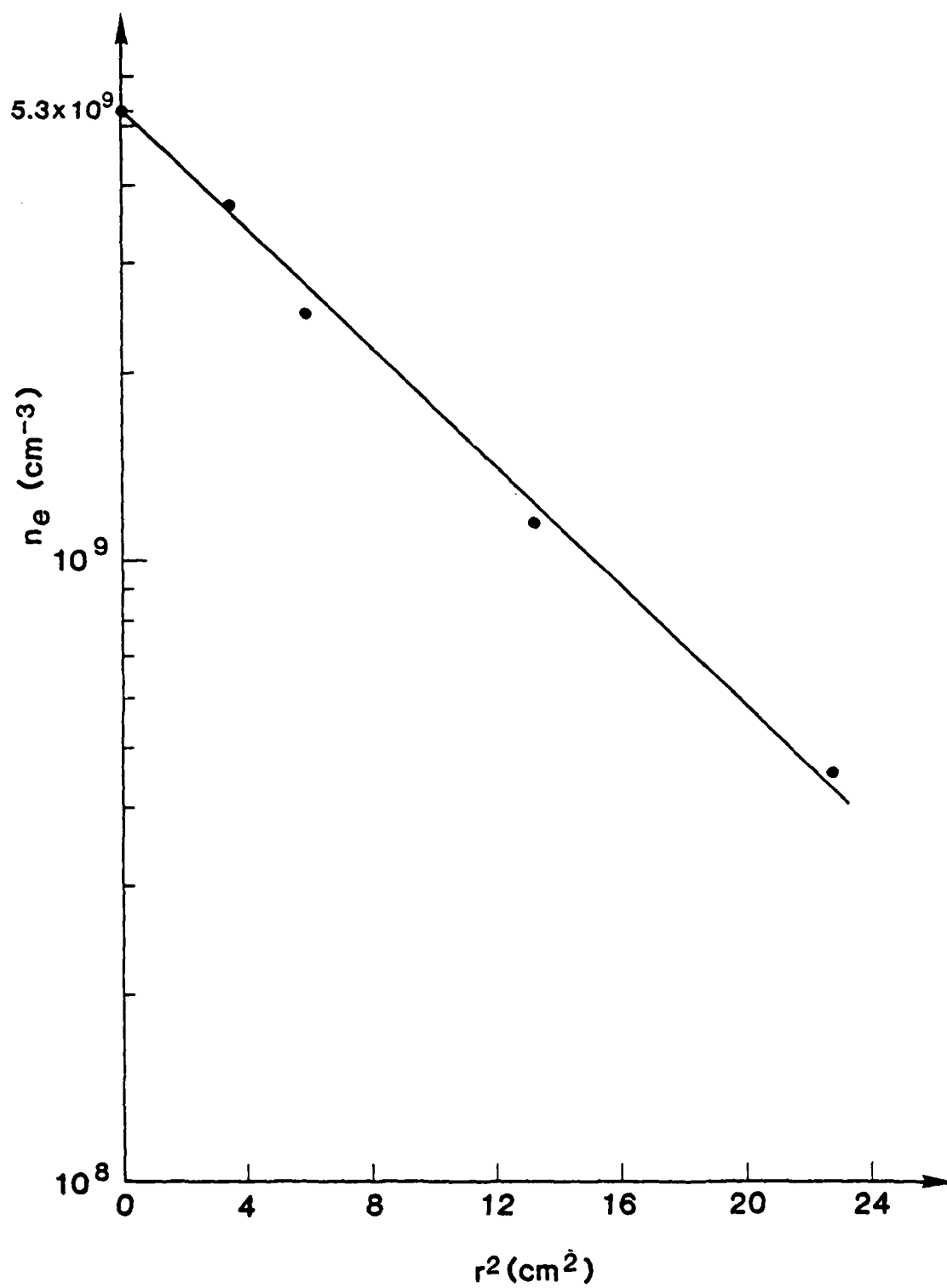


Fig. 4-4 Electron Density vs. r^2 at $z = -3.81 \text{ cm}$

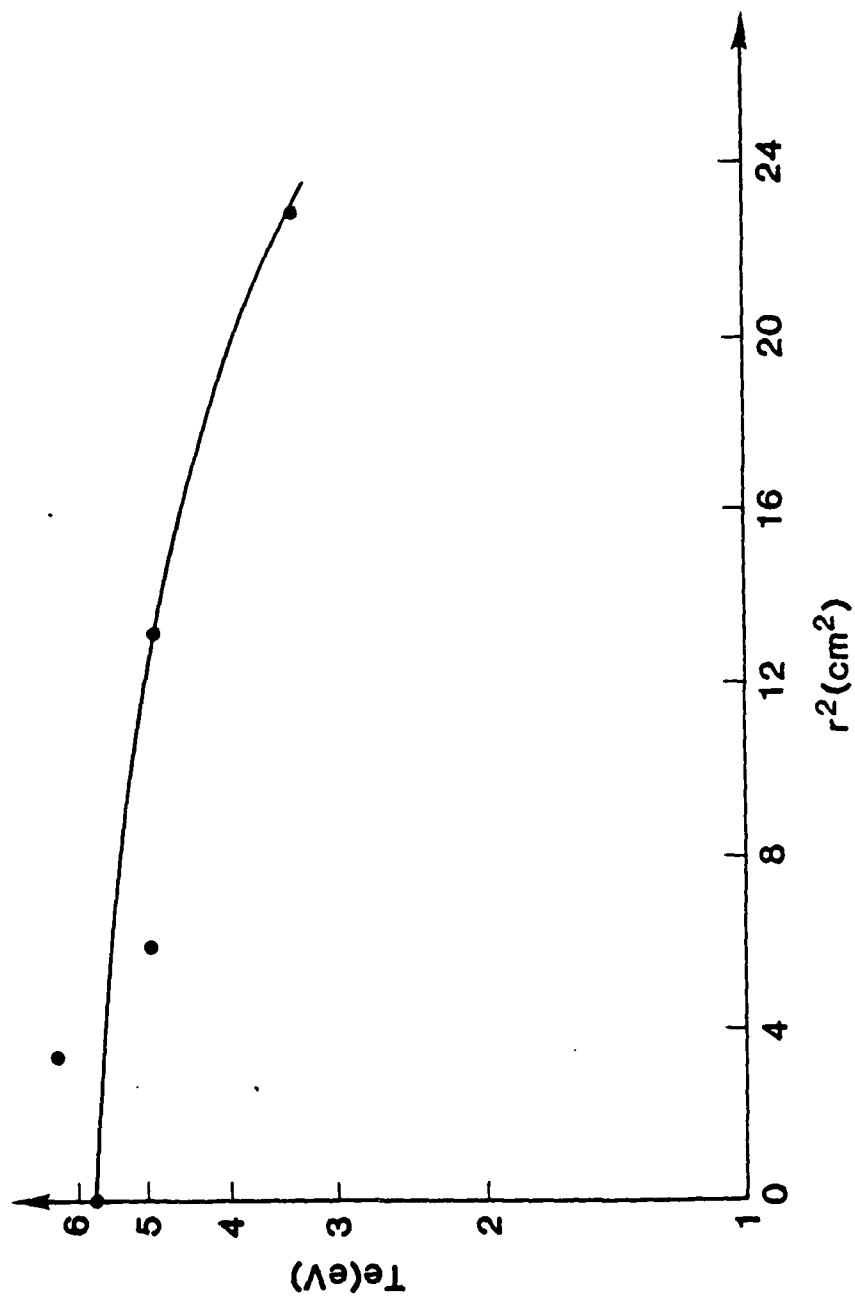


Fig. 4-5 Electron Temperature vs. r^2 at $z = -3.81 \text{ cm}$

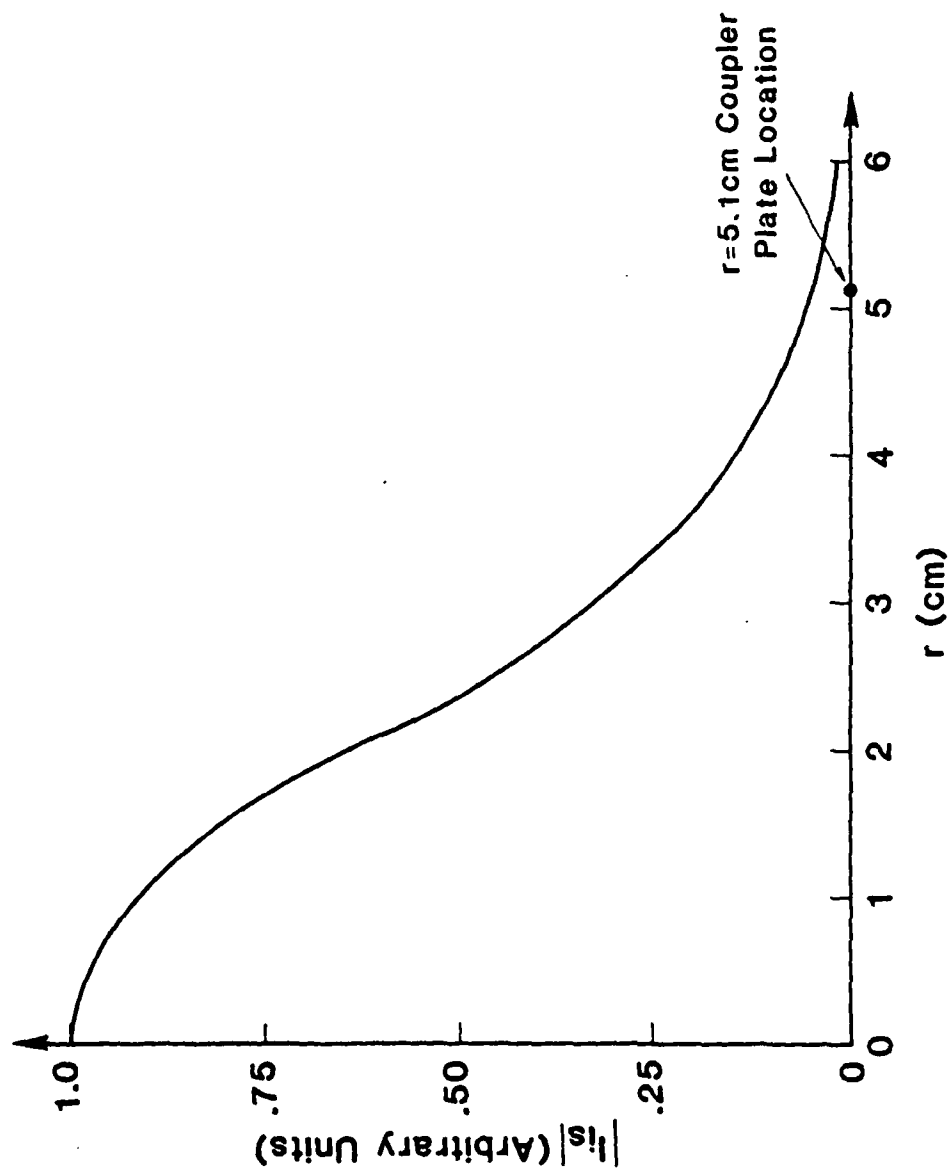


Fig. 4-6 Radial Profile of Relative Magnitude of Ion Saturation Current

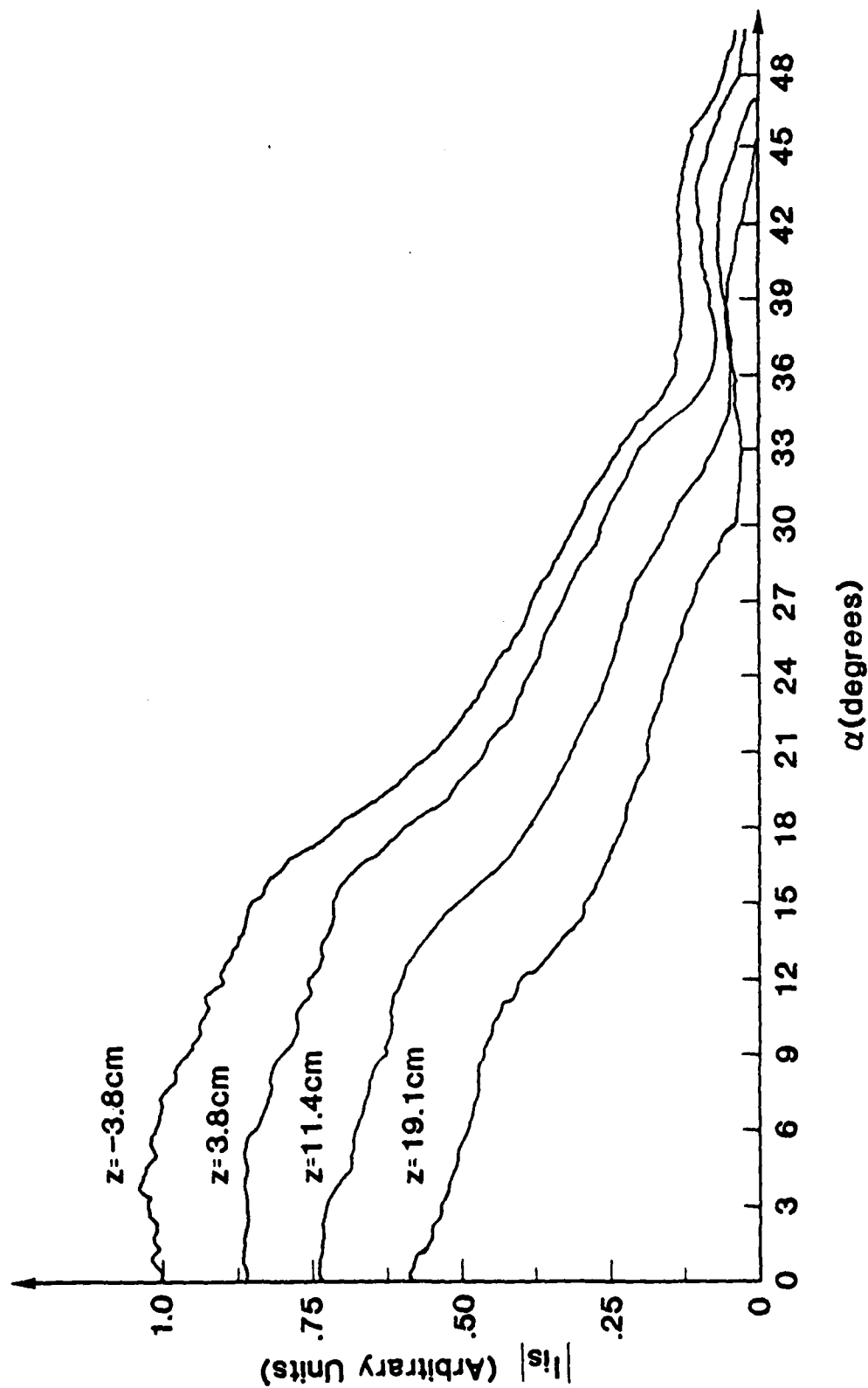


Fig. 4-7 Magnitude of Ion Saturation Current vs. α with z as a Parameter

temperature can be determined. Figs. 4-8 and 4-9 show the axial profiles of electron density and electron temperature at $r=0$ respectively. The Langmuir probe measurements also indicate that the background plasma is azimuthally symmetric. Fig. 4-10 shows the magnitude of the ion saturation current versus the radial probe angle α with the transmitted ECRH power as a parameter. The effect of the reduction of ECRH power is to reduce the ion saturation current and hence the electron density profile as well as the electron temperature profile. It is found experimentally, however, that the electron temperature decreases at a slower rate than does the electron density with ECRH power and hence the curves in Fig. 4-10 are indicative of the electron density profile in the plasma. Based on these Langmuir probe results, it is possible to construct a physical model of the background plasma electron density.

The spatial variation of electron density is modeled by

$$n_e(r,z) = n_o e^{-r^2/R^2} \left(1 - \frac{z}{L}\right) \quad (4.2)$$

where R and L are the radial and axial scale lengths determined from Figs. 4-4 and 4-8 respectively. n_o is the electron density at the position $(r,z) = (0,0)$. These three parameters are given by:

$$n_o = 4.82 \times 10^{15} \text{ m}^{-3}$$

$$R = 0.03\text{m}$$

$$L = 0.39\text{m}$$

Radial and azimuthal current probes were used to measure the localized current density in the plasma. The electron current density J_{ez} versus the radial probe angle α is shown in Fig. 4-11 and the experimental results also indicated that the localized current density was azimuthally symmetric as determined from the azimuthal current probe. The total current drawn from the endplate of the device is approximately -2 mA and a numerical integration of J_{ez} versus α yields approximately -1.8 mA comparing favorably with the measured value.

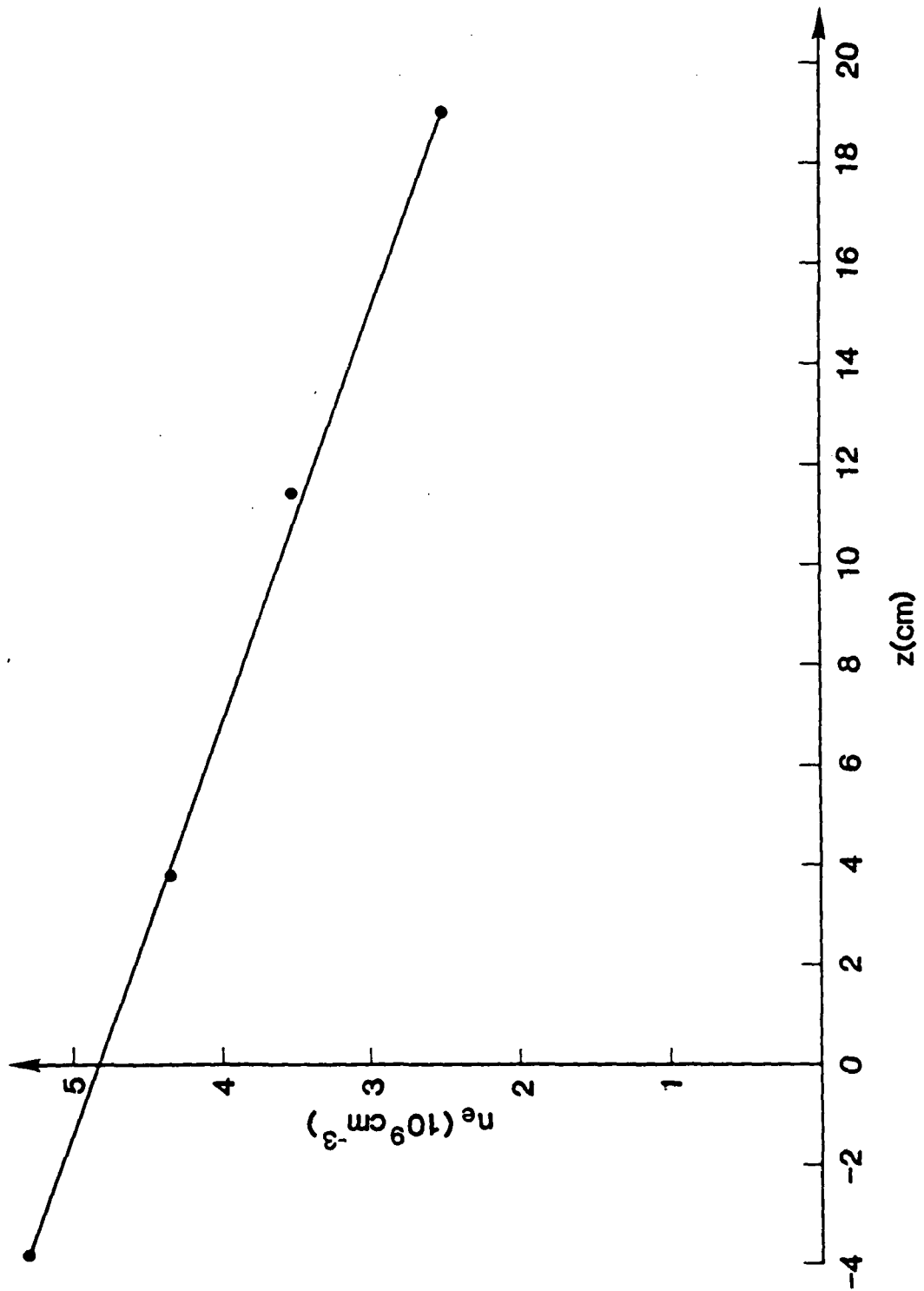


Fig. 4-8 Axial Profile of Electron Density at $r=0$

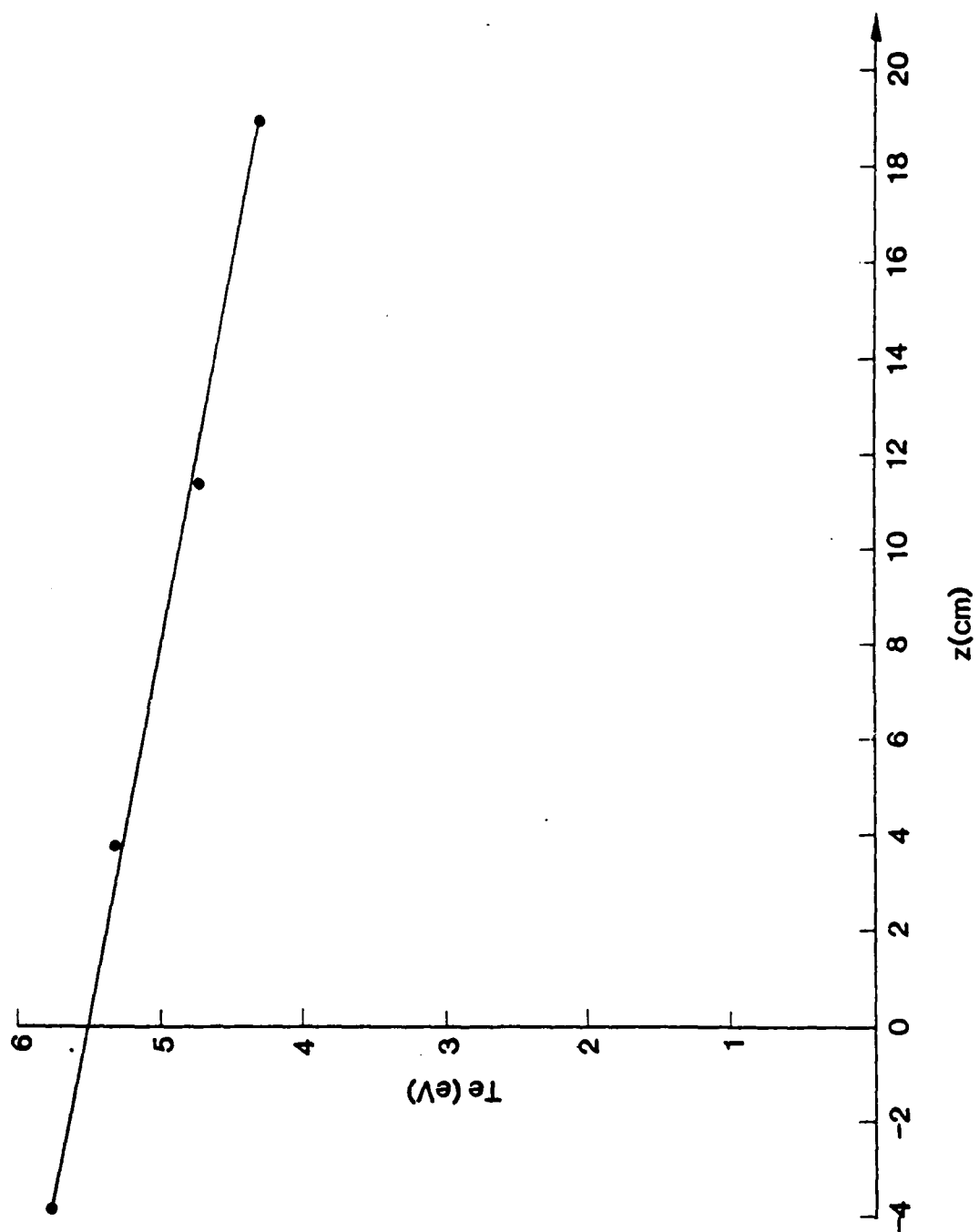


Fig. 4-9 Axial Profile of Electron Temperature at $r = 0$

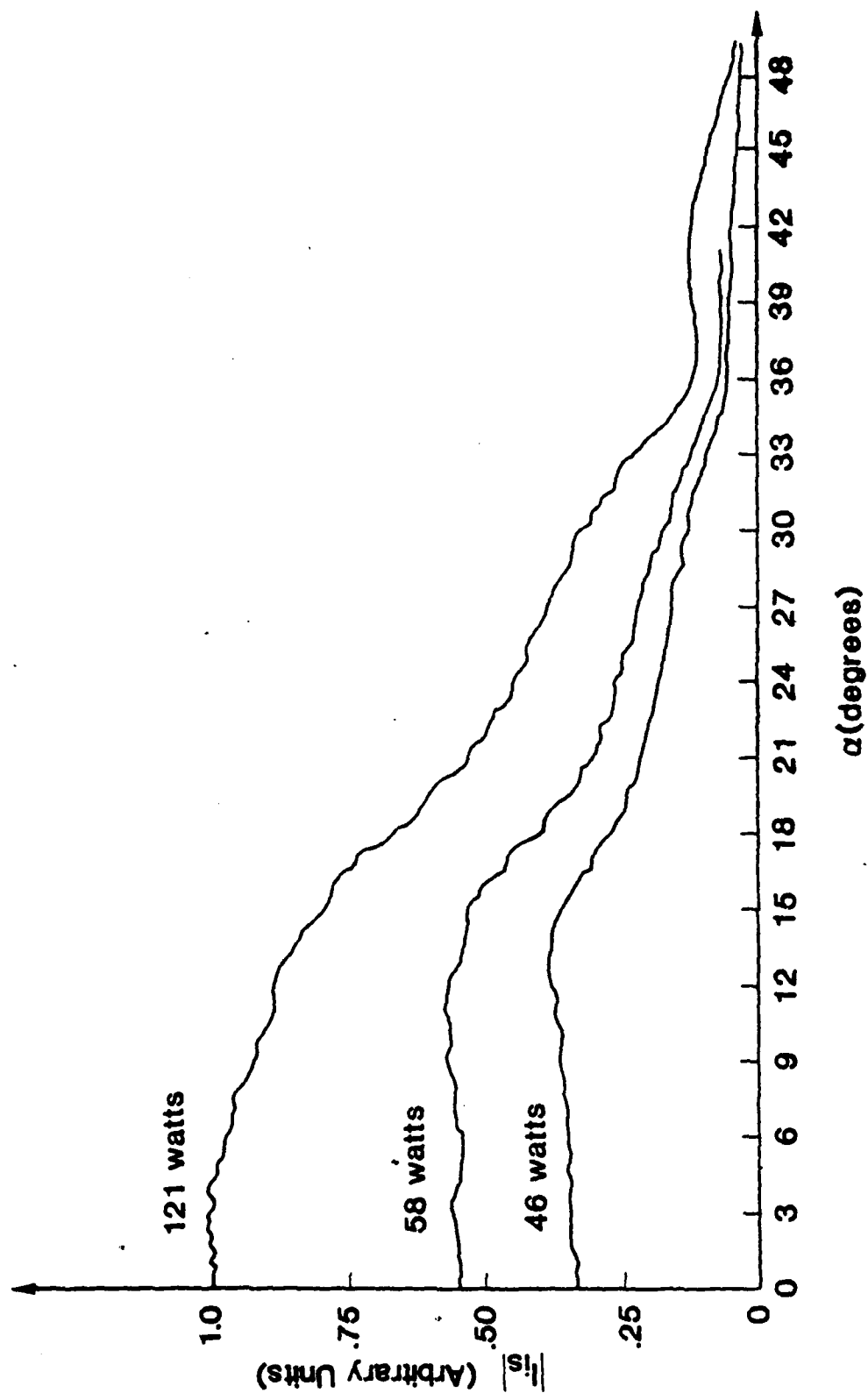


Fig. 4-10 Magnitude of Ion Saturation Current vs. α with ECRH Power as a Parameter

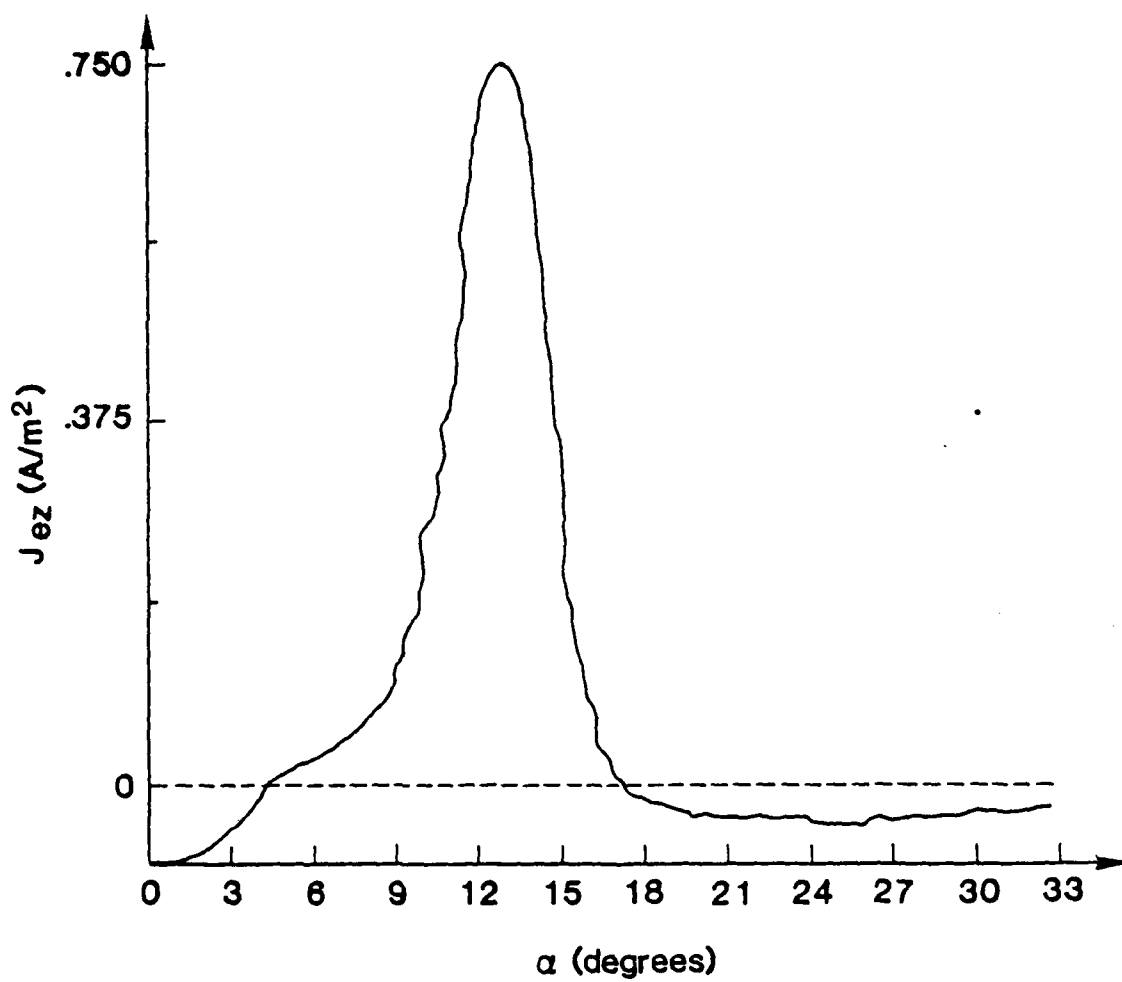


Fig. 4-11 Background Axial Electron Current Density vs. α

The electrostatic energy analyzer is located at a radial position of 3.81 cm and an azimuthal position of $\theta = \frac{\pi}{2}$ as discussed in section 3.5. The endplate of the experiment and hence the entrance aperture of the energy analyzer is located at an axial position of $z = 29.8$ cm ($z = 0$, defined in Fig. 4-2). The axial electron energy distribution is shown in Figs. 4-12 and 4-13. From Fig. 4-13 the axial electron temperature is determined to be 4.31 eV which compares favorably with the Langmuir probe results. The maximum value of the electron energy distribution can be normalized by using the measured electron density as determined by the Langmuir probe and a numerical integration of Eq. (3.28).

4.3 Typical Plasma Parameters

Table 4.1 is a summary of typical plasma parameters at $(r,z) = (0,0)$. Coulomb collision frequencies are determined from Spitzer's formulas

$$\nu_{ee} = \frac{e^4 n_e \ln \Lambda}{16\pi^{1/2} \epsilon_0^2 m_e^{1/2} (k_B T_e)^{3/2}} \quad (4.3)$$

$$\nu_{ei} = \frac{\nu_{ee}}{2\sqrt{2}} \quad (4.4)$$

$$\nu_{ie} = \left(\frac{m_e}{m_i}\right) \nu_{ei} \quad (4.5)$$

$$\nu_{ii} = \frac{e^4 n_i \ln \Lambda}{16\pi^{1/2} \epsilon_0^2 m_i^{1/2} (k_B T_i)^{3/2}} \quad (4.6)$$

where

$$\Lambda = \frac{12\pi(\epsilon_0 k_B T_e / e^2)^{3/2}}{n_e^{1/2}} \quad (4.7)$$

For a neutral pressure of 2×10^{-4} Torr the neutral density is $6.2 \times 10^{18} \text{ m}^{-3}$. The collision cross section for an electron-neutral Argon collision for an electron temperature at $(r,z) = (0,0)$ of 5.5 eV

is $9 \times 10^{-20} \text{ m}^2$. The electron thermal speed at this temperature is approximately 10^6 m/s . The electron-neutral collision frequency is given by

$$\nu_{en} = n_n \sigma_{ens} v_{te} \quad (4.8)$$

Similarly the ion-neutral collision frequency is given by

$$\nu_{in} = n_n \sigma_{ins} v_{ti} \quad (4.9)$$

where $\sigma_{ins} \sim 4 \times 10^{-19} \text{ m}^2$.

Additional interaction cross sections are given below¹⁷

- Ionization of Argon atoms by an electron:

$$\sigma_{eni} \sim 10^{-21} \text{ m}^2$$

- Excitation of 2P_s levels of Argon atoms by an electron:

$$\sigma_{enx} \sim 10^{-21} \text{ m}^2$$

- Charge exchange collisions between Argon atoms and an ion:

$$\sigma_{inch} \sim 4 \times 10^{-19} \text{ m}^2$$

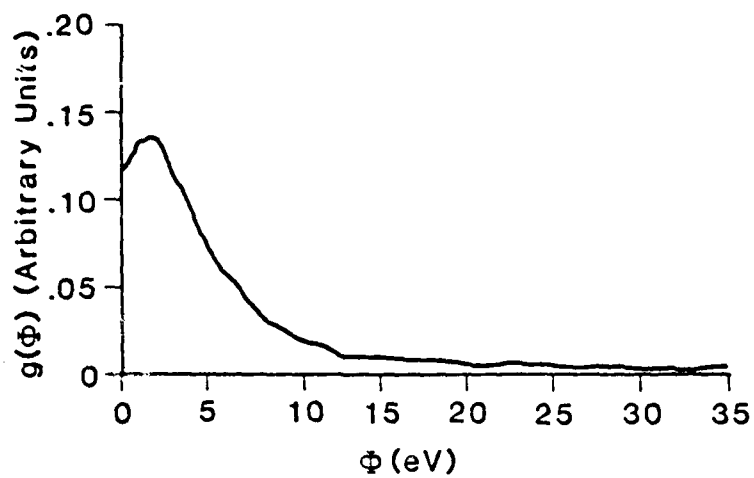


Fig. 4-12 Background Electron Energy Distribution at $(r, \theta) = (3.81 \text{ cm}, \pi/2)$

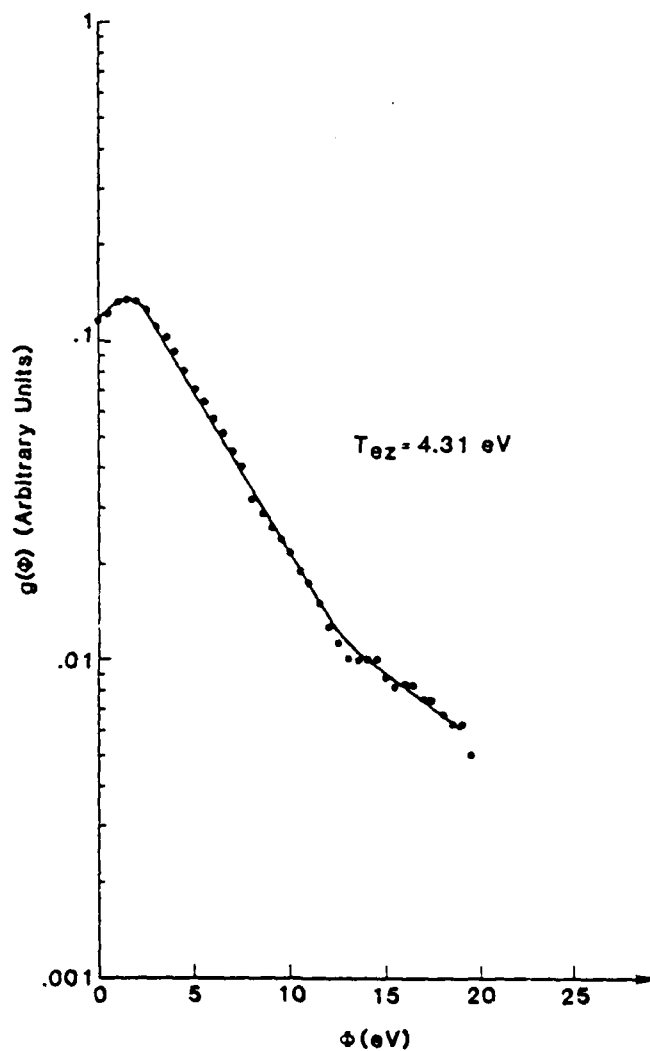


Fig. 4-13 Background Electron Energy Distribution from Fig. 4-12

Table 4-1 Typical Background Plasma Parameters at $(r,z) = (0,0)$

Quantity	Symbol	Value
Mass of Argon Ion	m_i	$6.63 \times 10^{-26} \text{ kg}$
Magnetic Field	B_0	850 Gauss
Neutral Pressure	p_n	$2 \times 10^{-4} \text{ Torr}$
Neutral Density	n_n	$6.2 \times 10^{18} \text{ m}^{-3}$
Electron, Ion Density	$n_{e,i}$	$4.82 \times 10^{15} \text{ m}^{-3}$
Radian Electron Plasma Frequency	ω_{pe}	$3.92 \times 10^9 \text{ rad/s}$
Electron Plasma Frequency	f_{pe}	624 MHz
Radian Ion Plasma Frequency	ω_{pi}	$1.45 \times 10^7 \text{ rad/s}$
Ion Plasma Frequency	f_{pi}	2.3 MHz
Radian Electron Cyclotron Frequency	Ω_e	$1.50 \times 10^{10} \text{ rad/s}$
Electron Cyclotron Frequency	f_e	2.39 GHz
Radian Ion Cyclotron Frequency	Ω_i	$2.05 \times 10^5 \text{ rad/s}$
Ion Cyclotron Frequency	f_i	32.6 kHz
Electron Temperature	$k_B T_e / e$	5.5 eV
Ion Temperature	$k_B T_i / e$	~ .5 eV
Electron Thermal Speed	v_{te}	10^6 m/s
Ion Thermal Speed	v_{ti}	$1.1 \times 10^3 \text{ m/s}$
Radial Density Profile Scale Length	R	.03 m
Axial Density Profile Scale Length	L	.39 m
Debye Length	λ_d	$1.78 \times 10^{-4} \text{ m}$
Debye Wave Number	k_d	$35.2 \times 10^3 \text{ m}^{-1}$
Electron Gyro Radius	ρ_e	$6.67 \times 10^{-5} \text{ m}$
Ion Gyro Radius	ρ_i	$5.37 \times 10^{-3} \text{ m}$
Electron-Electron Collision Frequency	ν_{ee}	27 kHz
Electron-Ion Collision Frequency	ν_{ei}	9.53 kHz
Ion-Electron Collision Frequency	ν_{ie}	.13 Hz
Ion-Ion Collision Frequency	ν_{ii}	3.64 kHz
Electron-Neutral Scattering Rate	ν_{ens}	558 kHz
Electron-Neutral Ionization Rate	ν_{eni}	6.2 kHz
Electron-Neutral Excitation Rate	ν_{enx}	6.2 kHz
Ion-Neutral Scattering Rate	ν_{ins}	2.8 kHz
Ion-Neutral Charge Exchange Rate	ν_{inch}	2.8 kHz
Radian Signal Frequency	ω	$2.04 \times 10^7 \text{ rad/s}$
Signal Frequency	f	3.25 MHz

4.4 Free Space Characteristics of the Slow Wave Structure

The physical construction of the slow wave structure was described in section 2.6. In this section the rf potential associated with the slow wave structure in free space will be described. The fundamental wave number associated with the slow wave structure, k_{zo} is determined by Eq.4.10

$$k_{zo} = \frac{\Delta\psi}{\Delta z} \quad (4.10)$$

where $\Delta\psi$ is the phase delay per section, and Δz is the distance between adjacent sections of the slow wave structure. For the experiments described here $|\Delta\psi| = \frac{\pi}{2}$ and $\Delta z = 7.6$ cm yielding $|k_{zo}| = .21 \text{ cm}^{-1}$. Fig.4-14 shows the axial phase delay as measured by the rf probe (see Section 3.4) for both $e^{ik_{zo}z}$ and $e^{-ik_{zo}z}$ excitations at a radial position located a small distance away from the coupler plates. At a radial position corresponding to the coupler plates it would be found that over the length of the coupler plate there would be no phase change and hence the phase change along the axis would not be as smooth. This is due to the high k_z content in the spatial Fourier transform of the slow wave structure.

Fig. 4-15 shows the relative magnitude of the rf potential versus the radial probe angle α at various axial locations for an rf power of 100 watts in the delay line corresponding to the coupler plates at $\theta = \frac{\pi}{2}$. Since the slow wave structure is a balanced system, the magnitude of the rf potential is an even function of α . The radial wave number is imaginary since the axial wavelength is much less than the free space wavelength; i.e. $\frac{\omega}{c} \ll k_{zo}$ and the signal is evanescent in the radial direction. Fig. 4-16 shows the α -profile of phase and it is seen that the phase is constant except for a nearly discontinuous 180° change in phase at $\alpha = 0$. The constant phase for $\alpha \neq 0$ is indicative of the evanescence and the 180° phase change is due to the fact that the structure is balanced.

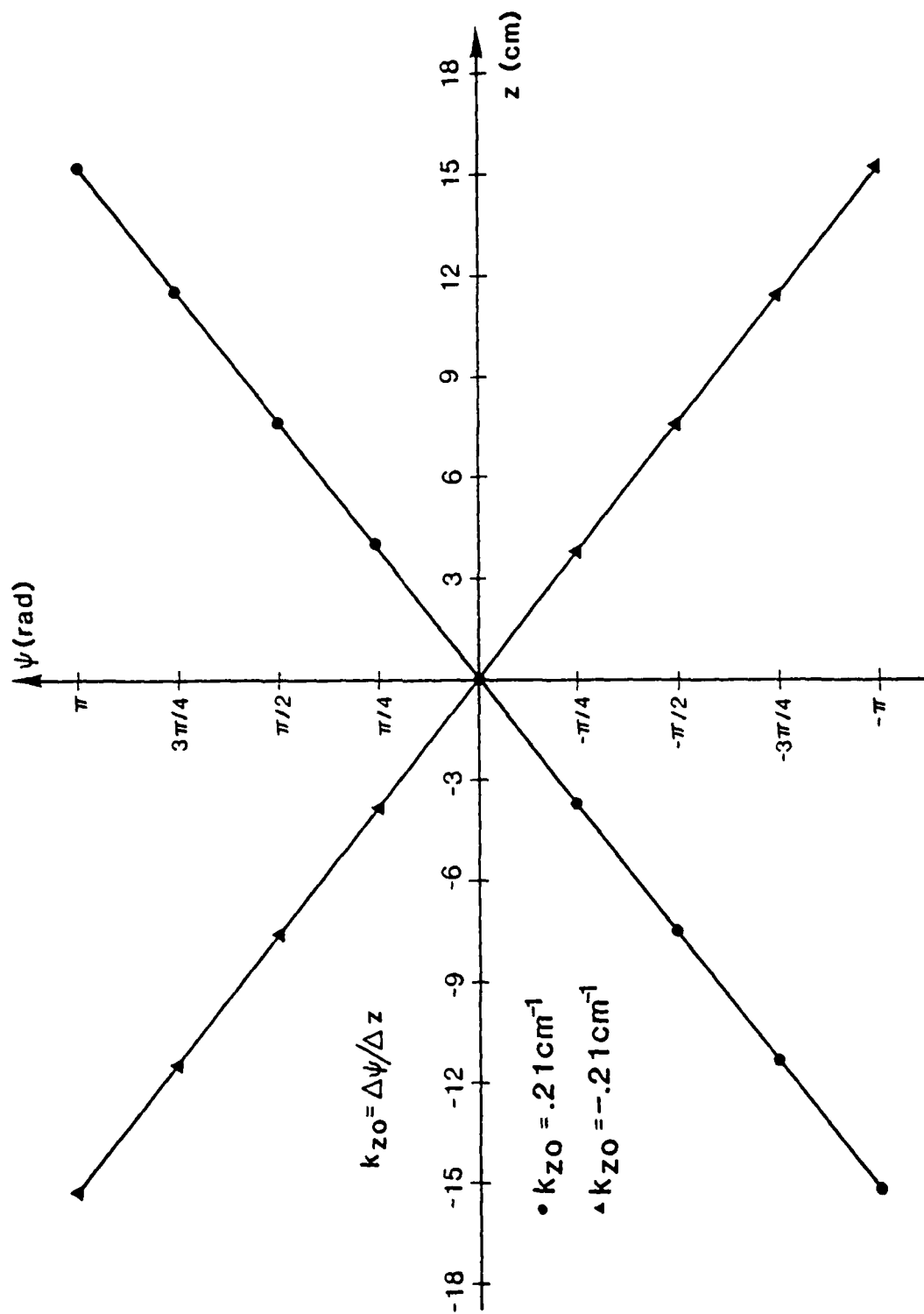


Fig. 4-14 Axial Phase Shift of Slow Wave Structure in Free Space

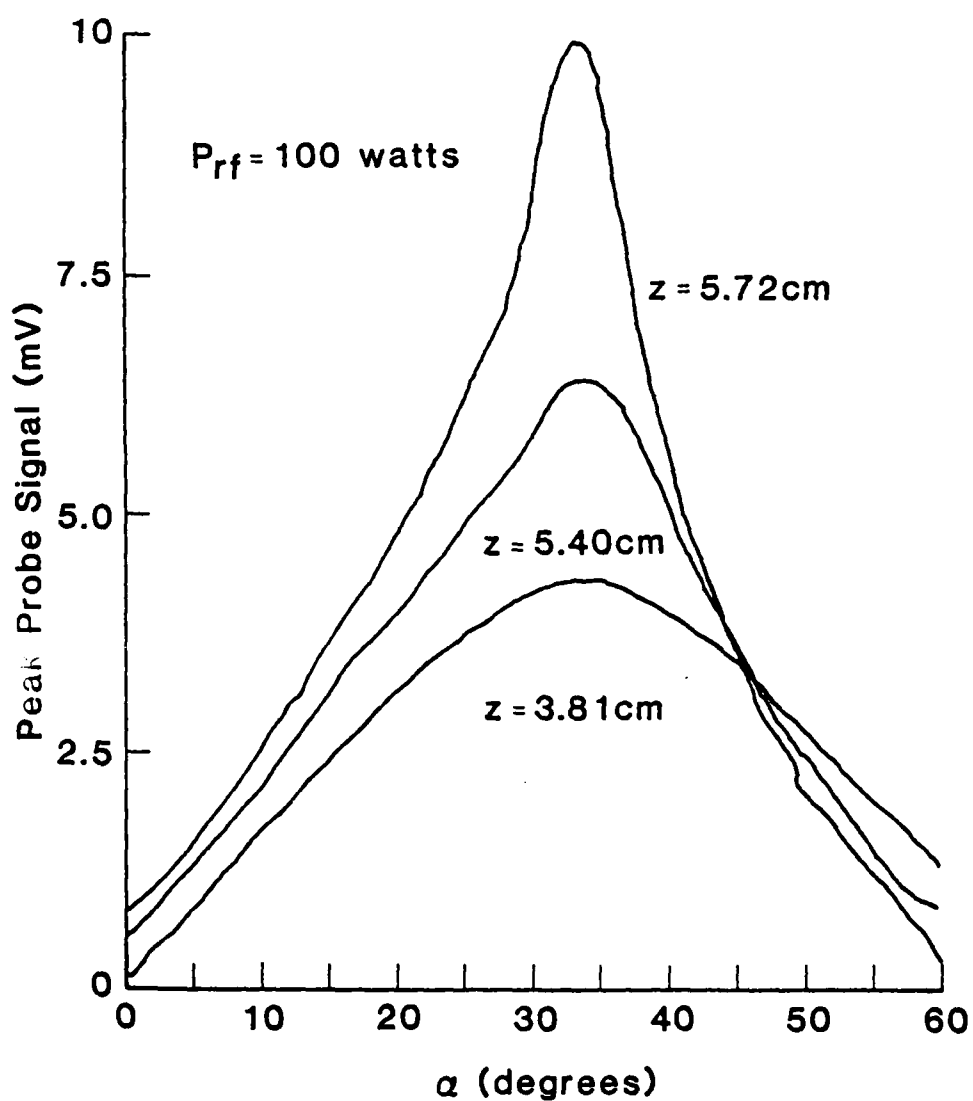


Fig. 4-15 Relative Magnitude of RF Potential vs. α
with z as a Parameter in Free Space

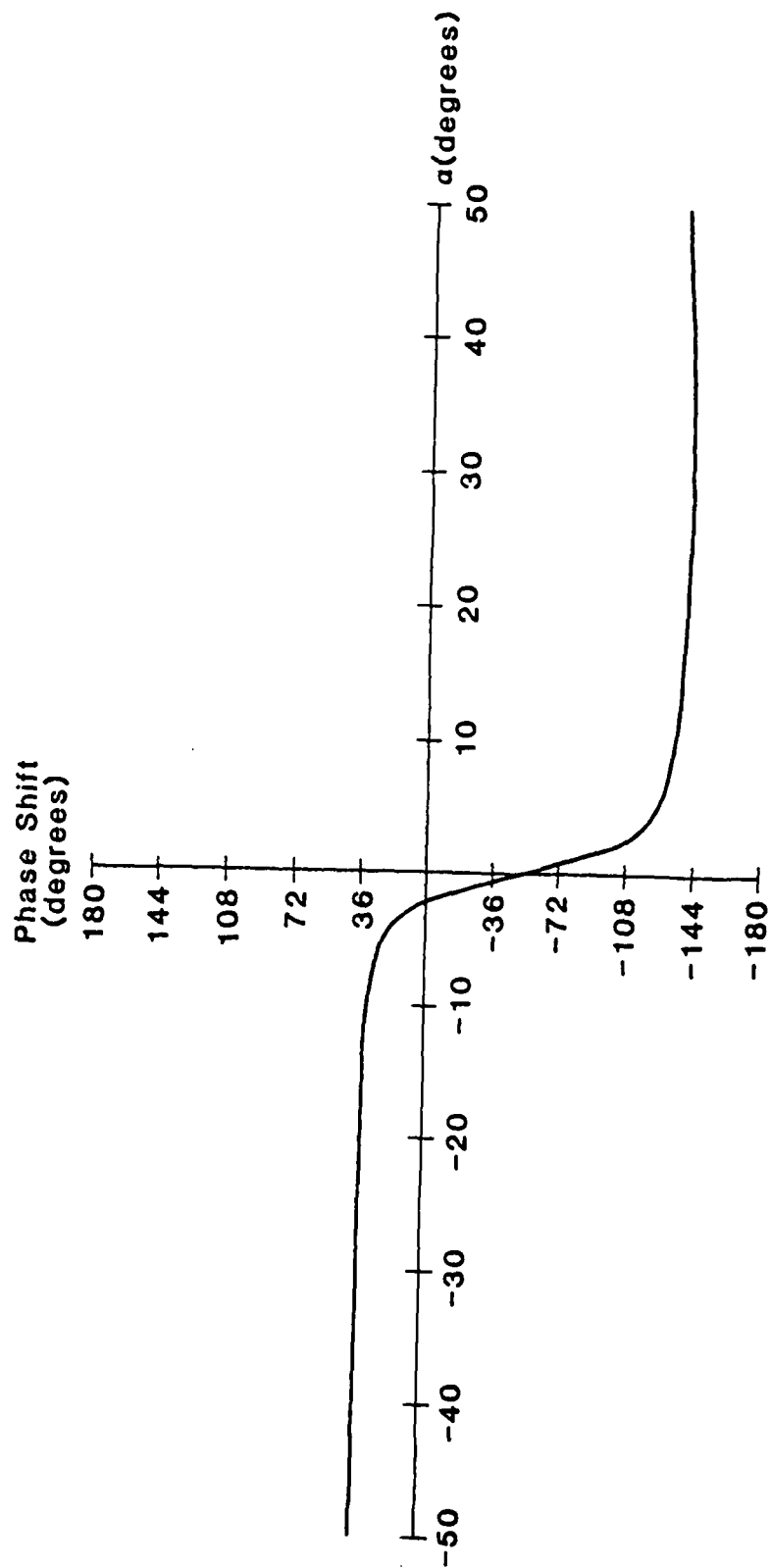


Fig. 4-16 α -Profile of Phase in Free Space

4.5 Experimental Results on the Interaction of the Plasma with Unidirectional RF Waves Excited by the Slow Wave Structure

This section is devoted to a detailed compilation of experimental results involving the excitation of the plasma by rf fields from the slow wave structure. Unidirectional slow waves propagating on the exciting structure can be set up with $k_{z0} > 0$ or $k_{z0} < 0$ by interchanging the power feed points and the terminating 50Ω loads on the delay lines as discussed in section 2.6. Experimental results are given for both $k_{z0} > 0$ and $k_{z0} < 0$ excitations. Results on the following topics are included in this section; (1) the radial and axial profiles of electron density, electron temperature, and ion saturation current for different rf powers, (2) the radial profile, azimuthal profile and rf power dependence of axial electron flux, (3) the affect of rf power on the electron energy distribution function, and (4) the radial and axial profiles of the amplitude and phase of the rf potential as a function of rf power.

The results of the rf modification of the electron density and ion saturation current profiles are shown in Figs. 4-17 to 4-19. Fig. 4-17 shows the electron density versus r^2 and Figs. 4-18 and 4-19 show the ion saturation current versus α for different rf powers, P_{rf} , as well as for $k_{z0} > 0$ and $k_{z0} < 0$.

Even though the electron density profiles are not Gaussian for $P_{rf} \neq 0$, it is seen from Fig. 4-17 that it is possible to assume a local Gaussian profile for $r \geq 2.5$ cm with a local radial scale length equal to the radial scale length of the unperturbed plasma. It should be noted that the absolute electron density decreases as the rf power is increased. It is also found that for a given rf power the density profile for a $k_{z0} < 0$ excitation is smaller than for a $k_{z0} > 0$ excitation. These results are corroborated by the α -profiles of ion saturation current. Experimental results also indicate that the axial electron density gradient is not affected along the slow wave structure. To understand the wave-particle dynamics, it is important to be familiar with these modified density profiles.

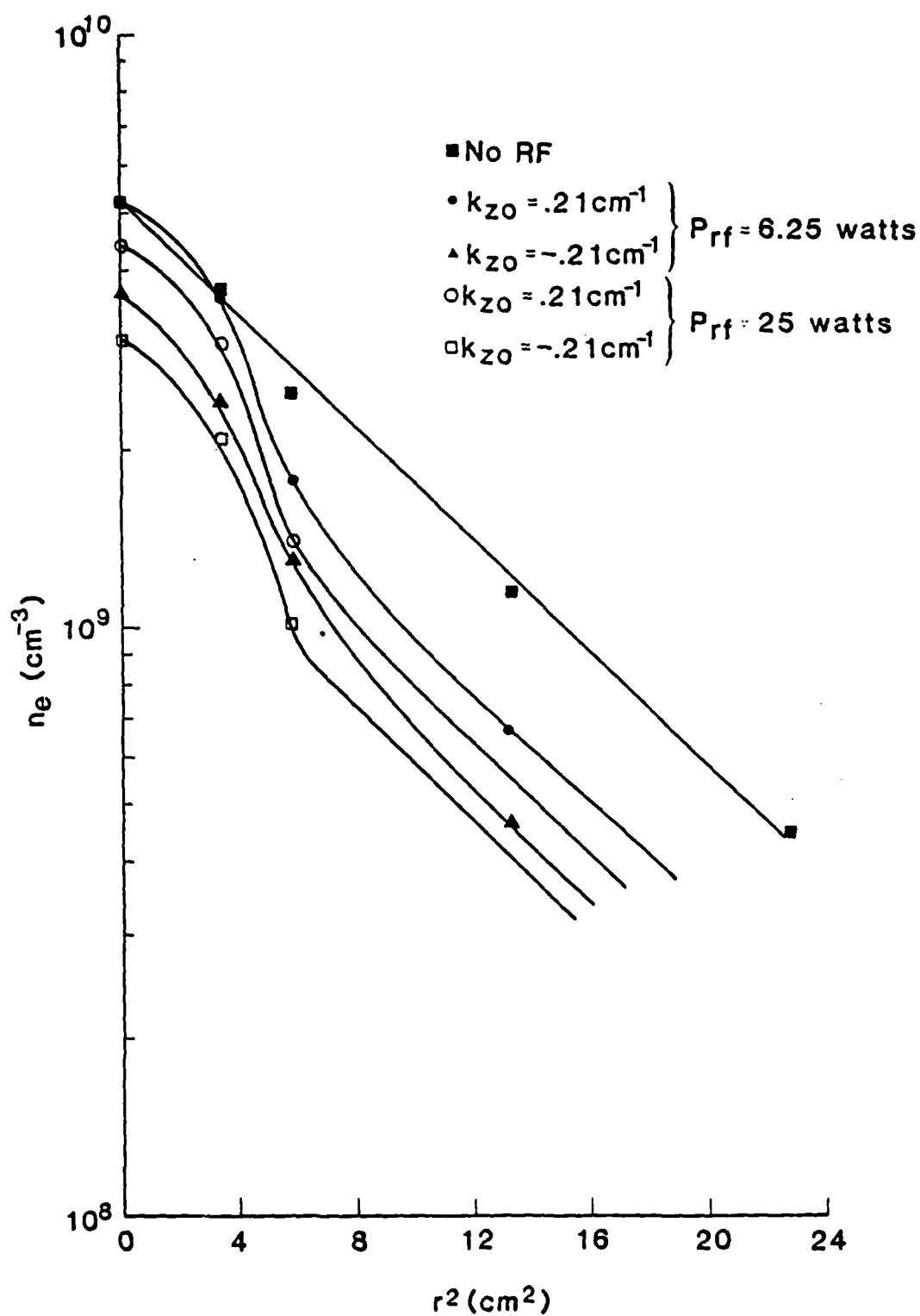


Fig. 4-17 Electron Density vs. r^2 with k_{z0} and P_{rf} as a Parameter at $z = -3.81 \text{ cm}$

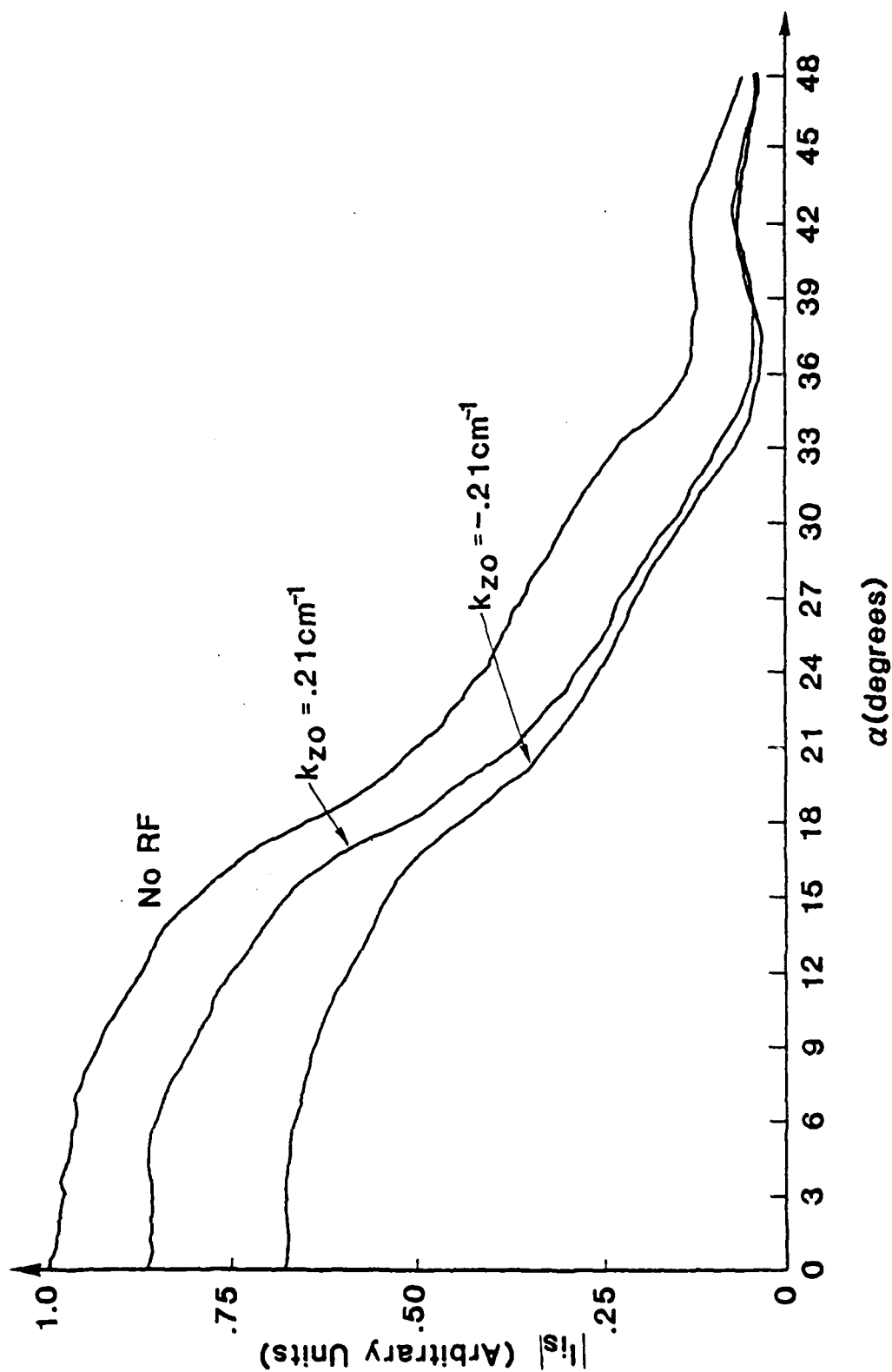


Fig. 4-18 Magnitude of Ion Saturation Current vs. α for $P_{rf} = 6.25$ Watts

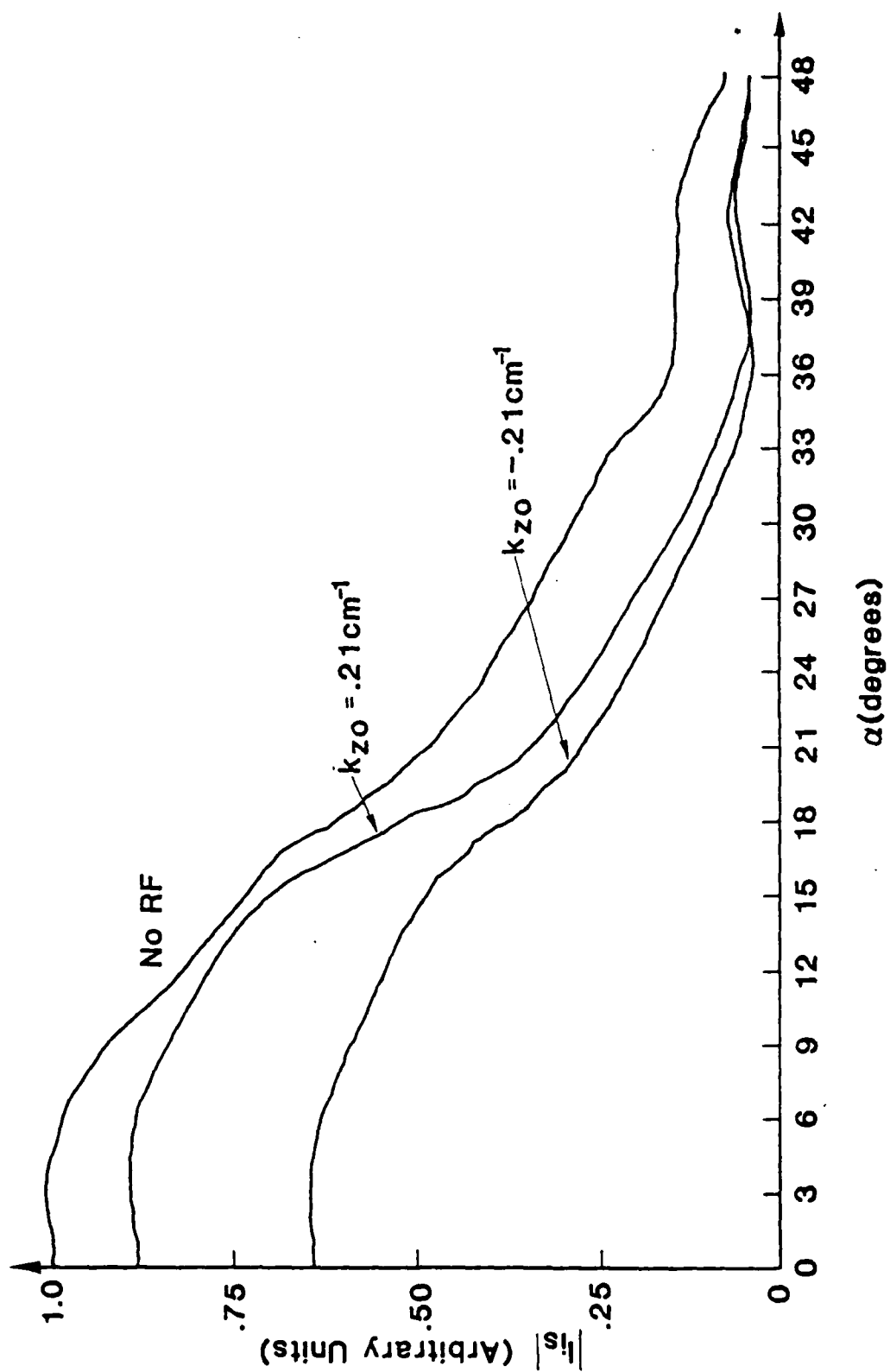


Fig. 4-19 Magnitude of Ion Saturation Current vs. α for $P_{rf} = 25$ Watts

Radial and azimuthal dc current probes are used to measure the profiles of axial electron flux in the plasma as described in section 3.3. These measurements are made as a function of rf power and the direction of excitation of the slow wave structure. α -profiles of electron flux for various rf powers are shown in Figs. 4-20 and 4-21 for $k_{z0} = .21 \text{ cm}^{-1}$ and $k_{z0} = -.21 \text{ cm}^{-1}$ respectively. The azimuthal electron flux at a radius of 3.8 cm is shown in Fig. 4-22. Fig. 4-22 applies for both $k_{z0} > 0$ and $k_{z0} < 0$ excitations.

As can be seen in Figs. 4-20 and 4-21 there are two radially localized regions of axial electron flux. Plots of the peak electron current density for peaks A and B (see Figs. 4-20 and 4-21) as a function of rf power for $k_{z0} > 0$ and $k_{z0} < 0$ are shown in Figs. 4-23 and 4-24. Fig. 4-25 shows the radial location of peak A of the electron flux as a function of rf power for $\pm k_{z0}$ excitations.

If the microwave power used for ECRH is reduced, the radial profiles of electron flux are radically altered. Figs. 4-26 and 4-27 show the effect of the reduction in ECRH power on the α -profile of axial electron current density for $k_{z0} > 0$ and $k_{z0} < 0$ respectively. From Fig. 4-10 it is seen that the ion saturation current and hence the electron density profiles are reduced as ECRH power is reduced and from Figs. 4-26 and 4-27, it is seen that peak A moves radially inward, and peak B remains in approximately the same radial position. Peak A moves inward in such a fashion that the location of this peak always corresponds to the same value of electron density. The electron density at this point is $n_e = 6 \times 10^8 \text{ cm}^{-3}$. Peak B remains approximately in the same position regardless of the power level used to excite the slow wave structure. The location of peak B also is not affected by the electron density profile. These results indicate peak A is due to the excitation of a plasma mode by the slow wave structure while peak B is probably due to the large axial electric fields located near the coupler plates. In this report we will be mainly concerned

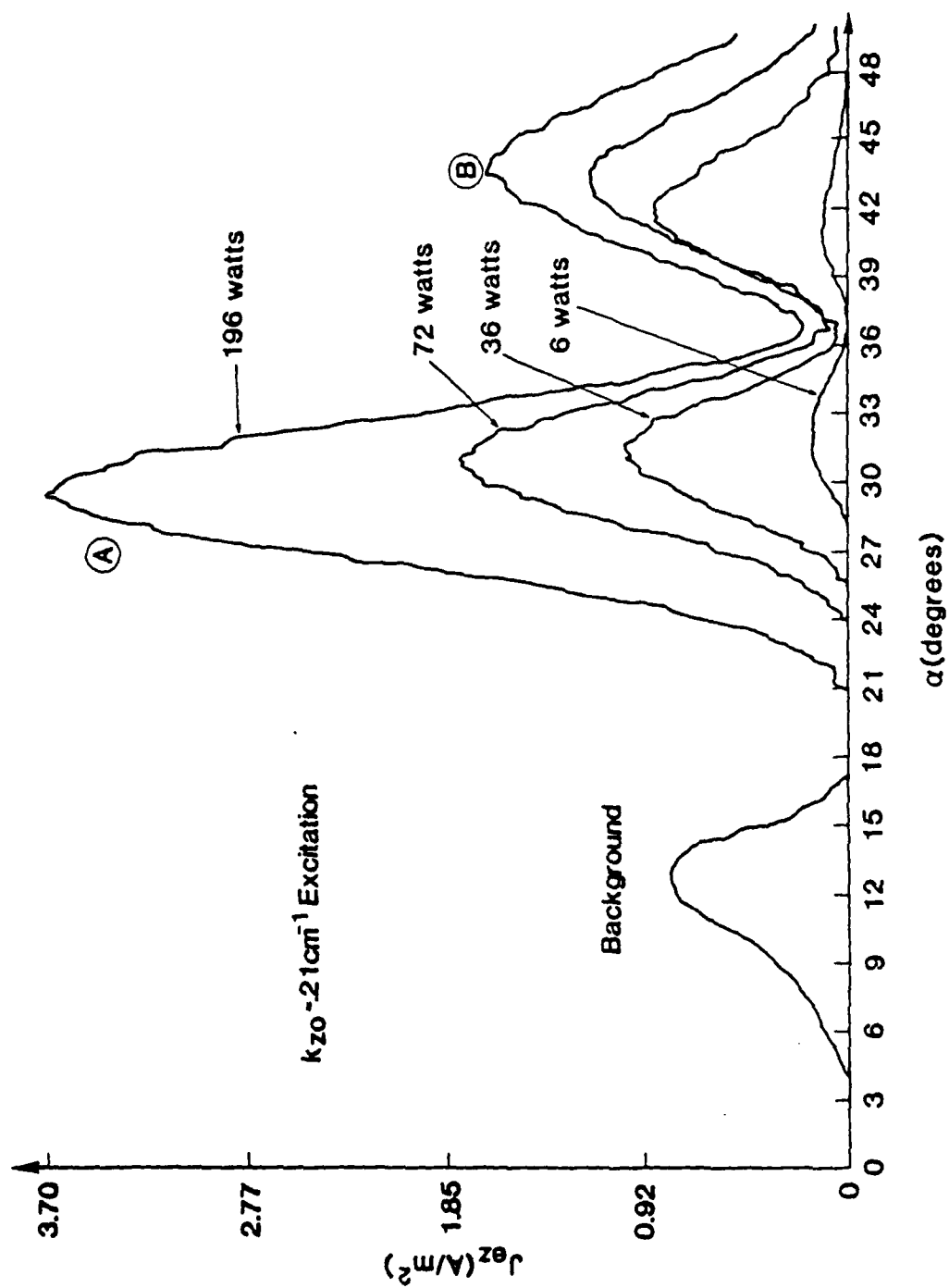


Fig. 4-20 α -Profiles of Axial Electron Current Density for $k_{z0} = 21 \text{ cm}^{-1}$

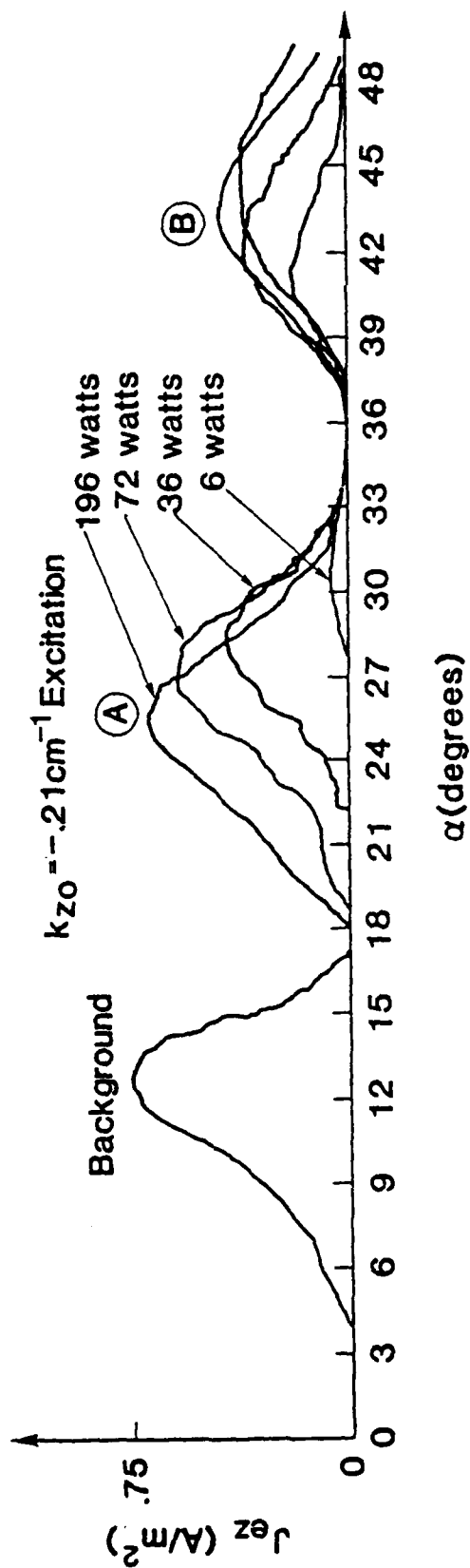


Fig. 4-21 α - Profiles of Axial Electron Current Density for $k_{z0} = -.21 \text{ cm}^{-1}$

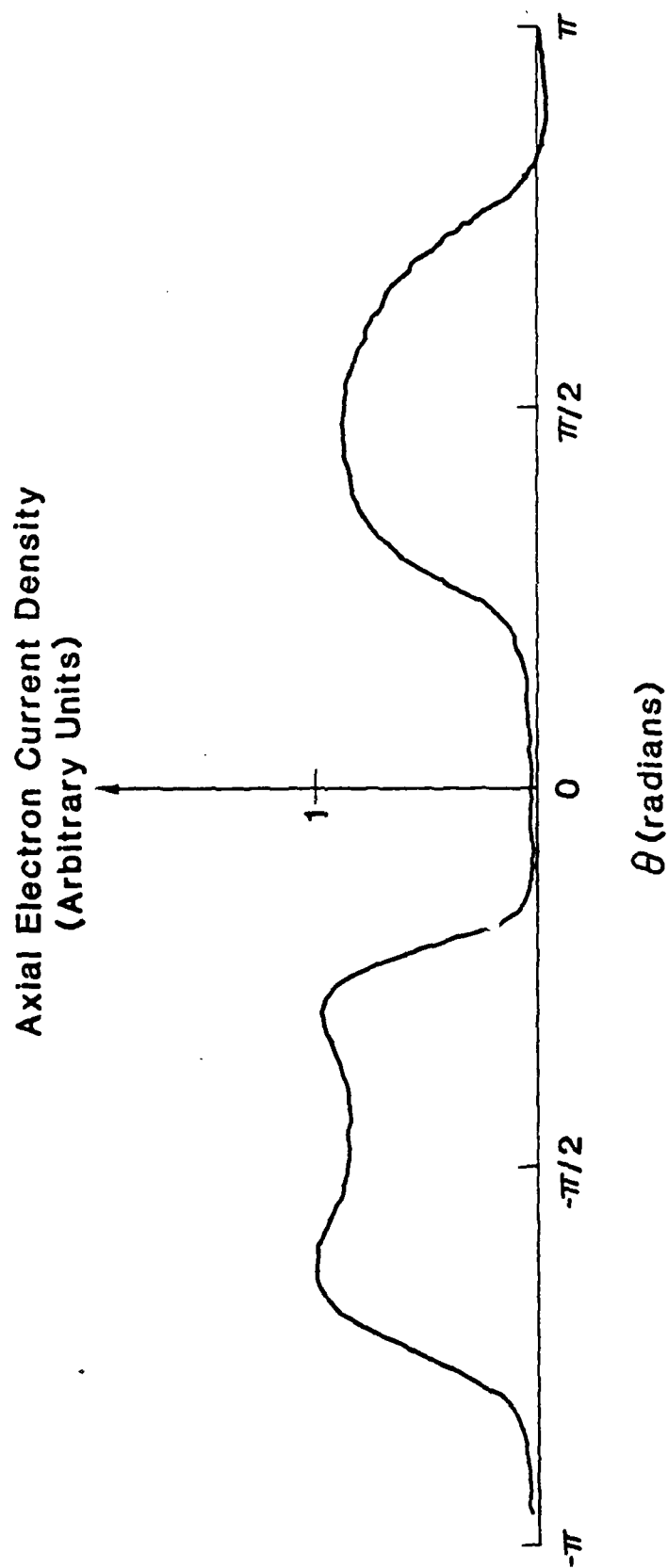


Fig. 4-22 Azimuthal Profile of Electron Current Density at $r = 3.81\text{cm}$

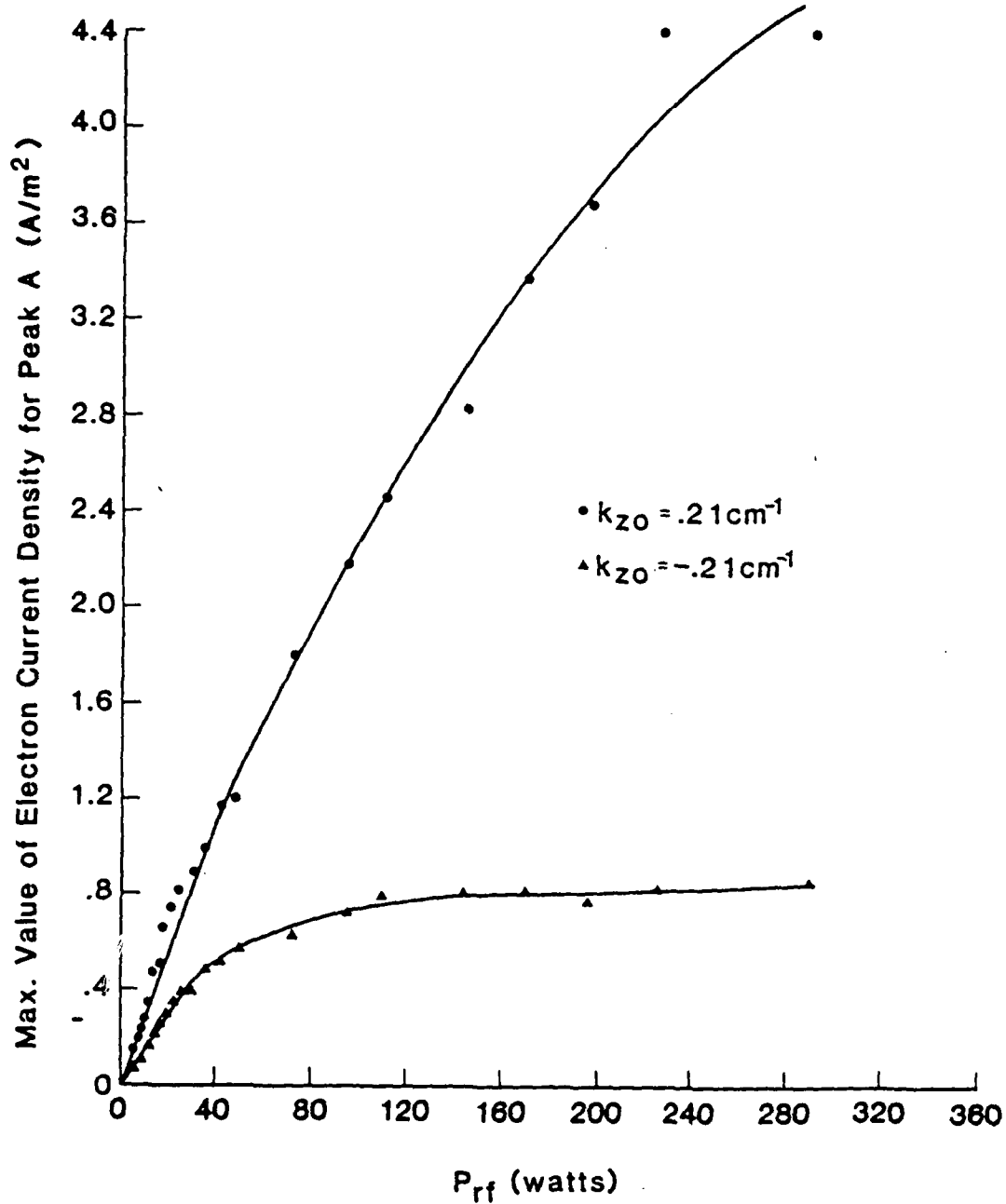


Fig. 4-23 Max. Value of Electron Current Density for Peak A vs. RF Power

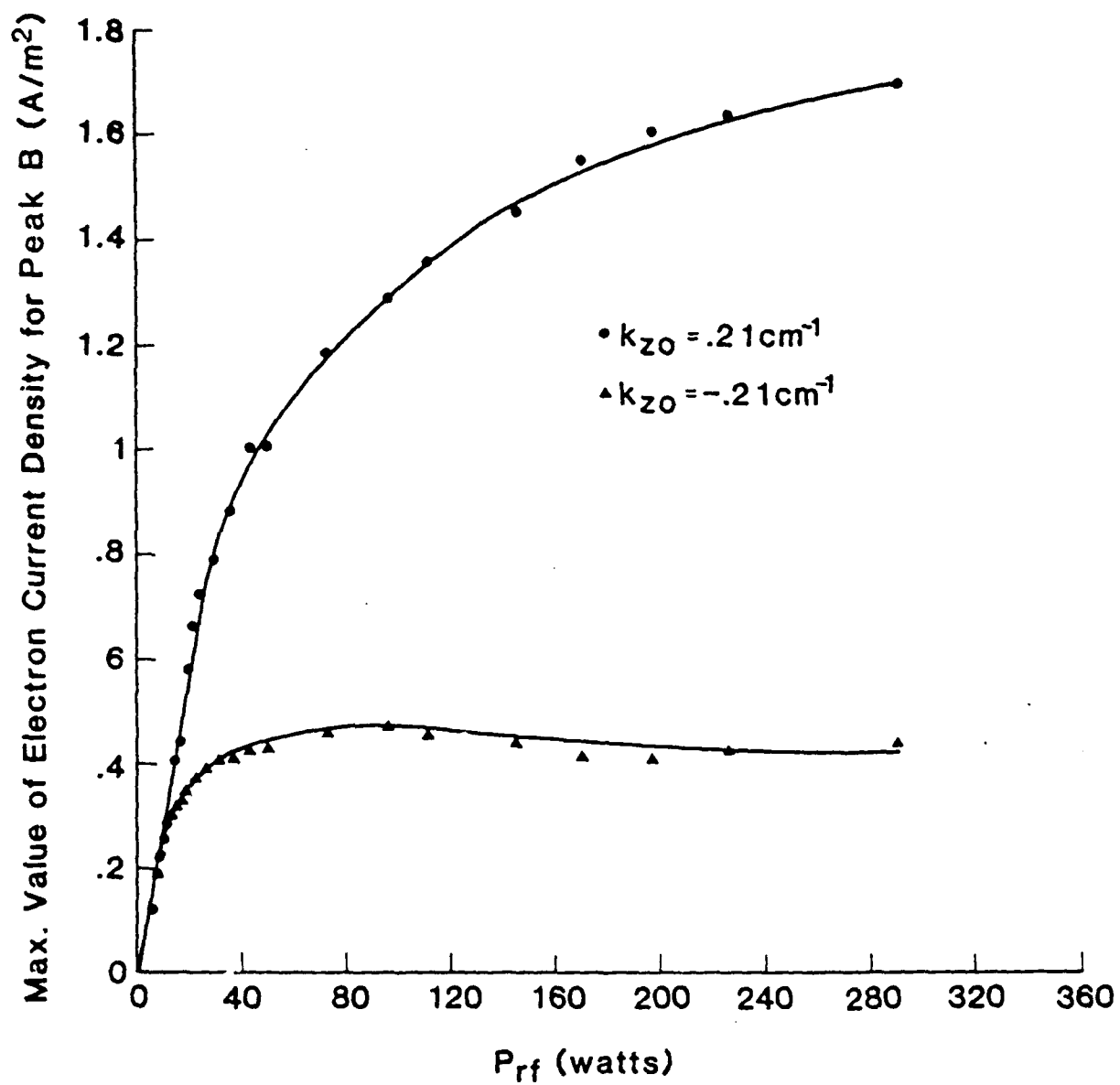


Fig. 4-24 Max. Value of Electron Current Density for Peak B vs. RF Power

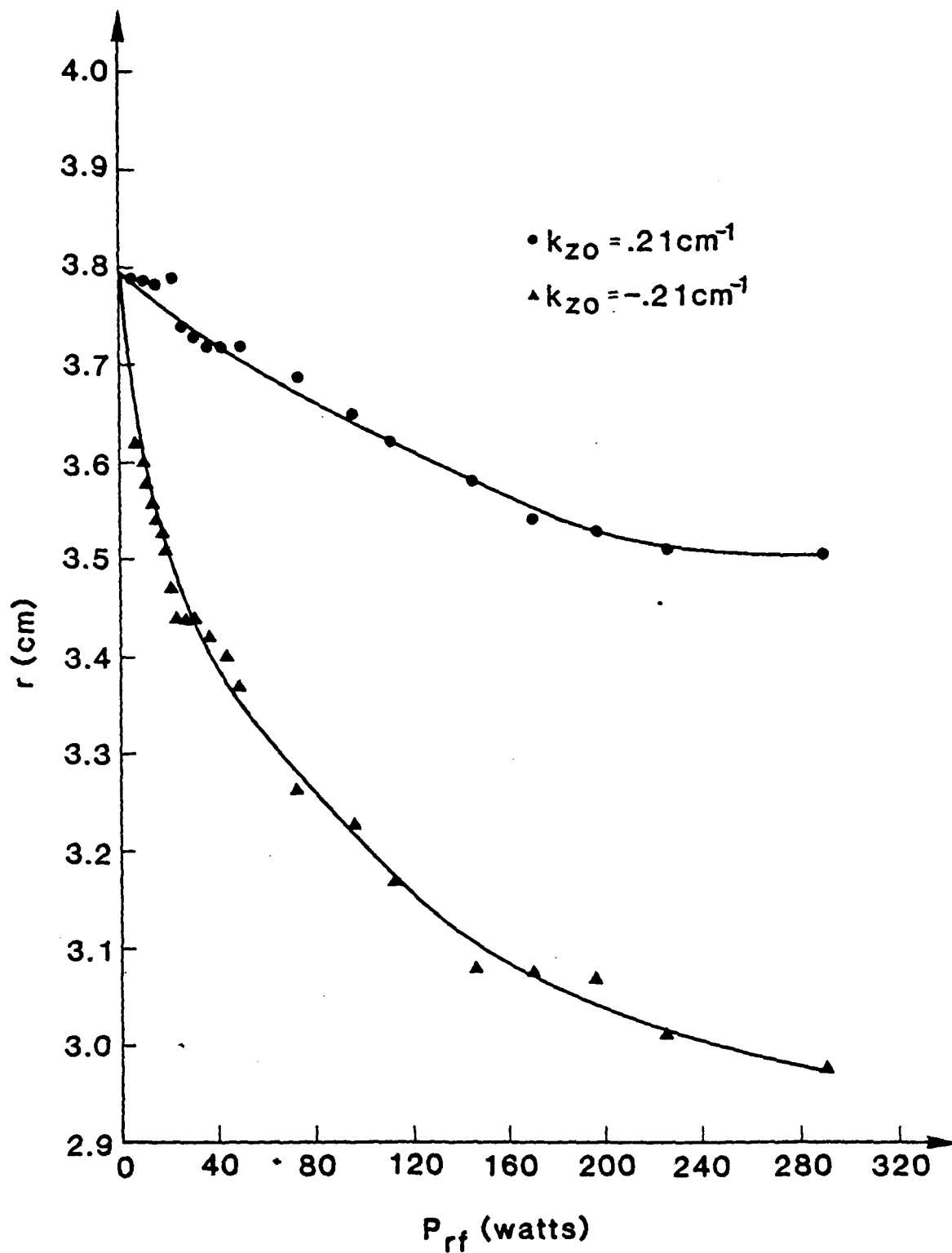


Fig. 4-25 Radial Location of Peak A of Electron Flux as a Function of RF Power

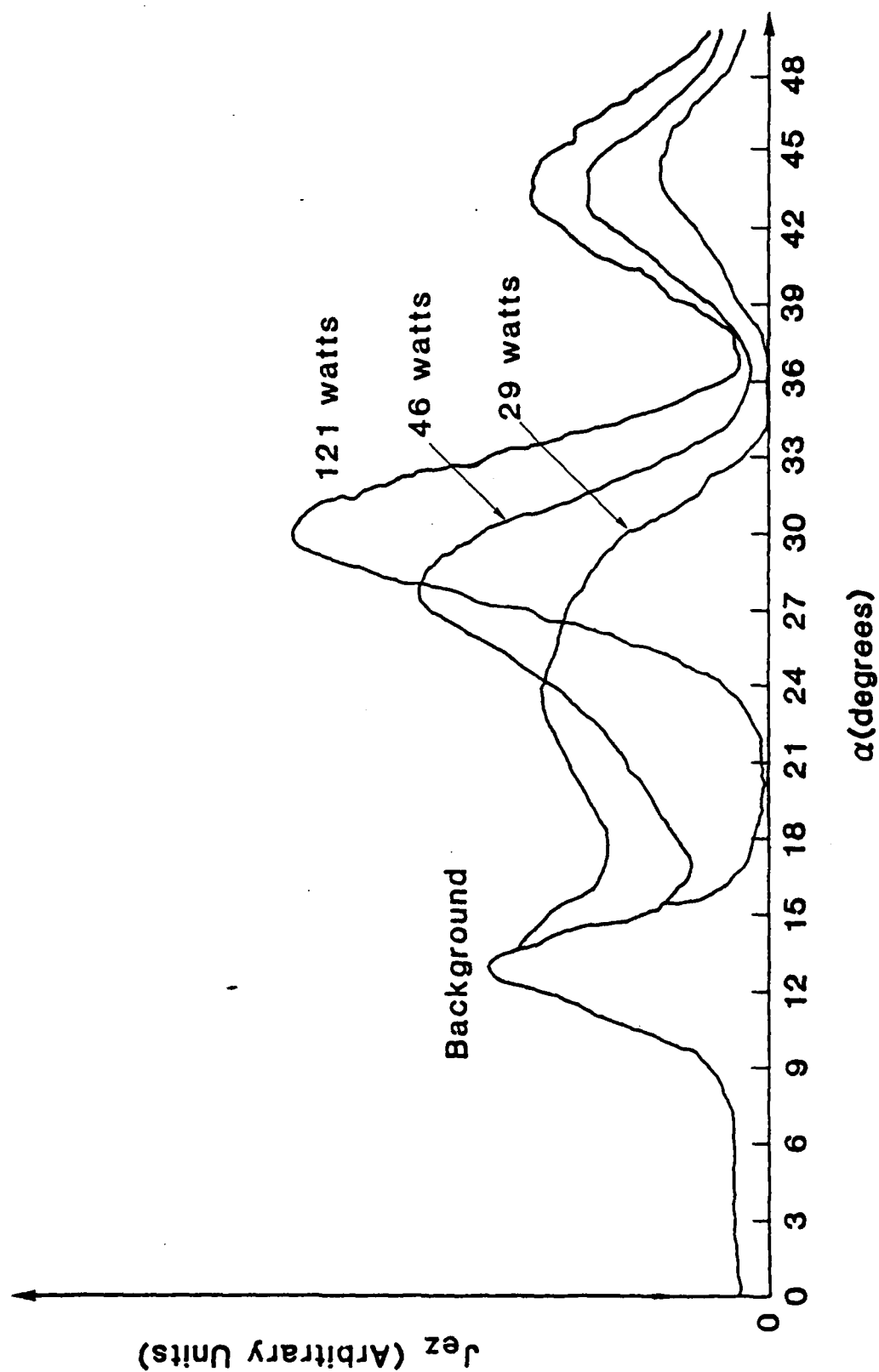


Fig. 4-26 Axial Electron Current Density vs. α
for $k_{z0} = .21\text{cm}^{-1}$ with ECRH Power as a Parameter

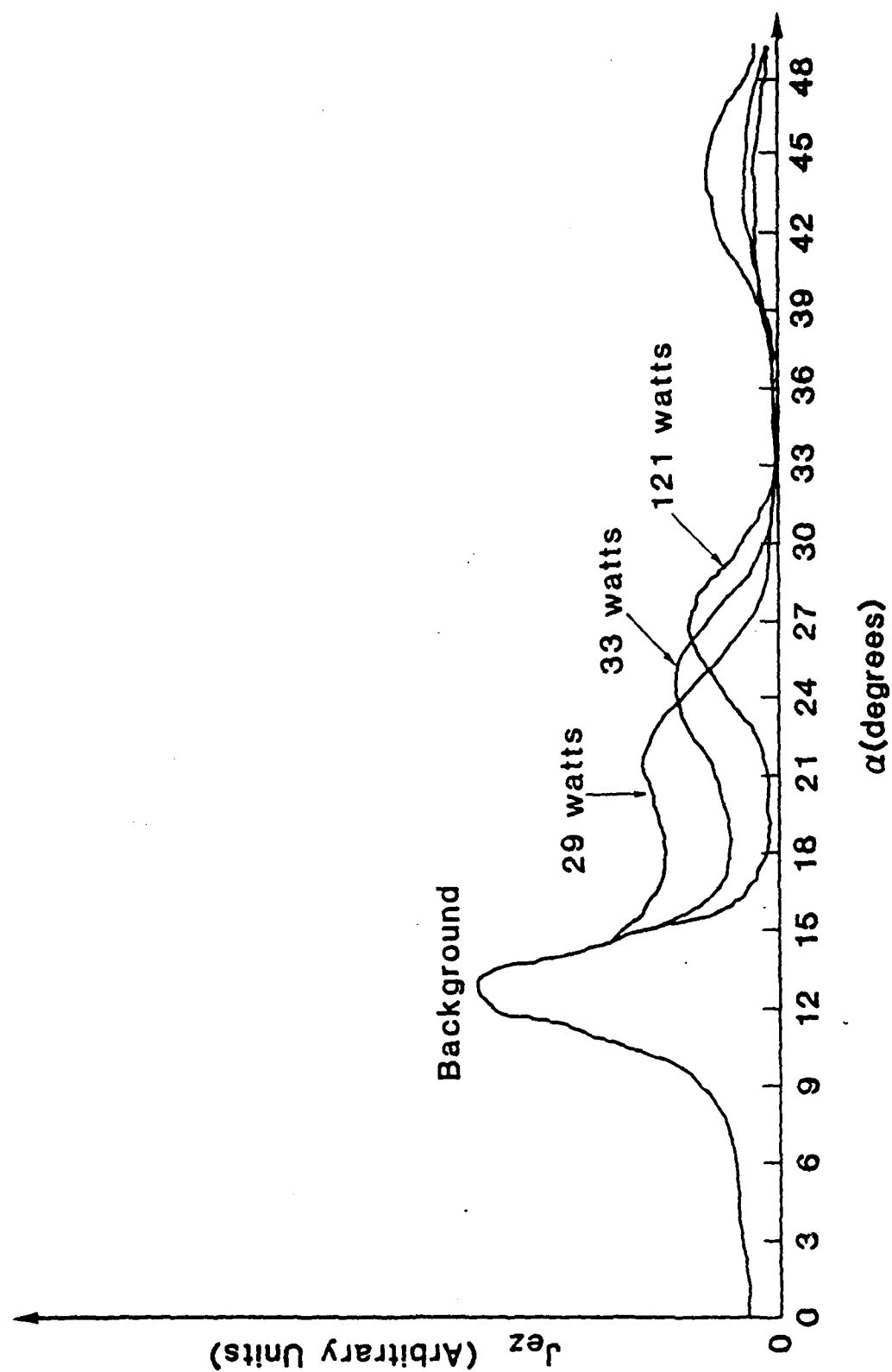


Fig. 4-27 Axial Electron Current Density vs. α
for $k_{z0} = -.21 \text{ cm}^{-1}$ with ECRH Power as a Parameter

with the electron flux associated with peak A. From Fig. 4-23 it is seen that for rf power levels less than approximately 40 watts, the electron current density increases linearly with applied rf power with slopes of $0.028 \text{ A/m}^2\text{-watt}$ and $0.014 \text{ A/m}^2\text{-watt}$ for $k_{zo} > 0$ and $k_{zo} < 0$ respectively. For power levels greater than approximately 100 watts the electron current density saturates for a $k_{zo} < 0$ excitation. These measurements are corroborated with measurements using the electrostatic energy analyzer.

Additional information on rf driven axial electron currents is obtained using the electrostatic energy analyzer. A superposition of typical electron energy distributions with rf power as a parameter are shown in Figs. 4-28 and 4-29 for $k_{zo} > 0$ and $k_{zo} < 0$ respectively. It is evident that for both $k_{zo} > 0$ and $k_{zo} < 0$ that there is a shift in the location of the peak of the distribution function to higher energies as the rf power is increased. Fig. 4-30 shows the shift in the location of the peak of the energy distribution function versus rf power and Fig. 4-31 shows the change in velocity corresponding to the energy peak versus rf power. If $\ln g(\phi)$ is plotted versus ϕ for ϕ greater than the energy corresponding to the peak of the distribution a straight line results whose slope determines the effective axial electron temperature, T_{ez} . Fig. 4-32 shows T_{ez} versus the applied peak rf voltage on the coupler plates. The relative value of axial electron flux $\langle nv_z \rangle$ and the average electron velocity $\langle v_z \rangle$ as determined from Eqs. 3.29 and 3.31 are plotted versus rf power in Figs. 4-33 and 4-34 respectively. From Fig. 4-33 it is seen that the axial electron flux increases linearly with rf powers less than 40 watts at a rate twice as large for $k_{zo} > 0$ than for $k_{zo} < 0$ corroborating the dc current probe results shown in Fig. 4-23. It is also observed that $\langle nv_z \rangle$ saturates for $P_{rf} \geq 100$ watts for $k_{zo} < 0$. Fig. 4-35 is a plot of the average kinetic energy of an electron $\langle \frac{1}{2} m_e v_z^2 \rangle$ as determined from Eq. 3.28 versus rf power for $\pm k_{zo}$ excitations. From Fig. 4-29 one observes the formation of a plateau in the distribution function

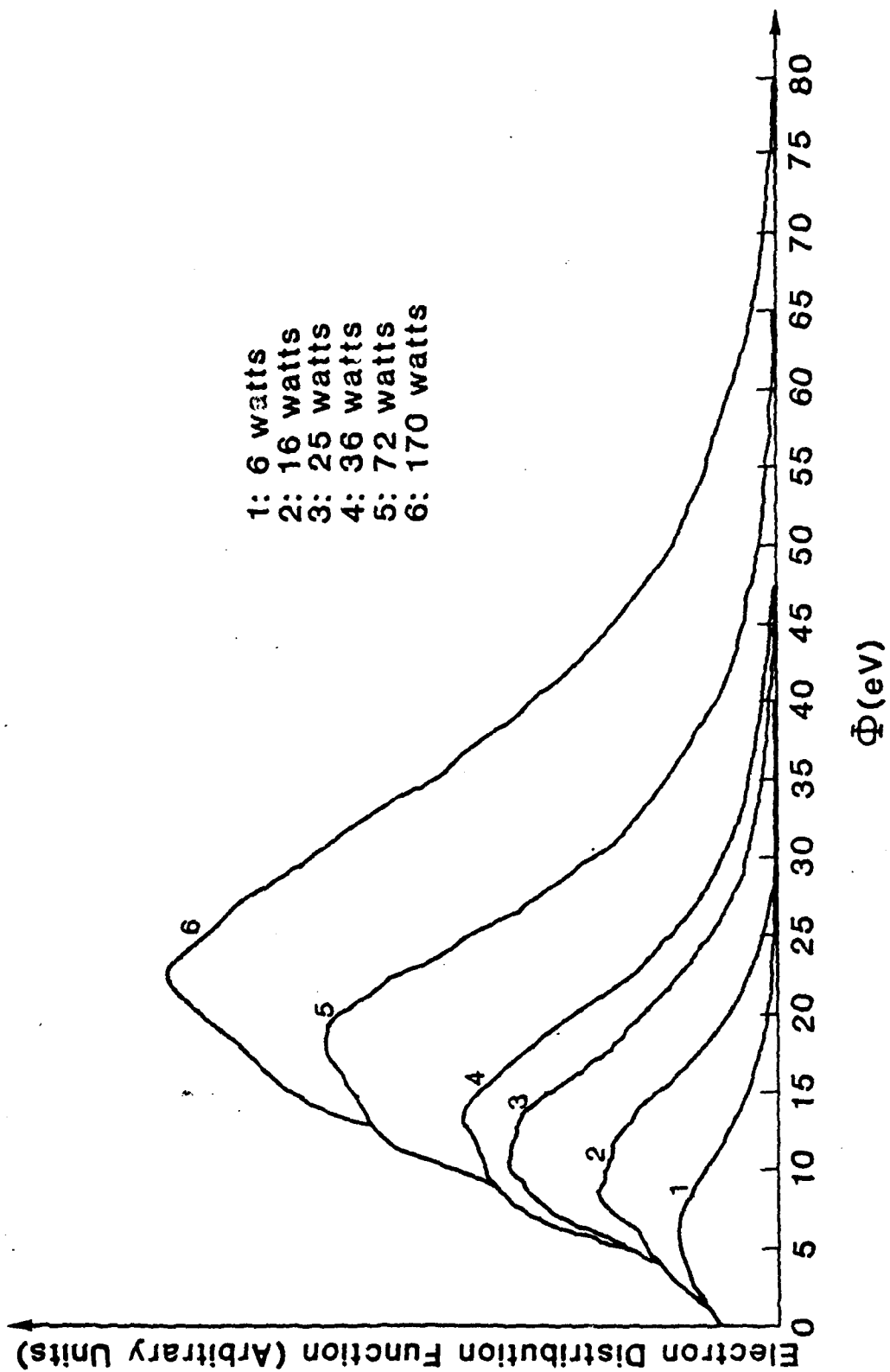


Fig. 4-28 Electron Energy Distribution for $k_{z0} = .21 \text{ cm}^{-1}$ with P_{rf} as a Parameter

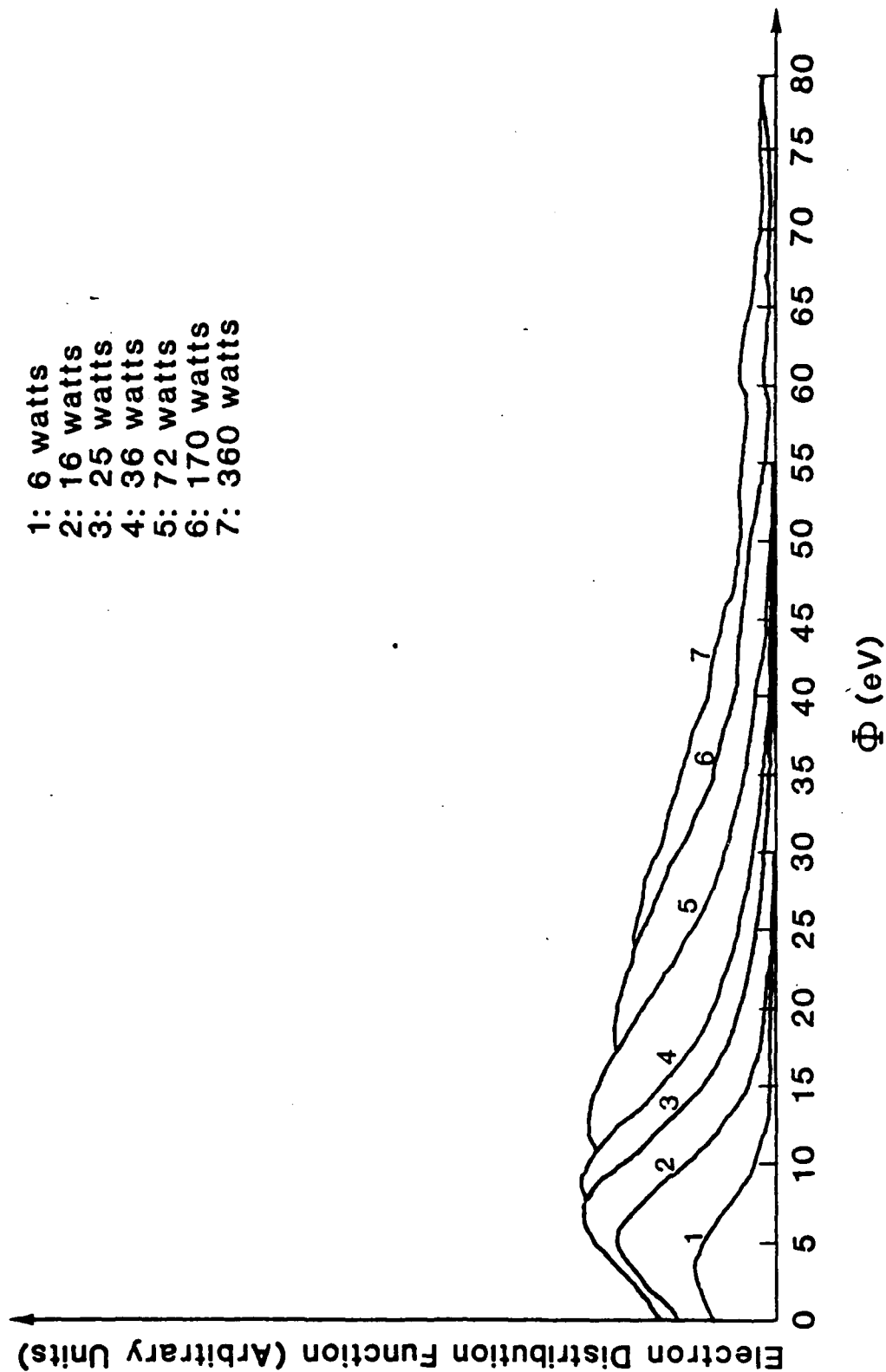


Fig. 4-29 Electron Energy Distribution for $k_{ZO} = -.21\text{cm}^{-1}$ with Prf as a Parameter

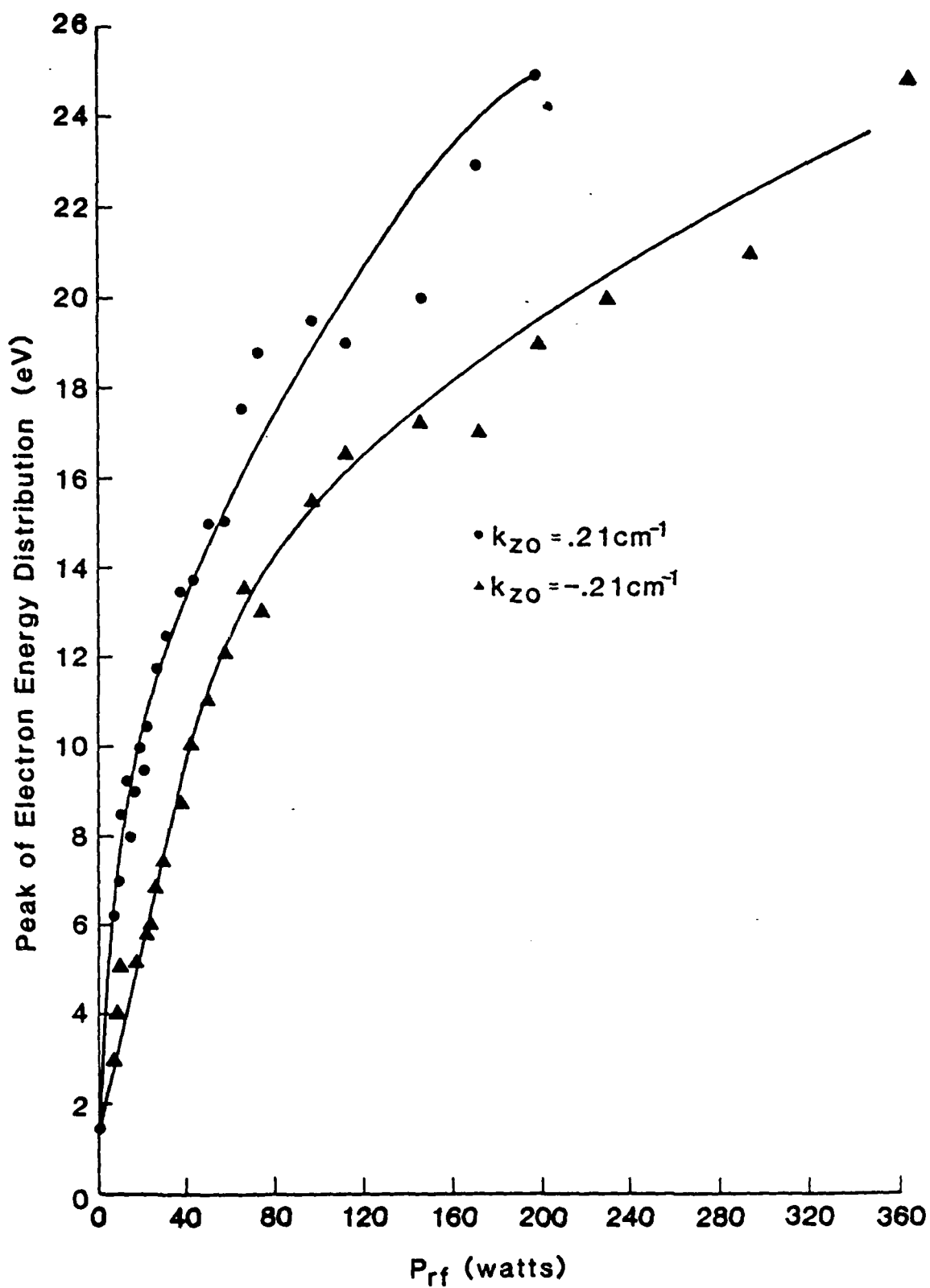


Fig. 4-30 Peak of Electron Energy Distribution vs. P_{rf}

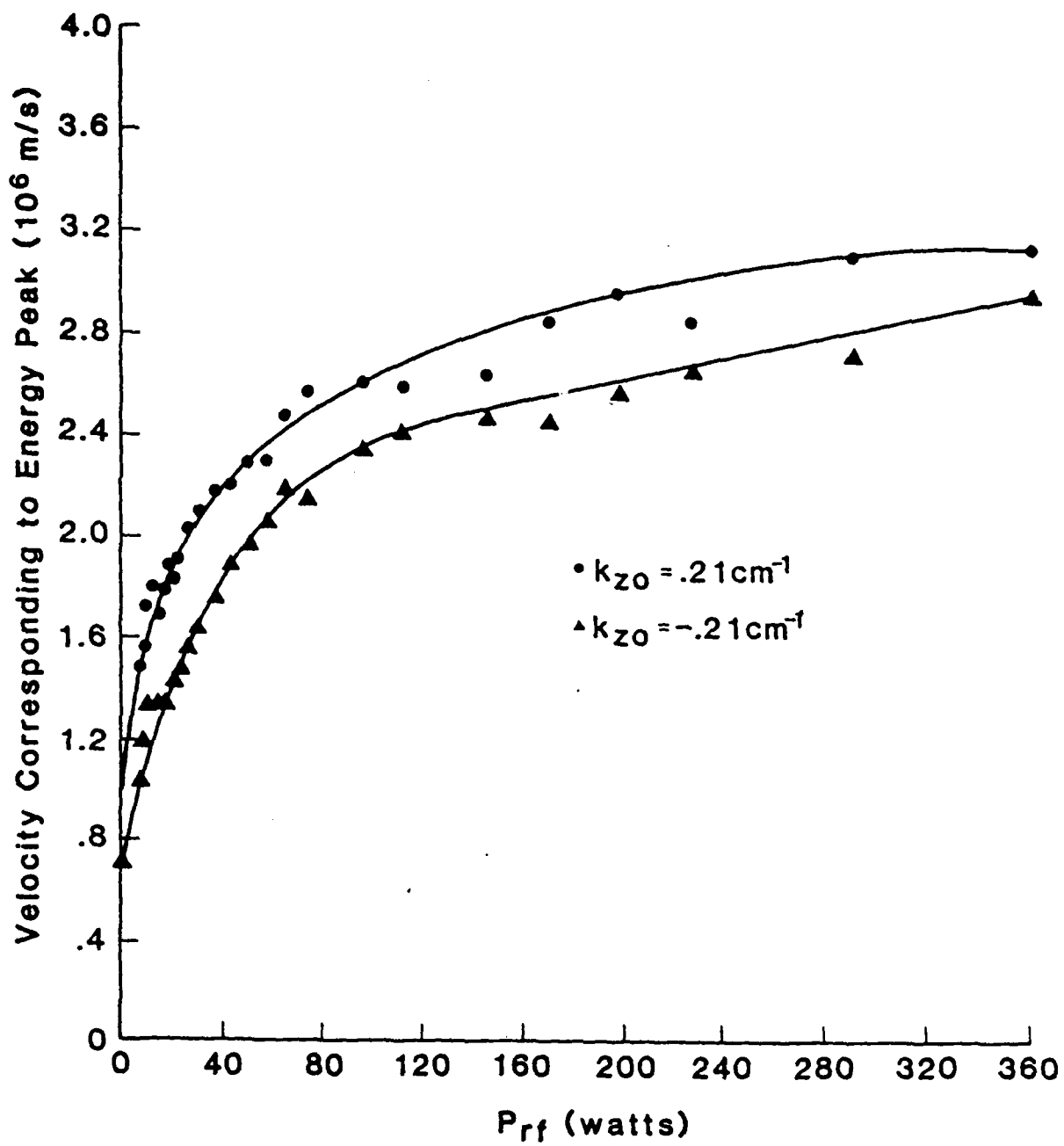


Fig. 4-31 Velocity Corresponding to Peak of
Energy Distribution vs. P_{rf}

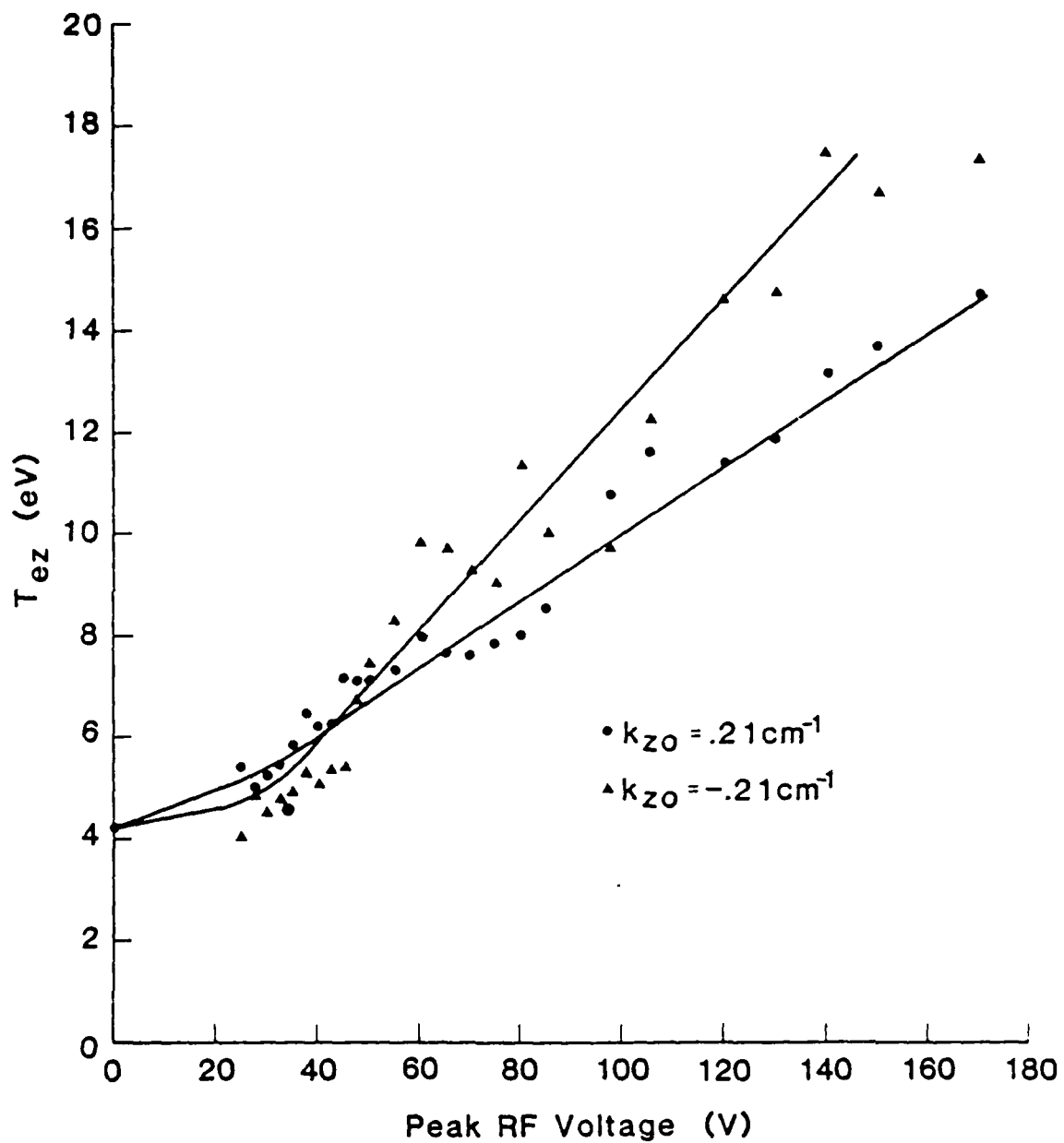


Fig. 4-32 Effective Electron Temperature vs. Peak RF Voltage

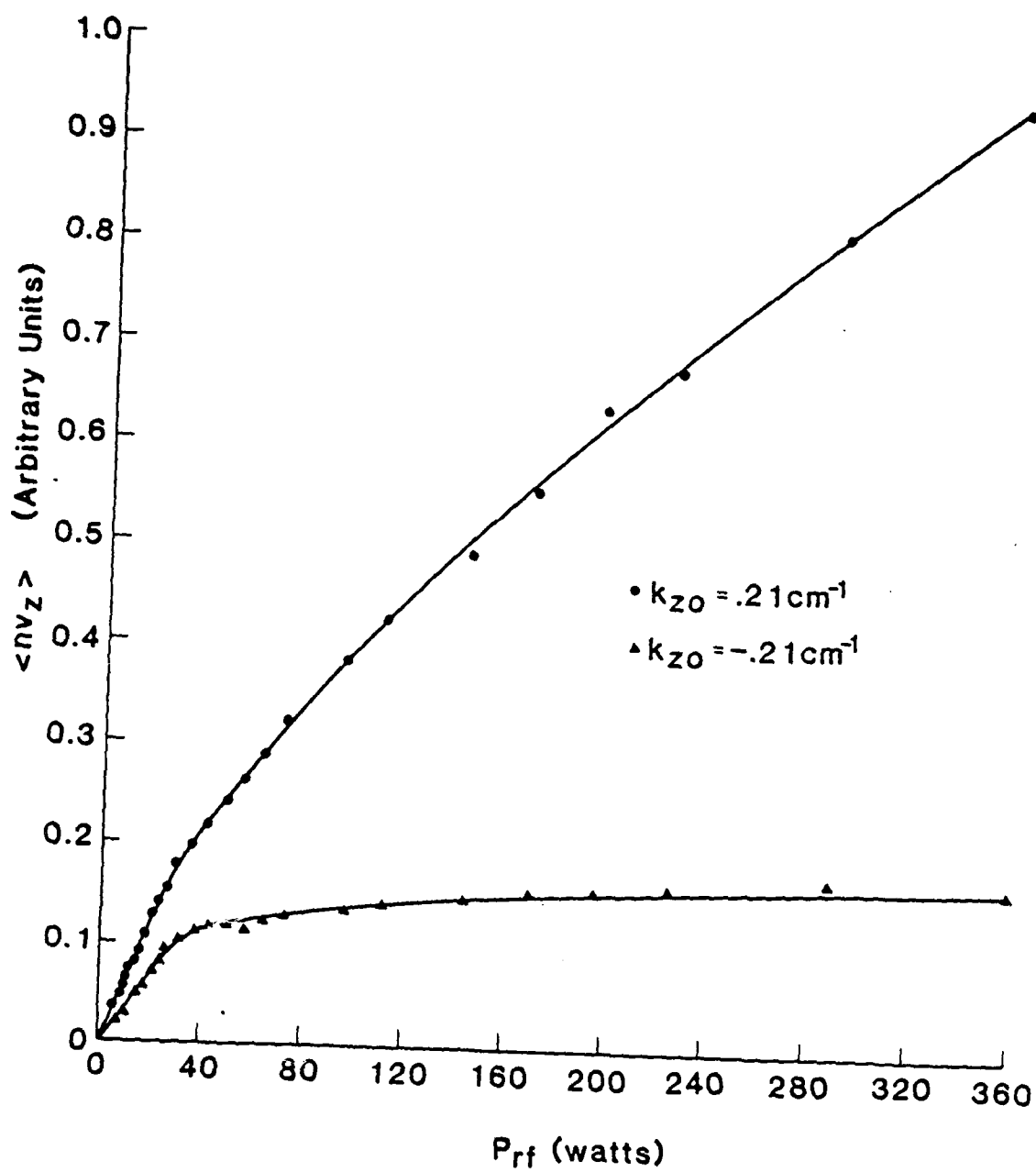


Fig. 4-33 Relative Value of Axial Electron Flux vs. RF Power

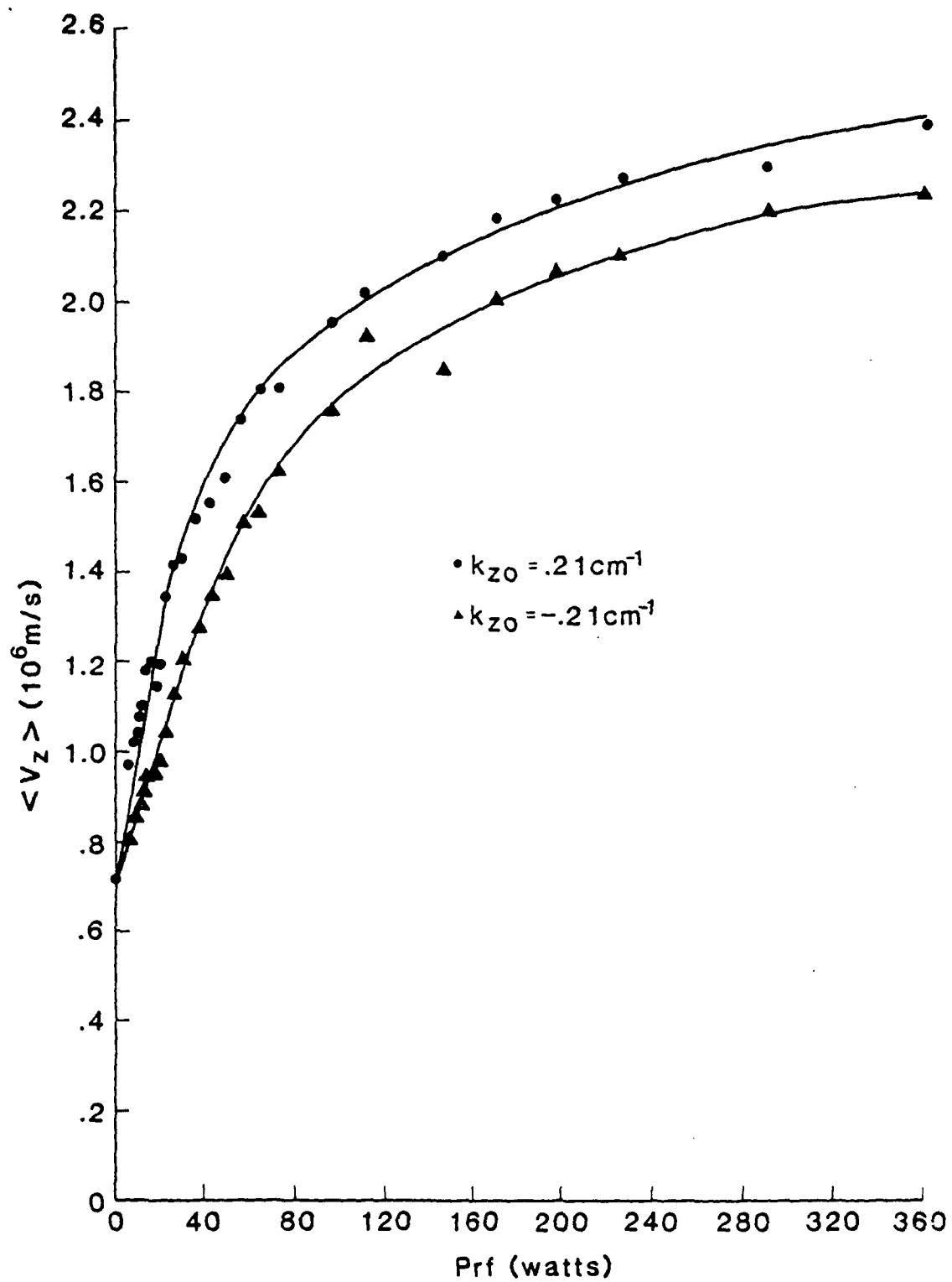


Fig. 4-34 Average Electron Velocity vs. Prf

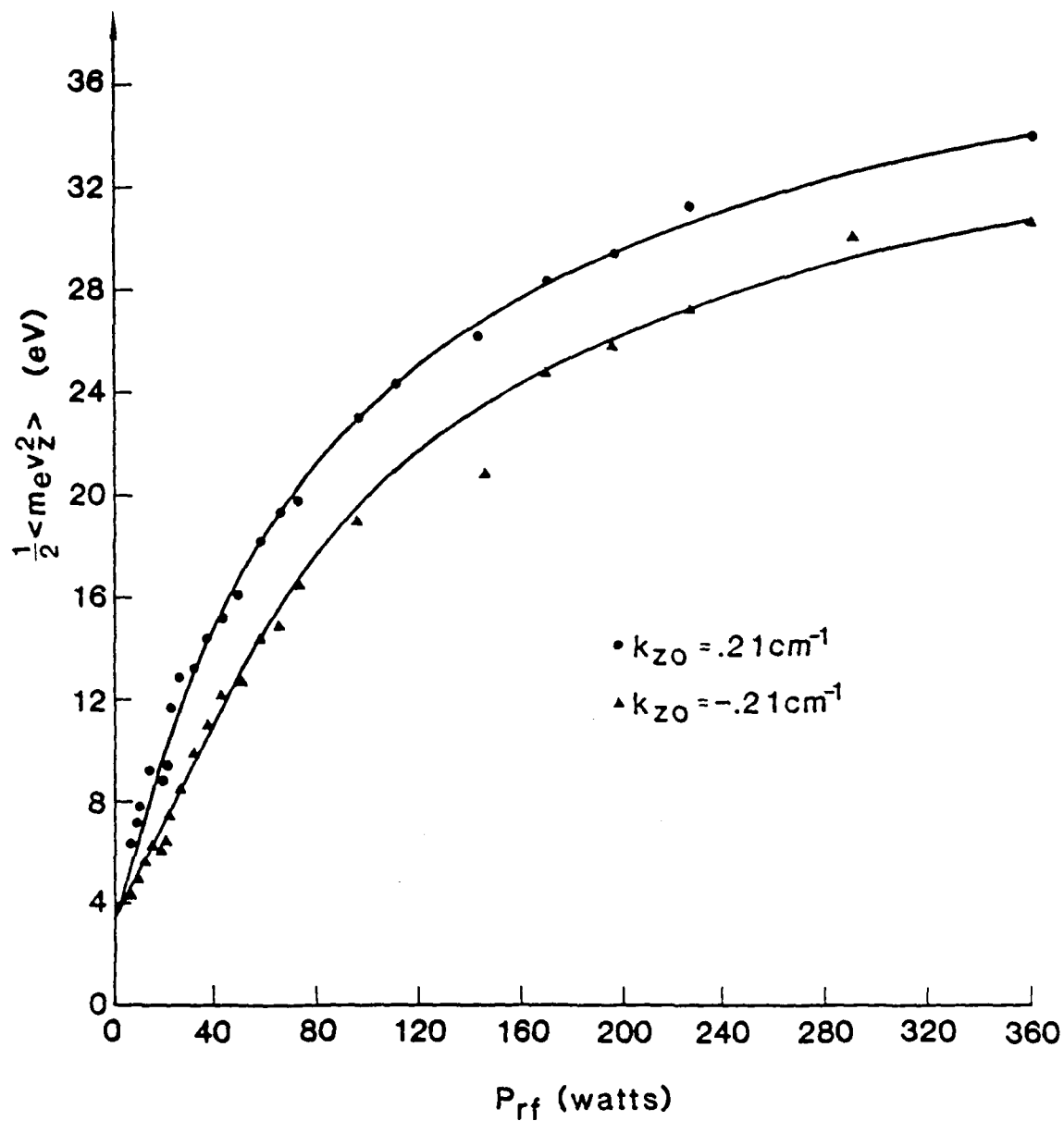


Fig. 4-35 Average Electron Kinetic Energy vs. RF Power

for power levels greater than 170 watts. Fig.4-36 is a typical semi-log plot of $g(\phi)$ versus ϕ showing the development of the plateau for energies greater than approximately 50eV.

Up to this point we have concentrated on an experimental description of the electron dynamics. We will now concentrate on the experimental results from the rf probe which will yield some information on the wave dynamics in the plasma. The rf measurements consist of amplitude and phase profiles at various axial locations in the plasma. The α -profile of the amplitude of the rf potential is shown in Fig. 4-37. The free space amplitude profile is also shown for comparison. Fig.4-37 indicates a shielding of the rf field by the plasma. This result was observed in a numerical simulation by Decyk, et al.¹³ A sharp dip in the potential magnitude is seen at an angle of $\alpha = 27.5^\circ$. The maximum value of the peak rf amplitude is shown in Fig.4-38 as a function of the peak exciting voltage between adjacent coupler plates. Experimentally it is found that the magnitude of the rf potential decreases in the axial direction near peak A. Figs. 4-39 and 4-40 show typical α -profiles of phase for $k_{z0} > 0$ and $k_{z0} < 0$ excitations respectively at different axial positions for an rf power of 6.25 watts. Similar profiles are shown in Figs. 4-41 to 4-44 for rf powers of 25 watts and 196 watts. It is found that the region of maximum rate of change of phase, i.e., maximum k_r , the dip in the rf amplitude profile, and maximum electron current density always occur at the same radial position. Also corroborating these results is the fact that as ECRH power is reduced, the radial position of maximum k_r moves radially inward as indicated in Figs. 4-45 and 4-46 to the same radial position as the maximum electron flux as shown in Figs. 4-26 and 4-27. These rapid radial phase changes have been observed by Fisher and Gould²³ in the study of the formation of resonance cones in a plasma. It is interesting to note from Figs. 4-39 to 4-44 that a $k_{z0} < 0$ excitation generates fields with a positive k_z in the region of electron flux which indicates electrons are moving in the direction of wave motion. This is probably due to the fact that for $k_{z0} < 0$ the source is exciting rf fields toward a region of increasing electron density along z and the wave will experience a reflection as discussed by Briggs and Parker²² and Ott, et al.³⁰

AD-A135 880

AN INVESTIGATION OF RF CURRENTS IN A MAGNETIZED PLASMA
USING A SLOW WAVE..(U) POLYTECHNIC INST OF NEW YORK
FARMINGDALE DEPT OF ELECTRICAL E.. B R POOLE ET AL.

2/2

UNCLASSIFIED

OCT 83 POLY-EE-83-004 AFOSR-TR-83-1057

F/G 20/3

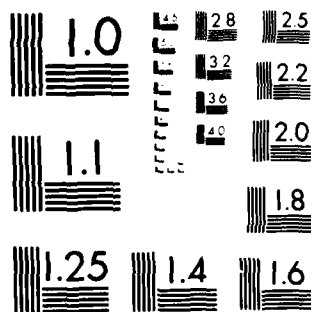
NL

END

DATE
FILMED

11-84

DTIC



MICROCOPY RESOLUTION TEST CHART
NATIONAL BUREAU OF STANDARDS-1963-A

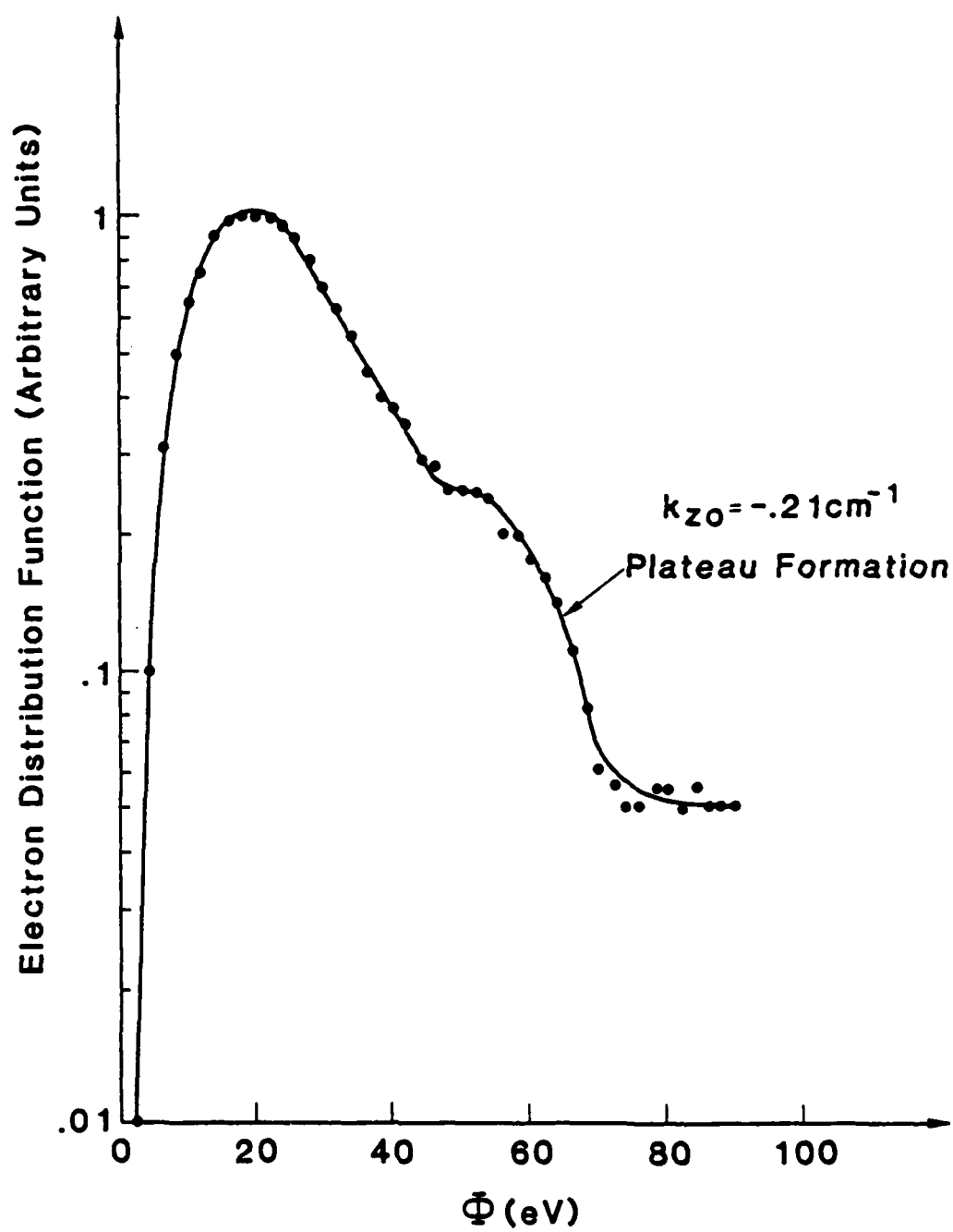


Fig. 4-36 Electron Energy Distribution for $P_{rf}=225$ watts

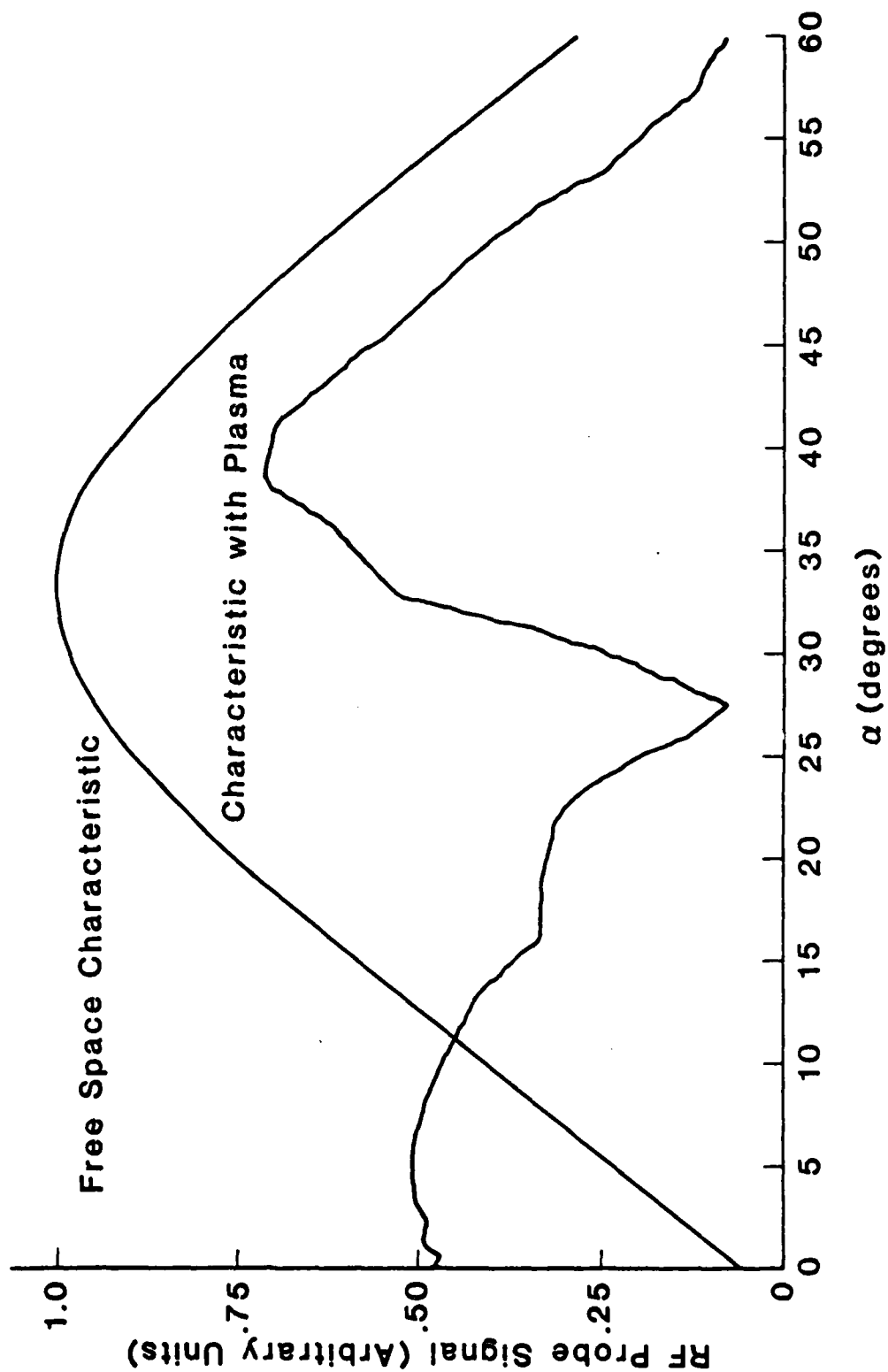


Fig. 4-37 α - Profile of Relative RF Amplitude

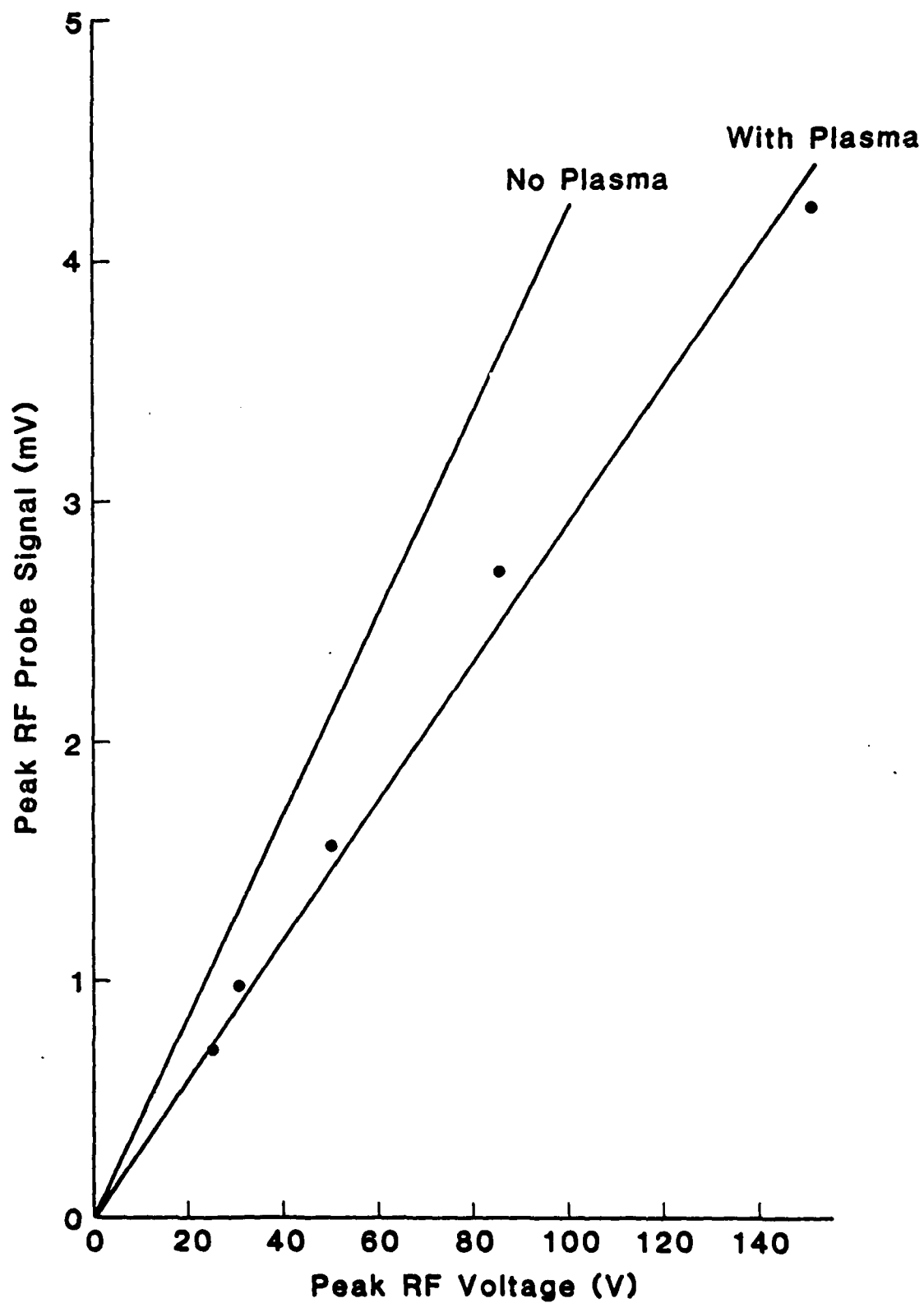


Fig. 4-38 Max. RF Probe Signal vs. Peak RF Voltage

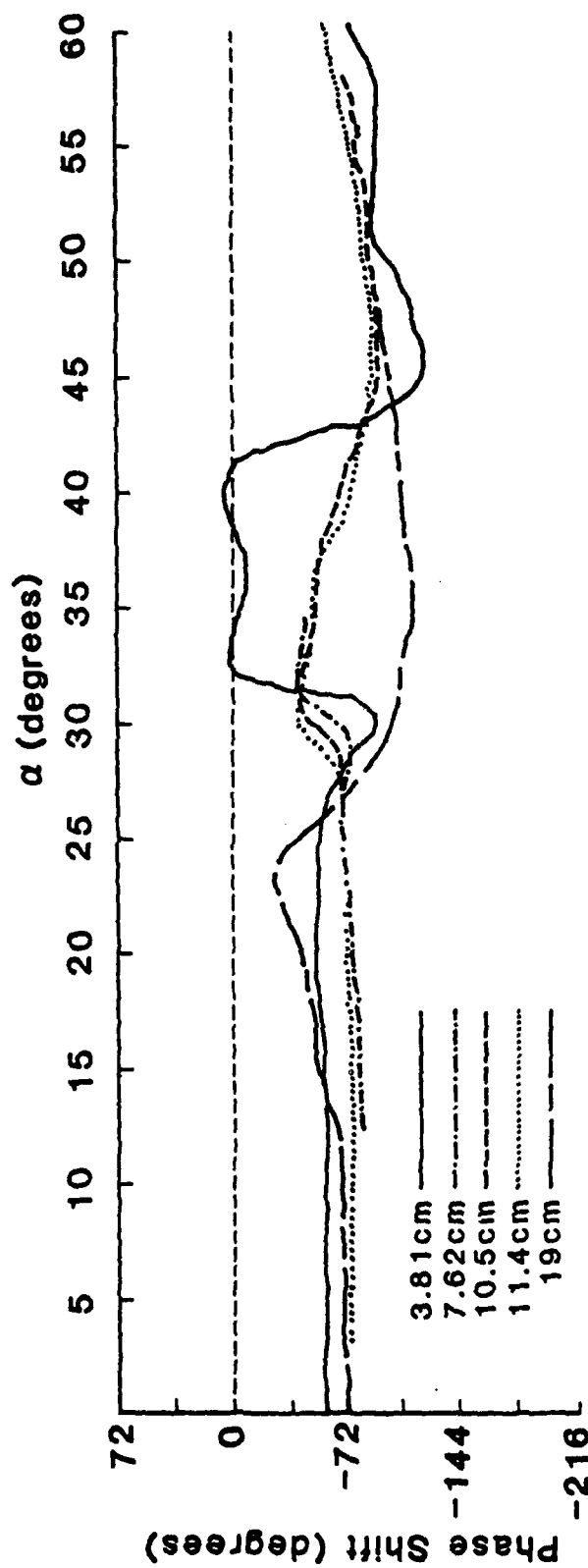


Fig. 4-39 α -Profiles of Phase for $k_{z0} = .21 \text{ cm}^{-1}$
and $P_{rf} = 6.25$ Watts with z as a Parameter

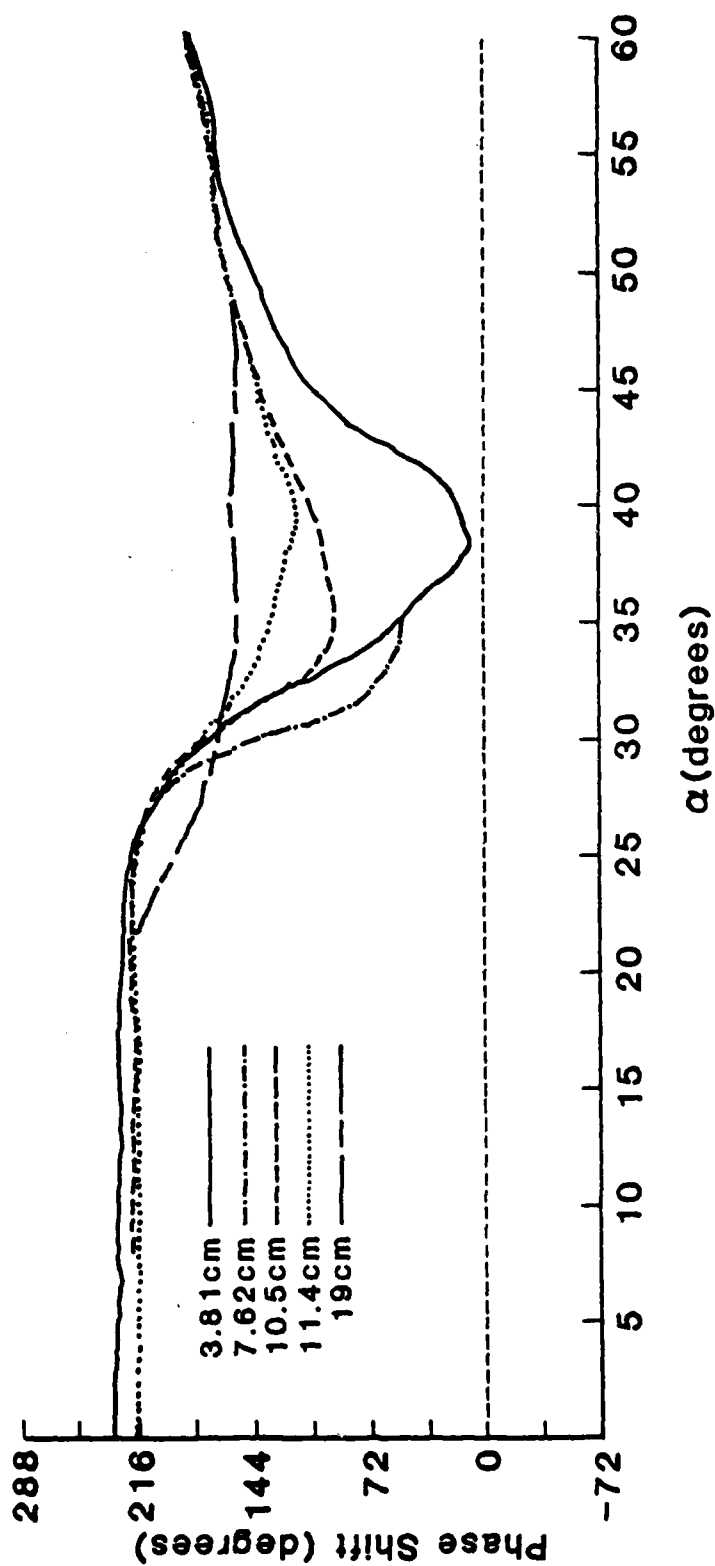


Fig. 4-40 α -Profiles of Phase for $k_{z0} = -.21 \text{ cm}^{-1}$
and $P_{rf} = 6.25$ Watts with z as a Parameter

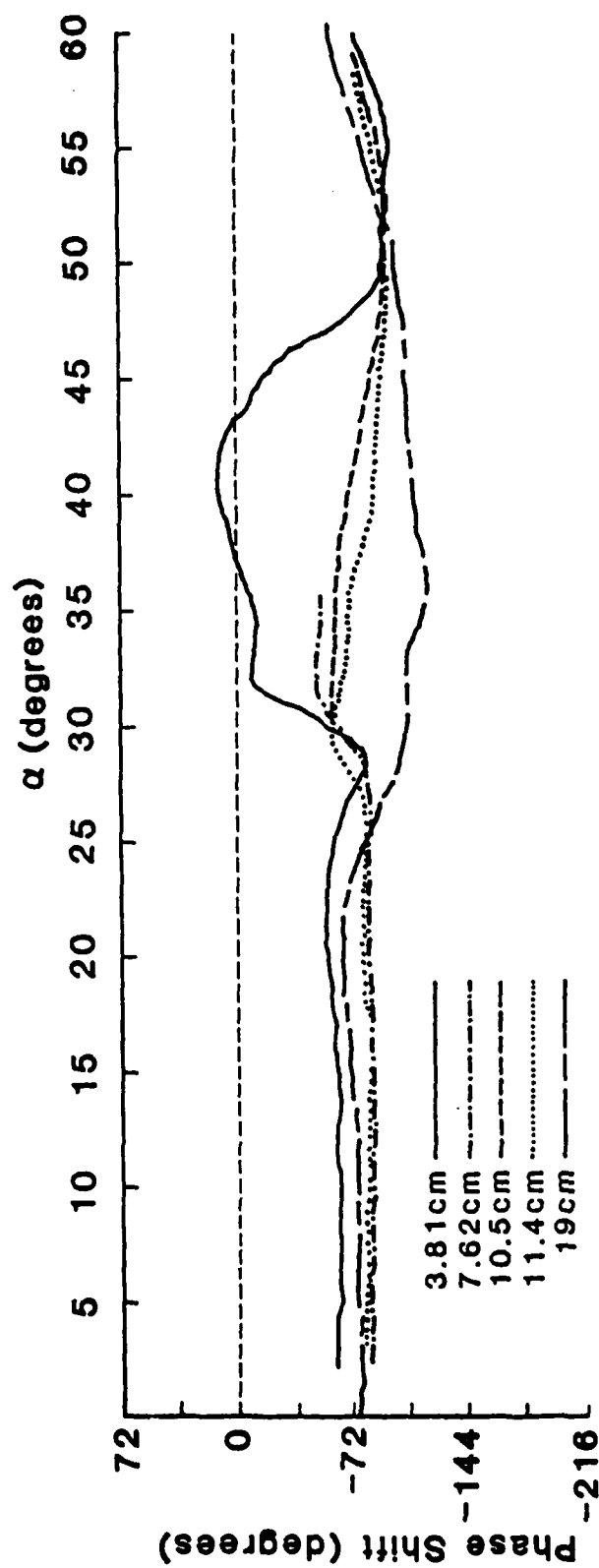


Fig. 4-41 α -Profiles of Phase for $k_{z0} = .21 \text{ cm}^{-1}$
and $P_{rf} = 25$ Watts with z as a Parameter

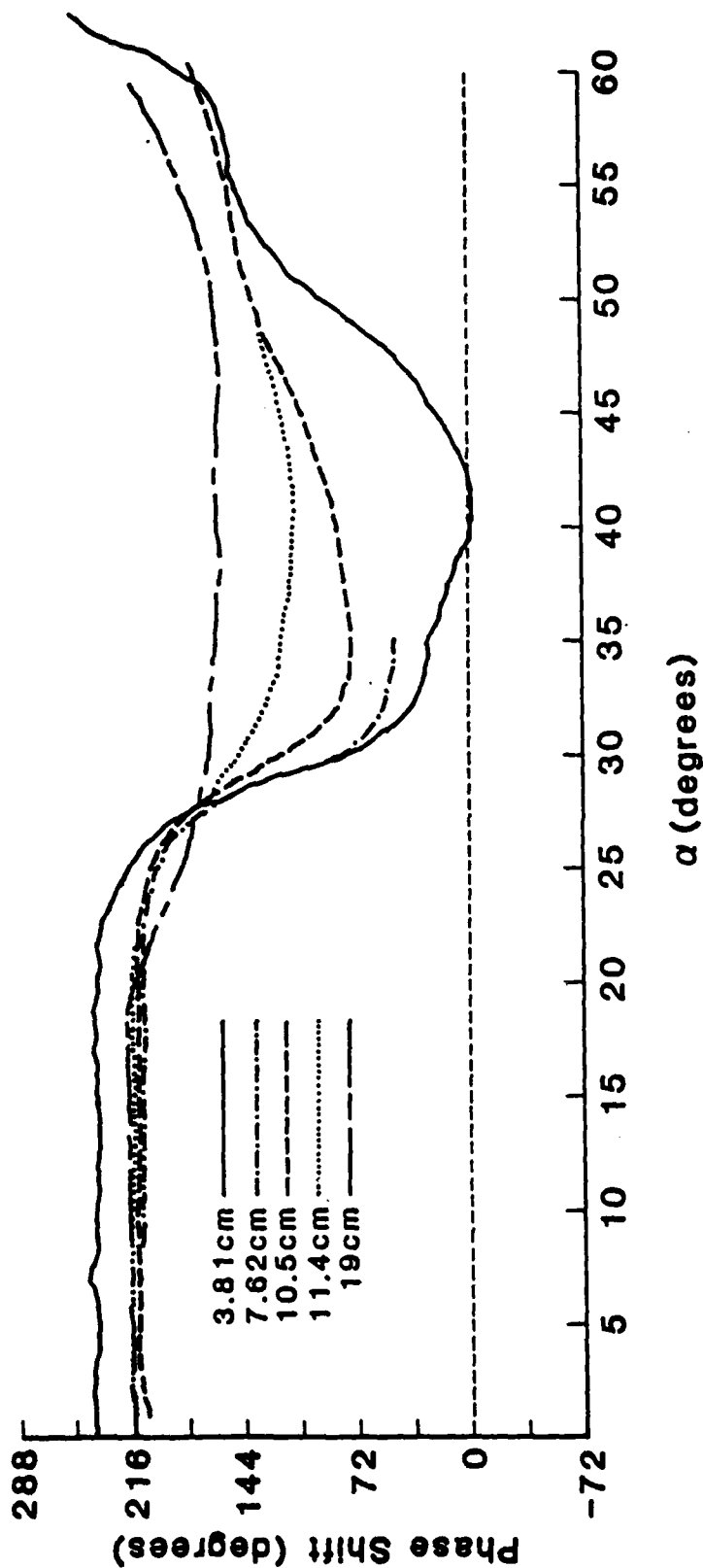


Fig. 4-42 α -Profiles of Phase for $k_{z0} = -.21 \text{ cm}^{-1}$
and $P_{rf} = 25$ Watts with z as a Parameter

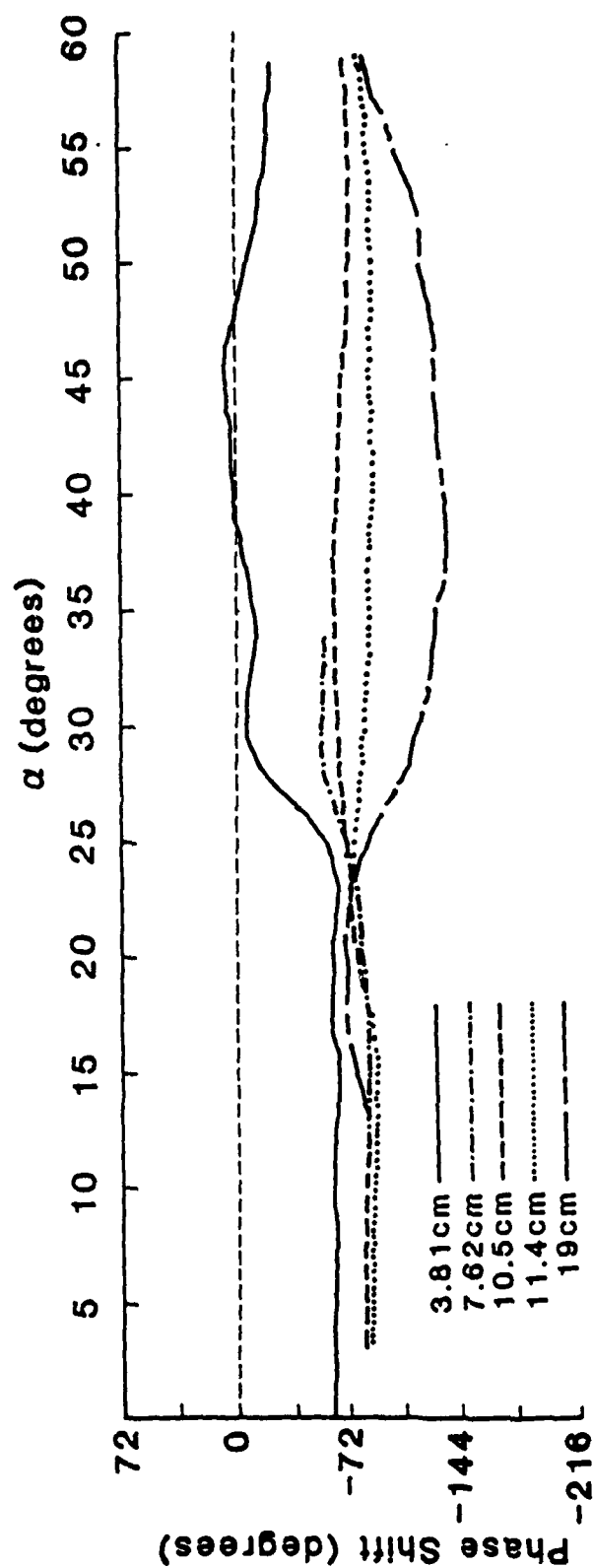


Fig. 4-43 α -Profiles of Phase for $kz_0 = .21 \text{ cm}^{-1}$
and $P_{rf} = 196 \text{ Watts}$ with z as a Parameter

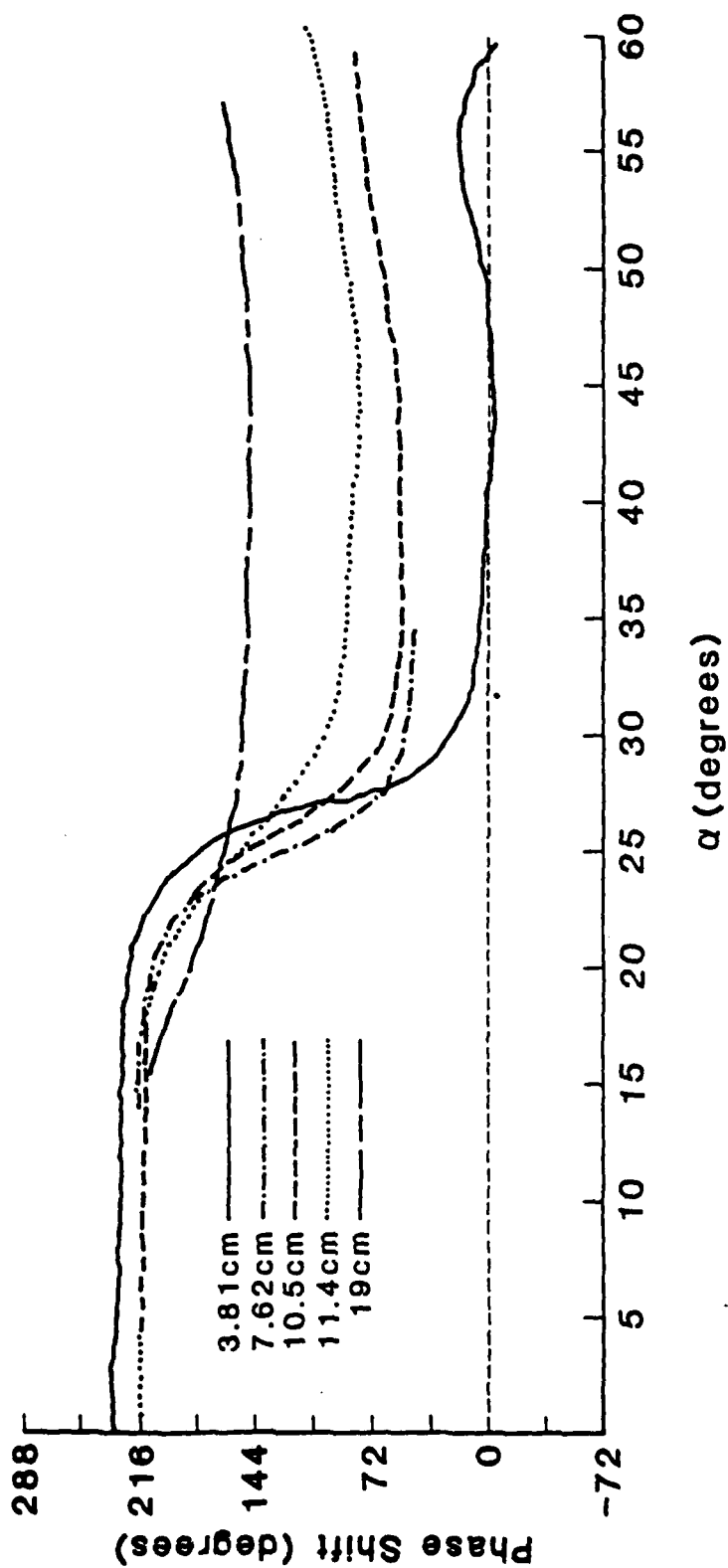


Fig. 4-44 α -Profiles of Phase for $k_{z0} = -.21 \text{ cm}^{-1}$
and $P_{rf} = 196$ Watts with z as a Parameter

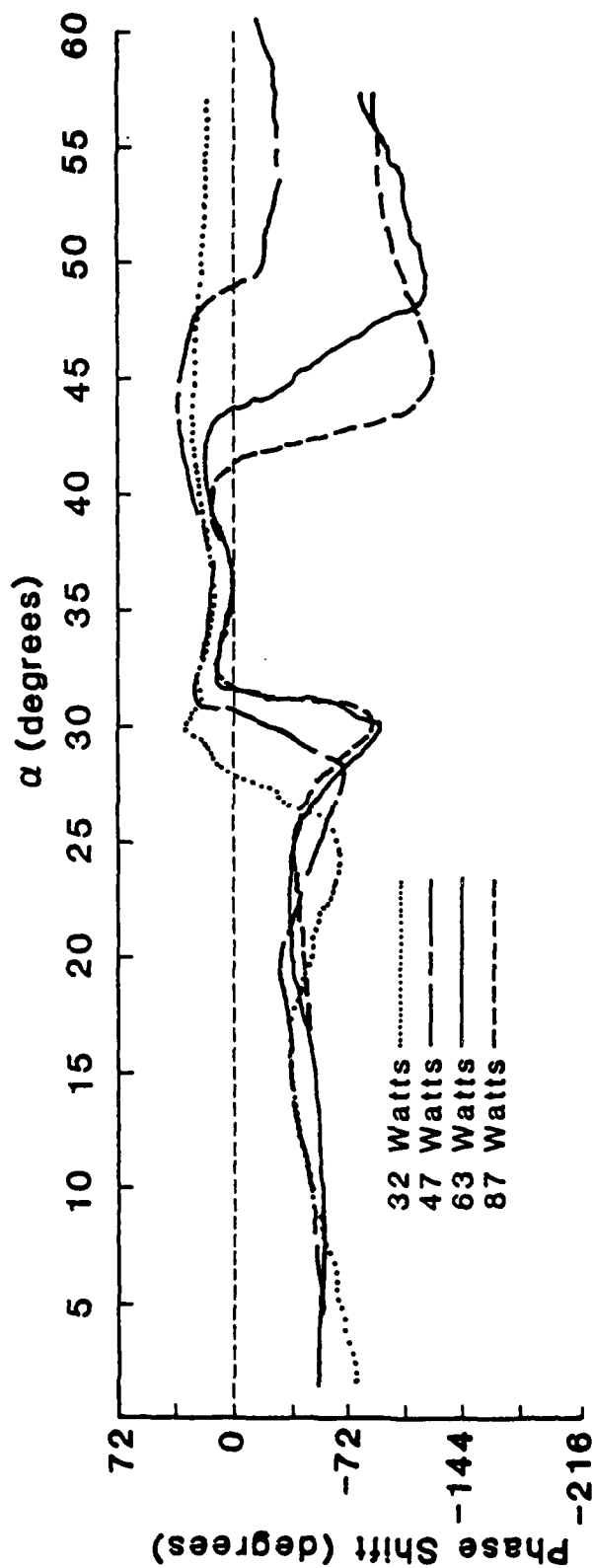


Fig. 4-45 α -Profiles of Phase for $k_{z0} = .21 \text{ cm}^{-1}$ and $P_{rf} = 6.25$ Watts with ECRH Power as a Parameter

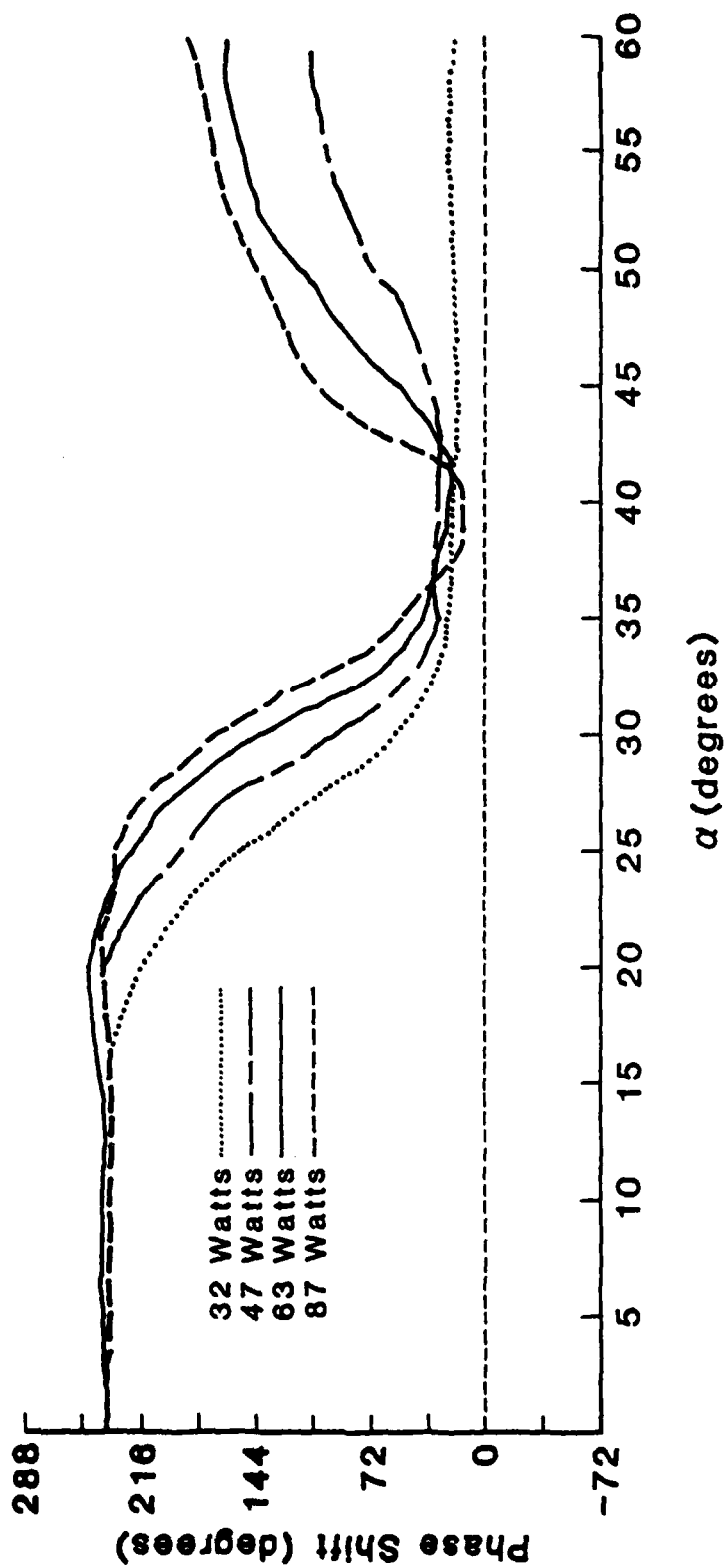


Fig. 4-46 α -Profiles of Phase for $\omega = \omega_{UH}$ and $P_{rf} = 6.25$ Watts with ECRH Power as a Parameter

Chapter 5

THEORETICAL FORMULATION AND INTERPRETATION
OF EXPERIMENTAL RESULTS

5.1 Introduction

In this chapter we consider the basic theoretical formulation of the wave-plasma interaction and discuss the applicability to our experimental results. The theoretical section of this chapter can be basically divided into two parts; the first deals with the excitation of electrostatic waves in an inhomogeneous, magnetized plasma by a slow wave structure, and the second part deals with the interaction of the electrostatic waves with the plasma. While no attempt has been made to give a complete rigorous theory of these problems a summary of the basic theory and relevant results from the literature will be discussed.

5.2 Electrostatic Waves in a Magnetized Plasma

The excitation of electrostatic waves in plasmas by using a slow wave structure has been studied extensively in the literature^{8,10,12,13}. An axial electric field, E_z is imposed near the plasma-vacuum interface using the exciting structure. The phasing of the structure is such that $\omega/k_{z0} \ll c$ and hence an electrostatic approximation, $\vec{E} = -\nabla\phi$ is assumed. The excitation of waves in the frequency range $\Omega_i \ll \omega \ll \omega_{pe} \ll \Omega_e$ is discussed and a time dependence $e^{-i\omega t}$ is assumed.

Following the notation used by Stix³¹, Maxwell's equations can be cast into the following form,

$$\nabla \times \vec{E} = i\omega \mu_0 \vec{H} \quad (5.1)$$

$$\nabla \times \vec{H} = -i\omega \epsilon_0 \vec{K} \cdot \vec{E} \quad (5.2)$$

where \vec{K} is the cold-magnetized plasma dielectric tensor defined by Eq. (5.3)

$$\underline{K} = \begin{bmatrix} K_{xx} & iK_{xy} & 0 \\ -iK_{yx} & K_{yy} & 0 \\ 0 & 0 & K_{zz} \end{bmatrix} \quad (5.3)$$

and

$$K_{xx} = K_{yy} = 1 + \frac{\omega_{pe}^2}{\Omega_e^2 - \omega^2} + \frac{\omega_{pi}^2}{\Omega_i^2 - \omega^2} \quad (5.4)$$

$$K_{xy} = K_{yx} = \frac{\Omega_e}{\omega} \frac{\omega_{pe}^2}{\Omega_e^2 - \omega^2} - \frac{\Omega_i}{\omega} \frac{\omega_{pi}^2}{\Omega_i^2 - \omega^2} \quad (5.5)$$

$$K_{zz} = 1 - \frac{\omega_{pe}^2}{\omega^2} - \frac{\omega_{pi}^2}{\omega^2} \quad (5.6)$$

Assuming only x and z variations and taking the divergence of Eq. (5.2), ϕ can be determined from

$$\frac{\partial}{\partial x} K_{xx} \frac{\partial \phi}{\partial x} + \frac{\partial}{\partial z} K_{zz} \frac{\partial \phi}{\partial z} = 0 \quad (5.7)$$

In the frequency range of interest, i.e., $\Omega_i \ll \omega \ll \omega_{pe} \ll \Omega_e$, K_{xx} and K_{zz} are approximated by

$$K_{xx} \approx 1 - \frac{\omega_{pi}^2}{\omega^2} \quad (5.8)$$

and

$$K_{zz} \approx 1 - \frac{\omega_{pe}^2}{\omega^2} \quad (5.9)$$

It should be noted that K_{xx} and K_{zz} are both functions of x and z since the electron density is inhomogeneous in x and z . Fig. 5-1 shows the geometry of our model. The model in Fig. 5-1 is not strictly valid for our experimental results since the model assumes a constant, uniformly aligned density gradient at an angle γ with respect to the x -axis and experimental results indicate a Gaussian radial density profile. However, since the wave is found not to propagate deep into the plasma we will assume a local constant, uniformly aligned density gradient near the periphery of the plasma column. Fig. 5-1 also defines a new coordinate system, (ρ, η) . The η and ρ axes are perpendicular and parallel to the density gradient ∇n_e respectively and $\rho = \text{constant}$ defines surfaces of constant density. The new coordinates are defined by

$$x = \eta \sin \gamma + \rho \cos \gamma \quad (5.10)$$

$$z = \eta \cos \gamma - \rho \sin \gamma \quad (5.11)$$

and equivalently

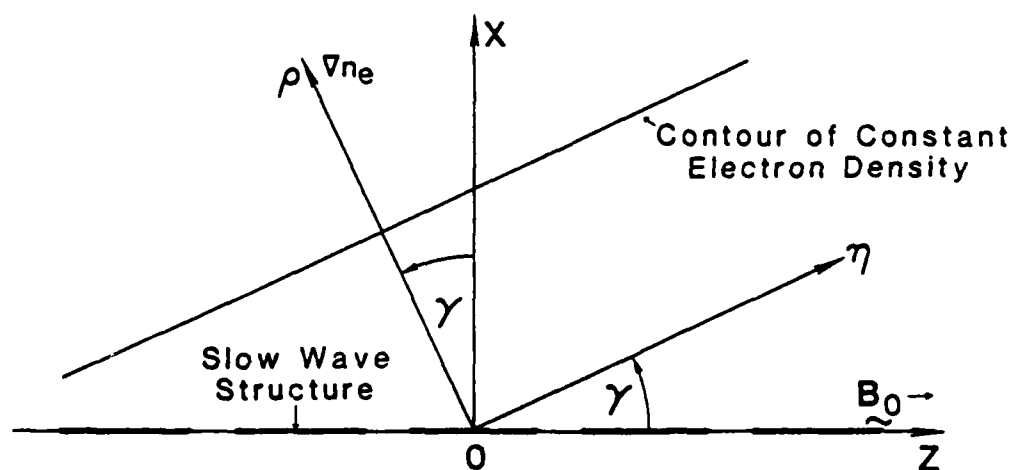


Fig. 5-1 Geometry of the Model

$$\rho = x \cos \gamma - z \sin \gamma \quad (5.12)$$

$$\eta = x \sin \gamma + z \cos \gamma \quad (5.13)$$

Eq. (5.7) must in general be solved in conjunction with the boundary condition defined by the potential field associated with the slow wave structure as in Eq. (5.14)

$$\phi(x=0, z) = \phi_0 e^{ik_z z} \quad (5.14)$$

where ϕ_0 is the peak of the rf potential applied between adjacent coupler plates. Eq. (5.7) can be rewritten in the (ρ, η) coordinate system by using the chain rule and using Eqs. (5.12) and (5.13) to transform the x and z derivatives. The advantage in doing this is that in the (ρ, η) coordinate system the components of the dielectric tensor are only functions of ρ .

$$\frac{\partial \phi}{\partial x} = \frac{\partial \phi}{\partial \rho} \frac{\partial \rho}{\partial x} + \frac{\partial \phi}{\partial \eta} \frac{\partial \eta}{\partial x} = \cos \gamma \frac{\partial \phi}{\partial \rho} + \sin \gamma \frac{\partial \phi}{\partial \eta} \quad (5.15)$$

$$\frac{\partial \phi}{\partial z} = \frac{\partial \phi}{\partial \rho} \frac{\partial \rho}{\partial z} + \frac{\partial \phi}{\partial \eta} \frac{\partial \eta}{\partial z} = -\sin \gamma \frac{\partial \phi}{\partial \rho} + \cos \gamma \frac{\partial \phi}{\partial \eta} \quad (5.16)$$

Inserting Eqs. (5.15) and (5.16) into Eq. (5.7) yields

$$\begin{aligned} & \cos \gamma \frac{\partial}{\partial \rho} \left[K_{xx} \cos \gamma \frac{\partial \phi}{\partial \rho} + K_{xx} \sin \gamma \frac{\partial \phi}{\partial \eta} \right] + \sin \gamma \frac{\partial}{\partial \eta} \left[K_{xx} \cos \gamma \frac{\partial \phi}{\partial \rho} + \right. \\ & \left. K_{xx} \sin \gamma \frac{\partial \phi}{\partial \eta} \right] - \sin \gamma \frac{\partial}{\partial \rho} \left[-K_{zz} \sin \gamma \frac{\partial \phi}{\partial \rho} + K_{zz} \cos \gamma \frac{\partial \phi}{\partial \eta} \right] + \\ & \cos \gamma \frac{\partial}{\partial \eta} \left[-K_{zz} \sin \gamma \frac{\partial \phi}{\partial \rho} + K_{zz} \cos \gamma \frac{\partial \phi}{\partial \eta} \right] = 0 \end{aligned} \quad (5.17)$$

Dividing by $\cos^2 \gamma$ and grouping terms yields

$$\begin{aligned} & \frac{\partial}{\partial \rho} \left[(K_{xx} + K_{zz} \tan^2 \gamma) \frac{\partial \phi}{\partial \rho} \right] + \frac{\partial}{\partial \eta} \left[(K_{zz} + K_{xx} \tan^2 \gamma) \frac{\partial \phi}{\partial \eta} \right] \\ & + \frac{\partial}{\partial \rho} \left[(K_{xx} \tan \gamma - K_{zz} \tan \gamma) \frac{\partial \phi}{\partial \eta} \right] + \frac{\partial}{\partial \eta} \left[(K_{xx} \tan \gamma - K_{zz} \tan \gamma) \frac{\partial \phi}{\partial \rho} \right] = 0 \end{aligned} \quad (5.18)$$

Near $x=0$, $k_\eta = k_{z0}$ and $k_\rho = 0$ for small γ . Since at $x=0$ a wave is launched with the dependence $e^{ik_{z0}z} = e^{ik_\eta \eta}$ and the dielectric tensor is invariant along η we assume plane wave solutions of the form

$$\phi(\rho, \eta) = \xi(\rho) e^{ik_\eta \eta} \quad (5.19)$$

and $\frac{\partial}{\partial \eta} \rightarrow ik_\eta$.

Using the plane wave solution indicated in Eq. (5.19) and noting that K_{xx} and K_{zz} are independent of η Eq. (5.18) can be rewritten as

$$\begin{aligned} & \frac{\partial}{\partial \rho} \left[(K_{xx} + K_{zz} \tan^2 \gamma) \frac{\partial \xi}{\partial \rho} \right] - k_\eta^2 \left[K_{zz} + K_{xx} \tan^2 \gamma \right] \xi + \\ & ik_\eta \left\{ \frac{\partial}{\partial \rho} \left[(K_{xx} - K_{zz}) \tan \gamma \right] \xi + \left[(K_{xx} - K_{zz}) \tan \gamma \right] \frac{\partial \xi}{\partial \rho} \right\} = 0 \end{aligned} \quad (5.20)$$

Following the notation used by Briggs and Parker²² we define

$$K_\rho = K_{xx} + K_{zz} \tan^2 \gamma \quad (5.21A)$$

$$K_{\rho\eta} = (K_{zz} - K_{xx}) \tan \gamma \quad (5.21B)$$

$$K_\eta = K_{zz} + K_{xx} \tan^2 \gamma \quad (5.21C)$$

and Eq. (5.20) is written as

$$\frac{\partial}{\partial \rho} K_{\rho} \frac{\partial \xi}{\partial \rho} - i k_{\eta} \left(\frac{\partial}{\partial \rho} K_{\rho \eta} + K_{\rho \eta} \frac{\partial}{\partial \rho} \right) \xi - k_{\eta}^2 K_{\eta} \xi = 0 \quad (5.22)$$

In weakly inhomogeneous systems, that is, for large k_{ρ} (small wavelength in ρ -direction compared with the scale length in ρ -direction), it is possible to write a local spatially dependent dispersion relation assuming $\xi = \exp \left[i \int^{\rho} k_{\rho}(\rho') d\rho' \right]$. Noting that $\frac{\partial}{\partial \rho} \rightarrow i k_{\rho}$, we have from Eq. (5.22),

$$K_{\rho} k_{\rho}^2 + 2 k_{\eta} K_{\rho \eta} k_{\rho} - k_{\eta}^2 K_{\eta} = 0 \quad (5.23)$$

Since k_{η} is fixed from the boundary condition at $x=0$, k_{ρ} can be determined from Eq. (5.23) as,

$$k_{\rho} = \frac{-k_{\eta} K_{\rho \eta}}{K_{\rho}} \pm \frac{|k_{\eta}|}{K_{\rho}} (K_{\rho \eta}^2 - K_{\rho} K_{\eta})^{1/2} \quad (5.24)$$

Using Eqs. (5.21), Eq. (5.24) can be written as

$$k_{\rho} = \frac{1}{K_{\rho}} \left[-k_{\eta} K_{\rho \eta} \pm |k_{\eta}| (1 + \tan^2 \gamma) (-K_{xx} K_{zz})^{1/2} \right] \quad (5.25)$$

If $\gamma=0$, i.e., $\nabla n_e \perp B_0$, $k_{\rho} = k_x$, $k_{\eta} = k_z$, $K_{\rho} = K_{xx}$, and $K_{\rho \eta} = 0$, yielding

$$k_x = |k_z| \left(\frac{-K_{zz}}{K_{xx}} \right)^{1/2} \quad (5.26)$$

where the plus sign was chosen to be consistent with inwardly plane waves.

Eq. (5.26) is the usual result obtained for a density gradient perpendicular to the background magnetic field. From Eq. (5.25) it is seen that there are propagating waves when K_{xx} and K_{zz} are opposite in sign. This corresponds to the condition that $\omega_{pi} < \omega < \omega_{pe}$. Hence waves can be launched from the low density periphery of the plasma column into regions of increasing density. k_z is determined from

$$k_z = k_\eta \cos \gamma - k_\rho \sin \gamma \quad (5.27)$$

Using k_ρ defined from Eq. (5.25) and the fact that $k_\eta = k_{zo}$, k_z can be written as

$$k_z = k_{zo} \cos \gamma - \frac{1}{K_\rho} \sin \gamma \left[-k_{zo} K_{\rho\eta} + |k_{zo}| (1 + \tan^2 \gamma) (-K_{xx} K_{zz})^{1/2} \right] \quad (5.28)$$

Similarly

$$k_x = k_\eta \sin \gamma + k_\rho \cos \gamma \quad (5.29)$$

and

$$k_x = k_{zo} \sin \gamma + \frac{1}{K_\rho} \cos \gamma \left[-k_{zo} K_{\rho\eta} + |k_{zo}| (1 + \tan^2 \gamma) (-K_{xx} K_{zz})^{1/2} \right] \quad (5.30)$$

Eq. (5.24), or equivalently Eqs. (5.28) and (5.30) indicate two possible mode structures. These modes and their properties have been discussed in detail for lower hybrid waves by Briggs and Parker²² and by Maggs and Morales³² for electrostatic modes in a magnetized plasma with a longitudinal density gradient. We present here a brief summary of the properties of these modes. From Eq. (5.24) we define these modes as

$$k_{\rho+} = \frac{-k_\eta K_{\rho\eta}}{K_\rho} + \frac{|k_\eta|}{K_\rho} (K_{\rho\eta}^2 - K_\rho K_\eta)^{1/2} \quad (5.31)$$

$$k_{\rho-} = \frac{-k_\eta K_{\rho\eta}}{K_\rho} - \frac{|k_\eta|}{K_\rho} (K_{\rho\eta}^2 - K_\rho K_\eta)^{1/2} \quad (5.32)$$

The resonance layer is located at the singular point of the differential equation defining ξ in Eq. (5.22). The singular point is determined from $K_\rho \rightarrow 0$ ²².

$$K_\rho = K_{xx} + K_{zz} \tan^2 \gamma = 0 \quad (5.33)$$

The density at the resonance layer can be determined from Eq. (5.33) as

$$\left(1 - \frac{\omega_{pi}^2}{\omega^2}\right) + \left(1 - \frac{\omega_{pe}^2}{\omega^2}\right) \tan^2 \gamma = 0$$

Solving for the critical density yields

$$n_c = \frac{m_i \epsilon_0}{e^2} \omega^2 \left(\frac{1 + \tan^2 \gamma}{1 + \frac{m_i}{m_e} \tan^2 \gamma} \right) \quad (5.34)$$

From the experimental density profile given in Eq. (4.2)

$$n = n_0 e^{-r^2/R^2} \left(1 - \frac{z}{L}\right) \quad (4.2)$$

Evaluating $\frac{\partial n}{\partial z}$ and $\frac{\partial n}{\partial r}$, the angle the density gradient makes with the r -axis is given by

$$\tan \gamma = \frac{R^2}{2(L-z)r} \quad (5.35)$$

From Eq. (5.35) it is apparent that the angle γ is a function of r and z which severely complicates the analysis. If however, we assume that the critical density occurs at the region of maximum current drive ($r \sim 3.8$ cm) and evaluate Eq. (5.35) at $z = -3.81$ cm it is found that γ can be locally approximated by $\gamma \approx 1.58^\circ$. Inserting experimental parameters into Eq. (5.34) yields $n_c \approx 1.7 \times 10^8 \text{ cm}^{-3}$ comparing favorably with typical values of electron density at these coordinates ranging from approximately $3.5 \times 10^8 \text{ cm}^{-3}$ to $6 \times 10^8 \text{ cm}^{-3}$ as determined from Langmuir probe measurements (see Fig. 4-17). These results are surprisingly accurate considering the approximations made and the tolerances in experimental measurements.

We now consider a brief physical description of the wave fields in the plasma for the two modes described in Eqs. (5.31) and (5.32). First we note that for densities large enough such that $(-K_{xx}K_{zz}) < 0$, i.e., $\omega < \omega_{pi}$ the wave fields are decaying (see Eq. (5.25)) for both modes. Noting that $K_\rho < 0$, i.e., $\omega_{pi} < \omega < \omega_{pe}$, for $k_\eta > 0$ and $k_\eta < 0$ and $k_\rho > 0$ both modes can propagate. If $k_\eta > 0$ the wave propagates in mode $k_{\rho+}$ and experiences a resonance as $K_\rho \rightarrow 0$. If $k_\eta < 0$ the wave propagates in mode $k_{\rho-}$ through the resonance layer and reflects from the lower hybrid layer. It now propagates in mode $k_{\rho+}$ and experiences a resonance as $K_\rho \rightarrow 0$. If the wave is launched into a region of higher density along z , the wave number in the z -direction, k_z as given by Eq. (5.28) can change sign as the wave reflects from the lower hybrid layer and approaches the resonance layer from the high density side. In Eq. (5.28), near the resonance layer, $K_\rho \rightarrow 0$ and is negative; for $k_\eta < 0$ or equivalently $k_{z0} < 0$, the resonance layer is approached via mode $k_{\rho+}$, and choosing the upper sign in Eq. (5.28) we see that the second term has a large positive value and hence the wave propagates in the $+z$ -direction even though the source has an $e^{-ik_{z0}z}$ excitation.

Experimentally it is found that large phase changes occur as one crosses the resonance layer. As the rf probe is moved toward more positive z , i.e., lower electron density, it is found that the phase change is not as large, and in fact for some radial position, k_z does change sign as indicated in Figs. 4-40, 4-42, and 4-44. Also, as the electron density is reduced by reducing ECRH power the region of large k_r moves radially inward to a new location where the electron density is the same as previously. More about the interpretation of physical results will be discussed in section 5.3.

5.3 Interaction of Electrostatic Waves with Plasma

Even though a large amount of experimental data was compiled on the electron dynamics in the presence of the externally excited slow electrostatic wave, it is difficult to interpret the experimental results because of the many competing effects in the plasma. Hence we will briefly describe several possible physical interpretations of the

experimental results. We also summarize the pertinent results from the literature.

First we consider the modification of the electron distribution function due to an electrostatic wave in the plasma. Starting with the collisionless Vlasov equation with an electrostatic perturbation $\phi(\underline{r}, t) = e^{i(\underline{k} \cdot \underline{r} - \omega t)}$

$$\left(\frac{\partial f}{\partial t} + \underline{v} \cdot \nabla f - \frac{e}{m_e} \underline{E} \cdot \nabla_v f \right) = 0 \quad (5.36)$$

where $\underline{E} = -\nabla \phi$, it is possible using quasilinear theory to recast Eq. (5.36) into the quasilinear diffusion equation by using a second order perturbation technique³³.

$$\frac{\partial f}{\partial t} = \nabla_v \cdot \underline{D} \cdot \nabla_v f \quad (5.37)$$

The velocity space diffusion tensor, \underline{D}_v is defined by

$$\underline{D}_v = \frac{2\omega_{pe}^2}{n_0} \int \frac{W_k}{1(\underline{k} \cdot \underline{v} - \omega)} \left(\frac{\underline{k}\underline{k}}{k^2} \right) d\underline{k} \quad (5.38)$$

where $\omega = \omega_r + i\omega_i$

and W_k is the spectral energy density of the electrostatic field. The average electric energy density of the electrostatic field is given by

$$\langle U_E \rangle = \frac{1}{2} \epsilon \langle |E|^2 \rangle = \int W_k d\underline{k} \quad (5.39)$$

and

$$W_k = \frac{\epsilon}{2(2\pi)^3 V} |E_k|^2 \quad (5.40)$$

The Fourier transform of the electric field is defined in the usual sense as

$$\underline{E}_k(t) = \frac{1}{(2\pi)^3} \int \underline{E}(\underline{r}, t) e^{-i\mathbf{k} \cdot \underline{r}} d\underline{r} \quad (5.41)$$

The spectral energy evolves in time according to

$$\frac{\partial}{\partial t} W_k(t) = 2\omega_i(k, t) W_k(t) \quad (5.42)$$

We are primarily concerned with the distribution function in axial velocity and hence we only consider the one-dimensional form of Eq. (5.37)

$$\frac{\partial f}{\partial t} = \frac{2\omega_p^2}{n_0} \frac{\partial}{\partial v_z} \int \frac{W_{k_z}}{i(k_z v_z - \omega)} dk_z \frac{\partial f}{\partial v_z} \quad (5.43)$$

The axial electron kinetic energy density is given as

$$U_{KE} = \frac{1}{2} n_0 m_e v_z^2 \quad (5.44)$$

Multiplying the one-dimensional diffusion equation by the axial electron kinetic energy density and integrating over axial velocities yields a conservation of energy relation.

$$\frac{\partial}{\partial t} \left(\frac{1}{2} n_0 m_e \int v_z^2 f(v_z, t) dv_z \right) = \frac{-\partial}{\partial t} \int W_{k_z}(t) dk_z \quad (5.45)$$

Eq. (5.45) indicates that as the electrostatic wave energy decreases by some damping mechanism the electron kinetic energy must increase by a corresponding amount.

The exciting slow wave structure used in our experiment excites a relatively broad spectrum in k_z of electrostatic waves since the exciting structure is only one wavelength long, i.e., $L_s = 2\pi/k_{z0}$, where

L_s is the axial extent of the slow wave structure. The spectral energy density associated with the exciting structure can be calculated using Eqs. (5.40) and (5.41)

$$E_{k_z} = \frac{1}{(2\pi)^3} \int_0^{L_s} E_o e^{i(k_{zo} - k_z)z} dz \quad (5.46)$$

$$E_{k_z} = \frac{E_o}{(2\pi)^3} \frac{1}{i(k_{zo} - k_z)} \left(e^{i(k_{zo} - k_z)L_s} - 1 \right) \quad (5.47)$$

Evaluating W_{k_z} yields

$$W_{k_z} = \frac{4E_o^2}{(k_{zo} - k_z)^2} \sin^2 \frac{1}{2} (k_{zo} - k_z)L_s \quad (5.48)$$

It is easily seen that the main peak of the spectral energy is contained in the wave number range $0 \leq k_z \leq 2k_{zo}$ which corresponds to electron energies greater than approximately 0.67 eV for $k_{zo} \approx .21 \text{ cm}^{-1}$. Hence the bulk of the electron energy distribution should be modified by the presence of the electrostatic wave. This results in an increase in the average axial electron kinetic energy which manifests itself as an apparent increase in the electron temperature (see Figs. 4-32 and 4.35). This energy is an energy associated with the oscillations of the electrons, i.e., it is not thermalized. It has been shown^{33,34} that the effective electron temperature associated with the plasma electrons is given by

$$T_{\text{eff}} = \left(\frac{4}{k_{Bo} n_o} \right) \int W_{k_z} dk_z + T_{eo} \quad (5.49)$$

where T_{eff} and T_{eo} are measured in eV. Experimentally it is found that the effective temperature increases strongly only near the outer regions of the plasma, i.e., near the region of maximum electron flux and radial phase change. These results are consistent with the results of Decyk, et.al.¹³ in their observation of electron surface heating using a phased array of capacitor plates to couple electrostatic energy into the plasma.

We will now discuss a simple physical interpretation of the rf-induced axial electron flux near the plasma surface based on the ponderomotive force on electrons in an inhomogeneous electrostatic potential in a background magnetic field B_0 .

$$\frac{\partial \underline{v}}{\partial t} + \underline{v} \cdot \nabla \underline{v} = \frac{-e}{m_e} (\underline{E} + \underline{v} \times \underline{B}_0) \quad (5.50)$$

and

$$\underline{E} = -\nabla \phi \quad (5.51)$$

The oscillating electric field has components in both the x and z directions. Noting that

$$\underline{v} \cdot \nabla \underline{v} = \frac{1}{2} \nabla (v^2) - \underline{v} \times \nabla \times \underline{v} \quad (5.52)$$

the z-component of Eq. (5.50) can be written as

$$\frac{\partial v_z}{\partial t} + \frac{1}{2} \frac{\partial}{\partial z} (v_x^2 + v_y^2 + v_z^2) - [\underline{v} \times \nabla \times \underline{v}]_z = \frac{-e}{m_e} E_z \quad (5.53)$$

It is assumed that there is no variation in the y-direction, i.e.

$$\frac{\partial}{\partial y} \rightarrow 0.$$

From Eq. (5.53) it is desired to determine the second order time averaged nonlinear force on the electrons along the background magnetic field. To do this we compute the first order velocities associated with the electrostatic wave using the linearized equation of motion and then computing the z-component of the ponderomotive force by time averaging Eq. (5.53). Writing the linearized equations, i.e. neglecting the convective term $\underline{v} \cdot \nabla \underline{v}$ from Eq. (5.50) and assuming a time dependence $e^{-i\omega t}$

$$v_z = \frac{ie}{\omega m_e} \frac{\partial \phi}{\partial z} \quad (5.54)$$

$$v_x = \frac{-ie}{\omega m_e} \left(-\frac{\partial \phi}{\partial x} + v_y B_0 \right) = \frac{ie}{\omega m_e} \frac{\partial \phi}{\partial x} - \frac{i\Omega_e}{\omega} v_y \quad (5.55)$$

$$v_y = \frac{i\Omega_e}{\omega} v_x \quad (5.56)$$

Solving for v_x yields from Eqs. (5.55) and (5.56)

$$v_x = \frac{ie}{\omega m_e} \frac{\partial \phi}{\partial x} \left(1 - \frac{\Omega_e^2}{\omega^2} \right)^{-1} \quad (5.57)$$

$$\underline{v} \times \nabla \times \underline{v} \Big|_z = v_x \frac{\partial v_x}{\partial z} - v_x \frac{\partial v_z}{\partial x} + v_y \frac{\partial v_y}{\partial z} \quad (5.58)$$

$$\frac{\partial v_z}{\partial t} + \frac{1}{2} \frac{\partial}{\partial z} (v_x^2 + v_y^2 + v_z^2) - v_x \frac{\partial v_x}{\partial z} + v_x \frac{\partial v_z}{\partial x} - v_y \frac{\partial v_y}{\partial z} = \frac{e}{m_e} \frac{\partial \phi}{\partial z} \quad (5.59)$$

Time averaging Eq. (5.59) yields

$$\left\langle \frac{\partial v_z}{\partial t} \right\rangle = \left\langle -\frac{1}{2} \frac{\partial}{\partial z} (v_x^2 + v_y^2 + v_z^2) + v_x \frac{\partial v_x}{\partial z} - v_x \frac{\partial v_z}{\partial x} + v_y \frac{\partial v_y}{\partial z} \right\rangle \quad (5.60)$$

Noting that

$$\frac{\partial}{\partial z} v_x^2 = 2v_x \frac{\partial v_x}{\partial z} \quad (5.61)$$

and

$$\frac{\partial}{\partial z} v_y^2 = 2v_y \frac{\partial v_y}{\partial z} \quad (5.62)$$

Eq. (5.60) can be written as

$$\left\langle \frac{\partial v_z}{\partial t} \right\rangle = \left\langle -\frac{1}{2} \frac{\partial}{\partial z} v_z^2 - v_x \frac{\partial v_z}{\partial x} \right\rangle \quad (5.63)$$

Using the results from Eqs. (5.54) to (5.57) we have

$$\left\langle \frac{\partial v_z}{\partial t} \right\rangle = \left\langle -\frac{1}{2} \frac{\partial}{\partial z} |v_z|^2 - |v_x^*| \frac{\partial |v_z|}{\partial x} \right\rangle \quad (5.64)$$

and

$$\left\langle \frac{\partial v_z}{\partial t} \right\rangle = -\frac{1}{2} \frac{e^2}{\omega m_e} \left[\frac{\partial}{\partial z} \left| \frac{\partial \phi}{\partial z} \right|^2 + 2 \left(1 - \frac{\Omega_e^2}{\omega^2} \right)^{-1} \left| \frac{\partial \phi}{\partial x} \right| \left| \frac{\partial \phi}{\partial x \partial z} \right| \right] \quad (5.65)$$

$$\frac{\partial}{\partial z} \left| \frac{\partial \phi}{\partial x} \right|^2 = 2 \left| \frac{\partial \phi}{\partial x} \right| \left| \frac{\partial \phi}{\partial x \partial z} \right| \quad (5.66)$$

$$\left\langle \frac{\partial v_z}{\partial t} \right\rangle = -\frac{1}{2} \frac{e^2}{\omega m_e} \left[\frac{\partial}{\partial z} \left| \frac{\partial \phi}{\partial z} \right|^2 + \left(1 - \frac{\Omega_e^2}{\omega^2} \right)^{-1} \frac{\partial}{\partial z} \left| \frac{\partial \phi}{\partial x} \right|^2 \right] \quad (5.67)$$

The ponderomotive force density on the electrons, F_p , can be written as

$$F_p = m_e n_o \left\langle \frac{\partial v_z}{\partial t} \right\rangle \quad (5.68)$$

Hence,

$$F_p = -\frac{1}{2} \frac{\epsilon_o \omega_{pe}^2}{\omega^2} \frac{\partial}{\partial z} \left[\left| \frac{\partial \phi}{\partial z} \right|^2 + \frac{\omega^2}{\omega^2 - \omega_e^2} \left| \frac{\partial \phi}{\partial x} \right|^2 \right] \quad (5.69)$$

This result has been obtained by Morales and Lee³⁵ in the study of the nonlinear filamentation of lower-hybrid cones. Since the electrons are strongly magnetized the first term in Eq. (5.69) dominates. This yields

$$F_p = -\frac{1}{2} \frac{\epsilon_o \omega_{pe}^2}{\omega^2} \frac{\partial |E_z|^2}{\partial z} \quad (5.70)$$

The wave field possesses strong spatial variations in the axial electric field and the electrons experience a ponderomotive force given by Eq. (5.70) and the electrons are forced out of the region of large rf potential. Experimentally this is seen as an increase in the axial electron flux. The electrons leave the high field region leaving a net positive charge produced by the ions which produces a large electric field. The ions accelerate out of this region to maintain quasi-neutrality. This leads to a localized density depression in the high field region as discussed by Morales and Lee³⁵, Gekelman and Stenzel^{36,37}, Wilson and Wong³⁸, and Decyk, et.al.¹³.

5.4 Conclusions and Proposal for Future Work

In this work, we have presented experimental results on the interaction of electrostatic waves excited by a slow wave structure with the plasma. It is found that large radial phase changes exist near the lower-hybrid resonance layer and the wave launched from the slow wave structure can experience a reflection when the wave is launched along z into the high density region of the plasma. Large increases in the effective

axial electron temperature are found near the plasma surface consistent with quasilinear theory. Increases in the axial electron flux can be attributed to the large ponderomotive force on the electrons which can lead to ion acceleration and a density depression due to the transient space charge field as the electrons leave the high rf field region.

More detailed phase measurements should be made in the future to obtain a greater understanding of the wave structure. This should include azimuthal phase measurements so that a model may be developed in cylindrical geometry. Also the ion dynamics should be studied by using the electrostatic energy analyzer to measure the ion distribution function to verify the self-consistent acceleration of ions due to the ponderomotive force on the electrons. In addition the mechanism associated with plateau formation in the distribution function as well as the saturation of the rf-incuded electron flux for a $k_{z0} < 0$ excitation should be investigated.

REFERENCES

1. K.L. Wong, Phys. Rev. Lett., Vol. 43, 438 (1979).
2. R. McWilliams and R.W. Motley, Proc. of 4th Topical Conf. on Radio Frequency Plasma Heating, B8-1 (1981) Austin, Texas.
3. R. McWilliams, E.J. Valeo, R.W. Motley, W.M. Hooke, and L. Olson, Phys. Rev. Lett., Vol. 44, 245 (1980).
4. S. Bernabei, C. Daughney, P. Efthimion, W. Hooke, J. Hosea, F. Jobes, A. Martin, E. Mazzucato, E. Meservev, R. Motley, J. Stevens, S. Von Goeler, and R. Wilson, Phys. Rev. Lett., Vol. 49, 1255 (1982).
5. D.K. Bhadra, C. Chu, R.W. Harvey, and R. Prater, Plasma Physics, Vol. 25, 361 (1983).
6. N.J. Fisch and C.F.F. Karney, Phys. Fluids, Vol. 24, 27 (1981).
7. W.M. Hooke and S. Bernabei, Phys. Rev. Lett., Vol. 28, 407 (1972).
8. V.E. Golant, Sov. Phys. Tech. Phys., Vol. 16, 1980 (1972).
9. P.M. Bellan and M. Porkolab, Phys. Fluids, Vol. 17, 1592 (1974).
10. S. Puri and M. Tutter, Nuclear Fusion, Vol. 14, 93 (1974).
11. M. Brambilla, Nuclear Fusion, Vol. 14, 327 (1974).
12. P. Bellan and M. Porkolab, Phys. Rev. Lett., Vol. 34, 124 (1975).
13. V.K. Decyk, J.M. Dawson, and G.J. Morales, Phys. Fluids, Vol. 23, 507 (1979).
14. G. Lisitano, Proc. of 7th Conf. on Phenomena in Ionized Gases, Vol. 1, 464 (1966) Beograd, Yugoslavia.
15. G. Lisitano, R.A. Ellis, Jr., W.M. Hooke, and T.H. Stix, Rev. Sci. Inst., Vol. 39, 295 (1968).
16. R.J. Chrisner, Master of Science Thesis, Electrophysics, June (1972), Polytechnic Institute of Brooklyn.
17. H.M. Kudyan, Ph.D Dissertation, Electrophysics, June 1978, Polytechnic Institute of New York.

REFERENCES (Continued)

18. I. Langmuir and H. Mott-Smith, Phys. Rev. Vol. 28, 727 (1926).
19. J.E. Allen, R.L.F. Boyd, and P. Reynolds, Proc. Phys. Soc., London, Vol. LXX, B, 297 (1957).
20. F.F. Chen, Plasma Physics (Journal of Nuclear Energy, Part C), Vol. 7, 47 (1965).
21. R.H. Huddleston and S.L. Leonard, Plasma Diagnostic Techniques, Academic Press, Chapter 4 (1965).
22. R.J. Briggs and R.R. Parker, Phys. Rev. Lett., Vol. 29, 852 (1972).
23. R.K. Fisher and R.W. Gould, Phys. Fluids, Vol. 14, 857 (1971).
24. T.K. Mau, IEEE Trans. on Plasma Sci., Vol. PS-2, 152 (1974).
25. S.A. Andersen, V.O. Jensen, P. Michelsen, and P. Nielsen, Phys. Fluids, Vol. 14, 728 (1971).
26. S.A. Andersen, G.B. Christoffersen, V.O. Jensen, P. Michelsen, and P. Nielsen, Phys. Fluids, Vol. 14, 990 (1971).
27. M. Guillemot, J. Olivain, F. Perceval, and J. Scharer, Phys. Fluids, Vol. 14, 952 (1971).
28. J.A. Simpson, Rev. Sci. Inst., Vol. 32, 1283 (1961).
29. H.M. Kudyan, Rev. Sci. Inst., Vol. 49, 8 (1978).
30. E. Ott, J.-M. Wersinger, and P.T. Bonoli, Phys. Fluids, Vol. 22, 192 (1979).
31. T.H. Stix, The Theory of Plasma Waves, McGraw-Hill, Chapter 1, (1962).
32. J.E. Maggs and G.J. Morales, Journal of Plasma Physics, Vol. 29, Part 2, 177 (1983).
33. N.A. Krall and A.W. Trivelpiece, Principles of Plasma Physics, McGraw-Hill, Chapter 10 (1973).
34. R.C. Davidson, Methods in Nonlinear Plasma Theory, Academic Press, Chapter 9 (1972).
35. G.J. Morales and Y.C. Lee, Phys. Rev. Lett., Vol. 35, 930 (1975).
36. W. Gekelman and R.L. Stenzel, Phys. Fluids, Vol. 20, 1316 (1977).
37. W. Gekelman and R.L. Stenzel, Phys. Rev. Lett., Vol. 35, 1708 (1975).
38. J.R. Wilson and K.L. Wong, Phys. Rev. Lett., Vol. 43, 1392 (1979).

